主論文

Nature of Hard X-ray Selected Active Galactic Nuclei

- Based on Optical Identification of the *ASCA* Large Sky Survey -

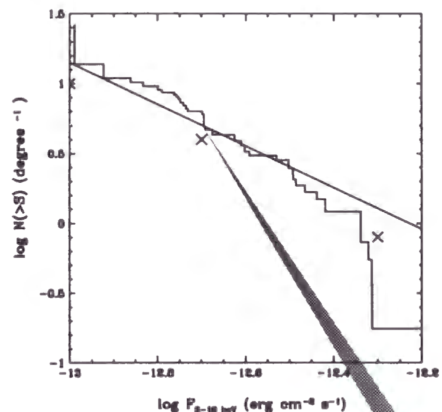

Masayuki Akiyama

A Dissertation Submitted to
Department of Astronomy
Kyoto University
for the Degree of Ph.D

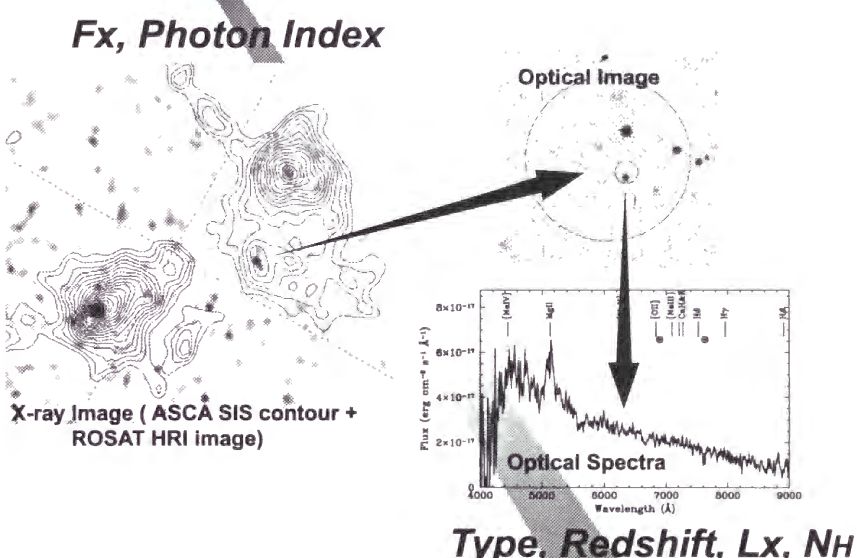

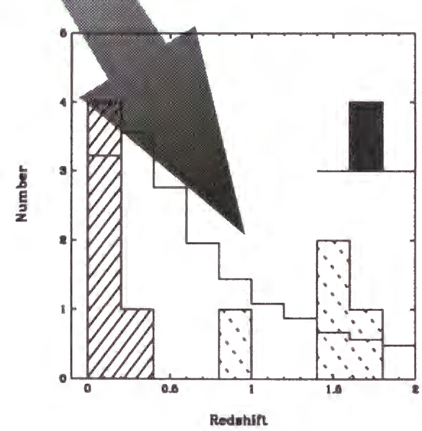

Figure 0: Why optical identification is importnant ?

Abstract

We discuss natures of hard X-ray selected active galactic nuclei (AGNs), based on the sample from optical identification of X-ray sources detected in the *ASCA* Large Sky Survey.

Optical spectroscopic observations were done for 34 X-ray sources which were detected with the SIS in the 2–7 keV band above 3.5 σ. The flux limit corresponds to $\sim 1 \times 10^{-13}$ erg cm^{-2} s^{-1} in the 2–10 keV band. The sources are identified with 30 AGNs, 2 clusters of galaxies, and 1 galactic star. Only 1 source is still unidentified.

All of the X-ray sources that have a hard X-ray spectrum with an apparent photon index of smaller than 1 in the 0.7–10 keV band are identified with narrow-line or weak-broad-line AGNs at redshifts smaller than 0.5. This fact supports the idea that absorbed X-ray spectra of narrow-line and weak-broad-line AGNs make the Cosmic X-ray Background (CXB) spectrum harder in the hard X-ray band than that of a broad-line AGN, which is the main contributor in the soft X-ray band. Assuming their intrinsic spectra are same as a broad-line AGN (a power-law model with a photon index of 1.7), their X-ray spectra are fitted with hydrogen column densities of $\log N_{\rm H}({\rm cm}^{-2}) = 22 \sim 23$ at the object's redshift. On the other hand, X-ray spectra of the other AGNs are consistent with that of a nearby type 1 Seyfert. In the sample, four high-redshift luminous broad-line AGNs show a hard X-ray spectrum with an apparent photon index of 1.3 ± 0.3. The hardness may be explained by the reflection component of a type 1 Seyfert. The hard X-ray spectra may also be explained by absorption with $\log N_{\rm H}({\rm cm}^{-2}) = 22 \sim 23$ at the object's redshift, if we assume an intrinsic photon index of 1.7. The origin of the hardness is not clear yet.

Based on the logN-logS relations of each population, contributions to the CXB in the 2–10 keV band are estimated to be 9% for less-absorbed AGNs ($\log N_{\rm H}({\rm cm}^{-2}) < 22$) including the four high-redshift broad-line AGNs with a hard X-ray spectrum, 4% for absorbed AGNs ($22 < \log N_{\rm H}({\rm cm}^{-2}) < 23$, without the four hard broad-line AGNs), and 1% for clusters of galaxies in the flux range from 3×10^{-11} erg cm^{-2} s^{-1} to 2×10^{-13} erg cm^{-2} s^{-1}. If the four hard broad-line AGNs are included in the absorbed AGNs, the contribution of the absorbed AGNs to the CXB is estimated to be 6%.

In optical spectra, there is no high-redshift luminous cousin of a narrow-line AGN in our sample. The redshift distribution of the absorbed AGNs are limited below $z = 0.5$ excluding the four hard broad-line AGNs, in contrast to the existence of 15 less-absorbed AGNs above $z = 0.5$. The redshift distribution of the absorbed AGNs suggests a deficiency of AGNs with column densities of $\log N_{\rm H}({\rm cm}^{-2}) = 22$ to 23 in the redshift range between 0.5 and 2, or in the X-ray luminosity range larger than 10^{44} erg s^{-1}, or both. Considering the luminosity and redshift distribution of absorbed and less-absorbed AGNs of the *HEAO1* A2 sample, the dependence on the luminosity is suggested. However, if the large column densities of the four hard broad-line AGNs are real, they could complement the deficiency of X-ray absorbed luminous high-redshift AGNs.

We made optical photometric and imaging observations for 6 absorbed and/or narrow-line AGNs in the LSS sample. 5 of them which are at low and intermediate redshift universe reside in early-type (E or S0) galaxies. Luminosities of the 5 objects distribute from 1/2 L^* to $3L^*$ and peak at $2L^*$, if we adopt the absolute magnitude of the knee of the galaxy luminosity function as $M_R = -22.2$ mag. Their radial surface brightnesses are well described by the de Vaucouleurs $r^{1/4}$ law and the surface brightnesses and the effective radii follow the Kormendy relation of E and S0 galaxies in the nearby universe. However, the colors of host galaxies are not fully consistent with those of old elliptical galaxies at their redshift. They show bluer colors than the old elliptical galaxy model. The remaining highest redshift luminous absorbed AGN (absorbed QSO, it should be noted that the object is not "absorbed" AGNs because the best fit column density is 6×10^{21} cm^{-2}) shows two components, a point-like nucleus which is thought to originate from scattered nuclear light and a peculiar extended component whose colors suggest post-starburst nature of the host galaxy.

Contents

Preface

Based on a sample of active galactic nuclei (AGNs) obtained from optical identification of the *ASCA* Large Sky Survey, this dissertation discusses nature of hard X-ray selected AGNs: is there a new population of obscured AGNs, which are escaped from previous surveys in other bands ?, what is the fraction of such population ?, and in what kind of galaxy AGNs reside ?

A certain fraction of AGNs are thought to be obscured and escaped from traditional selection methods for AGNs. If there are many such obscured AGNs in the universe, such population will appear in hard X-ray selection, because hard X-ray emission can pass through absorbing and obscuring matter around AGNs. The fraction of absorbed and obscured AGNs reflect distribution and structure of absorbing matter around the central massive black hole. Therefore, revealing the fraction as functions of redshift and luminosity will enable us to unveil the cosmological evolution of distribution of matter around AGNs. The fraction is also important to understand the origin of the cosmic X-ray background (CXB).

Furthermore, hard X-ray selected absorbed AGNs will give us precious sites to examine the natures of host galaxies of luminous AGNs (i.e. QSOs), especially for the radio-quiet AGN population. Because, the absorption of strong optical emission of AGNs makes it possible to detect faint and small nebulosities around QSOs, especially at intermediate to high redshift universe.

Therefore, sample of hard X-ray selected AGNs are very important. However, though there are large number of soft X-ray selected AGNs found by *ROSAT* in the 0.5–2 keV band, the number of hard X-ray selected AGNs is limited before launch of *ASCA* satellite. *ASCA*, which has the first imaging instrument in the 2–10 keV hard X-ray band, enables us to obtain a large sample of faint X-ray sources in the hard X-ray band for the first time. By hard X-ray surveys with *ASCA*, large number of hard X-ray sources, most of which are thought to be AGNs, have been detected. Information on statistical nature of the hard X-ray sources, such as logN-logS relation (number counts) and X-ray apparent spectral properties, is obtained so far. However,

to reveal the physical properties of the hard X-ray objects, such as luminosities and X-ray spectra in objects' rest frame, optical identification of the objects is indispensable, because we can obtain redshifts only by optical spectroscopic observations at this moment (Figure 0 in the top page).

In this dissertation, the first chapter introduces the previous studies on fraction of absorbed AGNs and host galaxies of AGNs. Next two chapters explain construction of the sample of hard X-ray selected AGNs with optical imaging (Chapter 2) and spectroscopy (Chapter 3). We examined absorption in the AGNs in optical and X-ray wavelength in Chapter 4, based on the spectroscopic properties of the identified AGNs. Spectral energy distributions (SEDs) of the AGNs from radio to X-ray wavelength is examined in Chapter 5. After that, Chapter 6 discusses contributions of the AGNs to the CXB with the logN-logS relation of them. The logN-logS relation of the sample is compared with that of soft X-ray selected AGNs in the chapter. The comparison will give us X-ray spectral information on the AGNs. Chapter 7 and 8 discuss the fraction of absorbed AGNs and host galaxies of the AGNs, respectively. Finally, Chapter 9 summarizes the results and discussions. Throughout this thesis, $H_0 = 50$ km s^{-1} Mpc^{-1} and $q_0 = 0.5$ are used.

Most part of Chapters from 2 to 7 of this dissertation is based on two papers, *"Optical Identification of the ASCA Large Sky Survey"* (*The Astrophysical Journal*, in press) and *"Optical Identification of the Hardest X-ray Source in the ASCA Large Sky Survey"* (*The Astrophysical Journal*, **500**, 173). Chapter 8 is added to show future prospect for studying nature of host galaxies of AGNs selected in the hard X-ray band.

The *ASCA* Large Sky Survey project is originally started by Dr. T. Tsuru, Dr. T. Yamada, and Dr. K. Ohta. The author of the thesis made optical imaging and spectroscopic observations, data reductions, and interpretation of the results. Data obtained by deep follow-up observations with *ROSAT* HRI were also reduced by the author. Some parts of the thesis are kindly supported by collaborators. Reductions of the optical imaging data obtained with the mosaic-CCD camera were done by Dr. W. Kawasaki. The *ASCA* X-ray source catalog is based on the results obtained by Dr. Y. Ueda. The X-ray spectral fittings for each sources were also kindly done by him. Galaxy spectral evolution models used in discussions on the host galaxies are calculated by Mr. N. Tamura.

Chapter 1

Introduction

This chapter summarizes the current status of the studies on the problems: is there a new population of obscured AGNs ?, what fraction of AGNs are absorbed and obscured ? and in what kind of galaxy AGNs reside ? The importance of the hard X-ray selection from the viewpoints of the issues is mentioned. In the final section of the chapter, we introduce the X-ray results of the *ASCA* Large Sky Survey.

1.1 What Fraction of AGNs are Absorbed ?

A certain fraction of AGNs are thought to be absorbed and/or obscured and escaped from traditional optical and UV selection methods for AGNs. Based on the unified scheme of Seyferts, i.e. low-luminous AGNs, (e.g. Antonucci 1993), Figure 1.1 shows a schematic view of a central region of an AGN. The central region consists of a central engine (a massive black hole) broad-emission line clouds, and a dusty torus. Outside of the central region, there are narrow-emission line clouds and interstellar clouds of the host galaxy. The white arrows represent optical emission from the central region, that is, blue featureless continuum and broad emission lines, into various directions. The optical emission is absorbed by dust in the dusty torus and/or interstellar clouds around the central region. In the line of sight which crosses the dusty torus or the interstellar clouds, we only observe narrow-emission lines from photoionized clouds distribute outside of the dusty torus. Such a population of absorbed AGNs is thought to be escaped from traditional AGN selection methods with UV excess and blue optical color.

The fraction of absorbed narrow-line AGNs in the whole AGN populations is one of a big issue in the AGN studies. First, the fraction is esti-

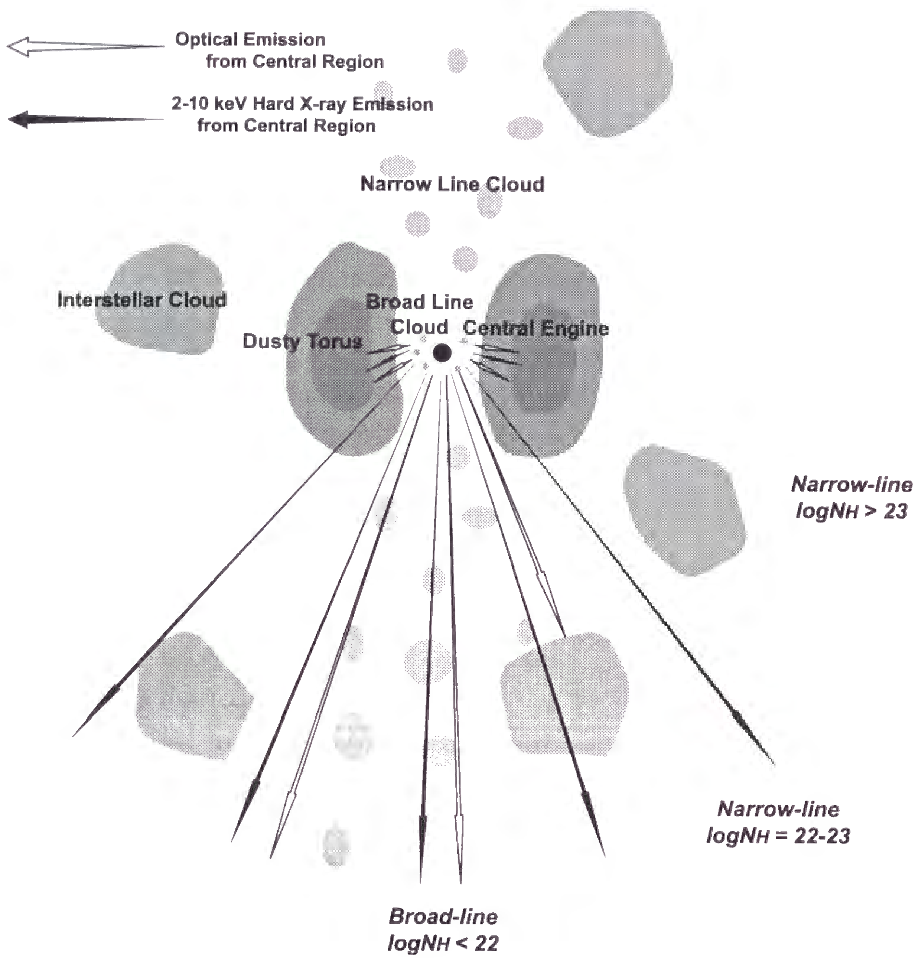

Figure 1.1: Schematic view of the central region of a AGN. White and black arrows represent optical and 2–10 keV hard X-ray emission from central regions.

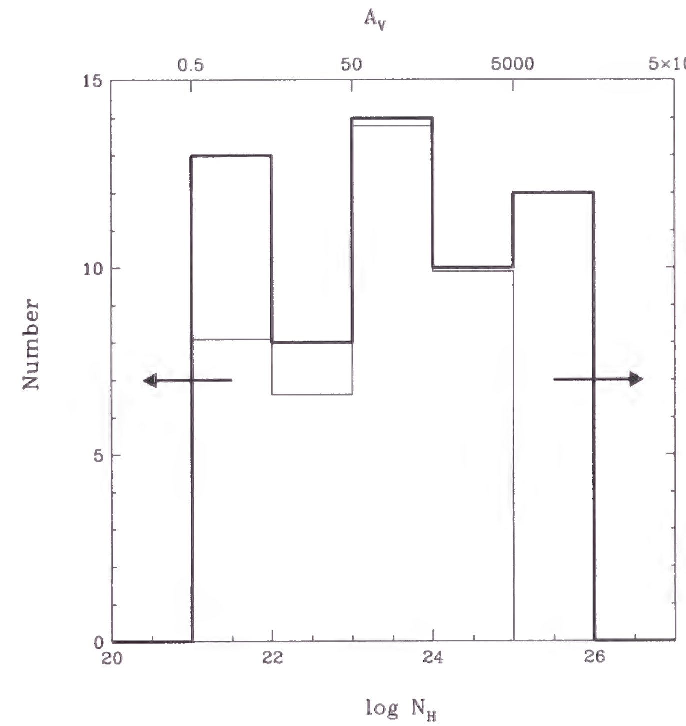

Figure 1.2: The observed column density distribution of Seyfert galaxies (thick histogram, Risaliti et al. 1999) in comparison with the expected column density distribution (thin histogram, Comastri et al. 1995) which reproduce the X-ray spectrum of the cosmic X-ray background. The lowest and highest column density bin includes objects with upper and lower limits to the column density, respectively. In the observed column density distribution, we add 11 type 1 Seyferts which are not included in Risalti et al. (1999) into the lowest column density bin. The number of type 1 Seyferts is estimated based on the number ratio of type 1∼1.5, type 1.8∼1.9, and type 2 Seyferts in Maiolino & Rieke (1995). The upper horizontal axis indicates corresponding optical absorptions to hydrogen column densities, if we assume the Galactic relation (e.g., Predehl & Schmitt 1995)

mated based on the spectroscopic survey of the optical magnitude limited sample of galaxies. Based on the CfA Redshift Survey sample ($m_{\rm Zw} < 14.5$ mag), the number density of type 1.8$\sim$2 Seyferts was estimated to be 2 $\sim$ 3.6 times larger than that of type 1$\sim$1.5 Seyferts (Huchra & Burg 1992, Osterbrock & Martel 1993). Maiolino & Rieke (1995) estimated the over density of absorbed type 1.8$\sim$2 Seyferts as 4, based on the Seyfert galaxies in the Revised Shapley-Ames catalog (RSA, $B_T < 13.3$ mag). These results suggest 60$\sim$80% of Seyferts are heavily obscured. Using the results of *ASCA* observations of the absorbed Seyferts in the RSA sample, Risalti et al. (1999) determined the column density distribution of the absorbed Seyferts. We plotted the results including the number of type 1$\sim$1.5 Seyferts in the lowest column density bin in Figure 1.2 (thick histogram). The distribution has a peak around column density of $\log N_{\rm H}({\rm cm^{-2}}) = 23$ and there are many type 2 Seyferts with a column density larger than Compton-thick value: $\log N_{\rm H}({\rm cm^{-2}}) = 24.2$ (Risaliti et al. 1999).

These studies on the optically selected sample of galaxies are limited to low-luminosity AGNs, i.e. Seyferts, ($L_{\rm 2-10keV} = 10^{40} \sim 10^{44}$ erg s^{-1}), in the nearby universe. For high-luminosity AGNs, i.e. QSOs, the fraction of absorbed AGNs is estimated based on radio or infrared selected AGN samples. Using radio selected 3C sample of radio-loud AGNs, Lawrence (1991) found that the fraction of narrow-line AGNs depends on the radio luminosity of AGNs : below luminosity of $L_{\rm 178MHz} = 10^{28}$ W Hz^{-1}, the fraction of narrow-line AGNs is about 80%, but above luminosity of $L_{\rm 178MHz} = 10^{29}$ W Hz^{-1}, the fraction decreases to 50%. For radio-loud QSOs, the radio luminosity of $L_{\rm 178MHz} = 10^{29}$ W Hz^{-1} roughly corresponds to hard X-ray luminosity of $L_{\rm 2-10keV} = 10^{44}$ erg s^{-1}. Similar dependence of the fraction on the luminosity is found in the far infrared selected AGNs (Veilleux, Kim, & Sanders 1999). Below infrared luminosity of $L_{\rm IR} = 10^{46}$ erg s^{-1}, the fraction of type 2 AGNs is 90% and the fraction decreases to 50% above the luminosity. For normal QSOs, the infrared luminosity corresponds to the hard X-ray luminosity of $L_{\rm 2-10keV} = 10^{44}$ erg s^{-1}. In the low-luminosity range, these results are consistent with the over density of narrow-line Seyferts obtained from the magnitude limited sample. But they suggest the fraction of narrow-line AGNs decreases above the hard X-ray luminosity of $L_{\rm 2-10keV} = 10^{44}$ erg s^{-1}.

On the contrary, a speculation that there is a large population of luminous absorbed AGNs comes from models of the spectrum of the cosmic X-ray background (CXB). The CXB is thought to be summed X-ray emission originated from AGNs at various distances. The spectrum of the CXB ($\Gamma = 1.4 \sim 1.5$ in the 2–10 keV band; Gendreau et al. 1995; Ishisaki et al. 1999) is harder than that of type 1 AGN ($\Gamma = 1.7$ in the 2–10 keV band (Turner & Pounds 1989)), though they are main contributor to the CXB in the soft X-ray band. Thus,

significant contribution from absorbed type 2 AGNs to the hard X-ray band is required to reproduce the CXB spectrum. (Comastri et al. 1995; Madau, Ghisellini, & Fabian 1994). To reproduce the CXB spectrum, it is argued that there are around three times more absorbed AGNs than non-absorbed AGNs in the universe and absorbed AGNs dominate the CXB above 2 keV (the expected column density distribution is shown with thin histogram in Figure 1.2). In consequence of the assumption, the existence of absorbed narrow-line QSO (so called type 2 QSO) is expected.

Recently, candidates of luminous absorbed narrow-line QSOs are identified in optical follow-up observations of X-ray surveys in the soft and hard bands (e.g. Stocke et al. 1982; Almaini et al. 1995; Ohta et al. 1996; Boyle et al. 1998b; Barcons et al. 1998; Schmidt et al. 1998; summarized in Table 1.1). Though follow-up spectroscopic observations revealed existence of a broad permitted emission line in most of the objects (see notes in Table 1.1), weakness of the broad emission lines suggests significant absorptions to the nuclei. Additionally, existence of red *broad-line* QSOs whose red color suggests existence of absorption to its nucleus was reported from a radio survey (Webster et al. 1995). From the radio selected sample of QSOs, Webster et al. argues that 80% of QSO population may be significantly absorbed and escaped from optical/UV selections, if radio-quiet QSOs also have the same absorption as in the radio-loud QSOs. Red *broad-line* QSO population was also identified in *ROSAT* surveys (Puchnarewicz & Mason 1998, Kim & Elvis 1999) and *Beppo-SAX* survey (Fiore et al. 1999). An absorbed broad-line QSO is also found in a deep K band survey (HAWAII 167, Cowie et al. 1994, Egami et al. 1996). They could be radio-quiet counterpart of radio-loud *broad-line* red QSOs. However, X-ray spectra, number densities and contributions to the CXB of both of these red narrow- and broad-line QSO populations are not clear.

One of the other candidates of absorbed luminous AGNs (QSOs) is ultra-luminous infrared galaxies (ULIGs). Their large luminosity in the infrared band is thought to be thermal emission from dust which absorbs UV and soft X-ray emission from central-nuclear and/or intense-starforming activities. and reradiates in the infrared band. Hard X-ray observations with *ASCA* and *Beppo-SAX* reveal heavily absorbed luminous nucleus ($L_{\rm 2-10keV} > 10^{44}$ erg s^{-1}) in some ULIGs (*IRAS* 20460+1925, $L_{\rm 2-10keV} = 1.2 \times 10^{44}$ erg s^{-1} with $\log N_{\rm H}({\rm cm^{-2}}) \sim 22.5$, Ogasaka et al. (1997); *IRAS* 23060+0505, $L_{\rm 2-10keV} = 1.5 \times 10^{44}$ erg s^{-1} with $\log N_{\rm H}({\rm cm^{-2}}) \sim 22.9$, Brandt et al. (1997); NGC6240, $L_{\rm 2-10keV} > 10^{44}$ erg s^{-1} with $\log N_{\rm H}({\rm cm^{-2}}) \sim 24.3$, Vignati et al. (1999); *IRAS* 09104+4109, $L_{\rm 2-10keV} \sim 10^{45}$ erg s^{-1} with $\log N_{\rm H}({\rm cm^{-2}}) > 24.7$, Franceschini et al. (1999)). But, some other ULIGs do not show hard X-ray emission, though their large infrared luminosities suggest the presence

Name	z	Survey	Ref.	Notes
1E0449-184	0.338	*Einstein* Medium Sensitivity	a,b	broad Hβ
RX J13434+0001	2.35	*ROSAT*	c,d	broad Hα
AX J08494+4454	0.8858	*ASCA* Lynx Deep	e,f	
Lockman Hole 12A	0.990	the *ROSAT* deep	g	Radio-loud(RL)
AX J0341.4-4453	0.67	*ROSAT* - *ASCA* South Galactic Pole Deep	h,i	broad Hβ
RX J1011.2+5545	1.246	*ROSAT* Medium Sensitivity	j	broad MgII, RL

Table 1.1: List of X-ray-selected absorbed narrow-line (or weak-broad-line) QSOs with $L_{2-10\ \mathrm{keV}} > 10^{44}$ erg s^{-1}. Reference: a) Stocke et al. (1982), b) Halpern, Eracleous, & Forster (1998), c) Almaini et al. (1995), d) Georgantopoulos et al. (1999), e) Ohta et al. (1996), f) Nakanishi et al. (2000), g) Schmidt et al. (1998), h) Boyle et al. (1998b), i) Halpern, Turner, & George (1999), j) Barcons et al. (1998).

of luminous hard X-ray nucleus (e.g. Arp 220, Iwasawa (1999)). Thus, the fraction of luminous AGNs among ULIGs, the connection between ULIGs and normal QSOs, and contributions to the CXB are not clear yet.

In this dissertation, we discuss the fraction of absorbed AGNs based on hard X-ray selected AGNs. Though the 0.5–2 keV soft X-ray emission, in which many *ROSAT* surveys have been done, is absorbed like optical emission, the 2–10 keV hard X-ray emission can pass through hydrogen column densities of up to 10^{23} cm^{-2} without severe absorption, and a part of a dusty torus and interstellar clouds are transparent for the 2–10 keV hard X-ray emission (black arrows in Figure 1.1 represent the 2–10 keV hard X-ray emission from the central region). Therefore, we can detect AGNs with intrinsic hydrogen column densities of up to 10^{23} cm^{-2} (Section 7.1) which is the peak of the column density distribution of Seyfert galaxies (Figure 1.2) without bias. It should be noted that for hydrogen column densities larger than 10^{23} cm^{-2}, the 2–10 keV hard X-ray emission severely absorbed by photoelectric absorption. Radio emission can also pass through absorbing matter around AGNs and useful to pick up absorbed AGNs (e.g. radio galaxies). But radio-selected AGNs are dominated by radio-loud AGNs whose number density is one-tenth of that of radio-quiet AGNs. Thus, for radio-quiet AGNs which are majority of AGN population, hard X-ray selection is the best way to pick up AGN without bias against absorbed AGNs.

1.2 In What Kind of Galaxy AGNs Reside ?

Understanding the characteristics of host galaxies of AGNs is important to reveal the condition in which AGN phenomena occurs. A correlation between a bulge luminosity and a central black hole mass which is determined from stellar or gas kinematics is reported by Magorrian et al. (1998). The correla-

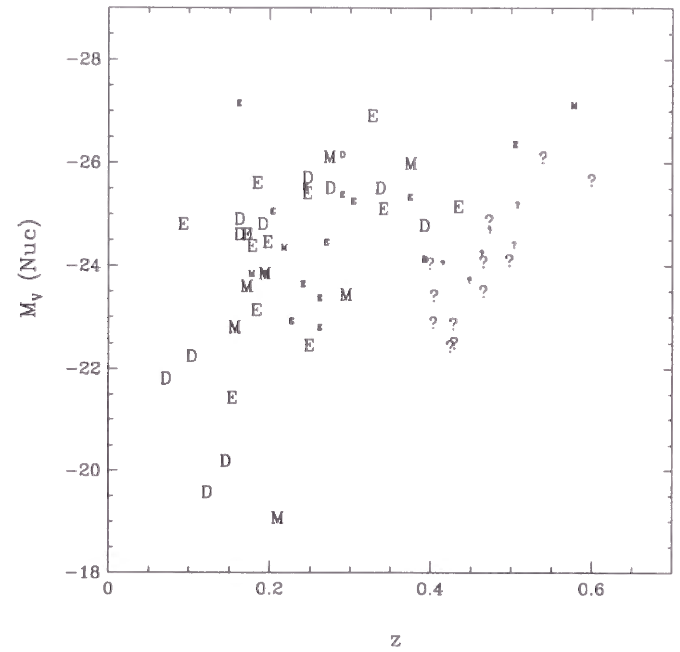

Figure 1.3: Radio-quiet (large marks) and Radio-loud (small marks) QSOs observed with *Hubble Space Telescope*. Labels E and D indicate that a host galaxy of the object is fitted well with the de Vaucouleurs $r^{1/4}$ law and the exponential law, respectively. Apparent merger of two galaxies with similar size is labeled with M. ? means that morphology of the host galaxy of the object is not clear. References: Hutchings et al. (1994), Hutchings & Morris (1995), Boyce et al. (1996), Bahcall et al. (1997), Hooper, Impey, & Foltz (1997), Boyce et al. (1998), Boyce, Disney, & Bleaken (1999), McLure et al. (1999).

tion suggests existence of a central massive black hole in all elliptical galaxies and spiral galaxies with a large bulge. Considering all of elliptical and spiral galaxies do not show AGN phenomena around their central massive black holes, there should be critical conditions to fuel the central massive black hole.

Further evidence of connection between host galaxies and AGN phenomena is the difference of the host galaxy type between radio-loud and radio-quiet low-luminous AGNs: radio galaxies reside in elliptical galaxies, while, Seyfert galaxies tend to live in early-type spiral galaxies.

On the contrary, for luminous AGNs (QSOs), studies on host galaxies are limited because of their bright nucleus. Thus, the connection between characteristics of host galaxies and AGNs is not clear. However, *Hubble Space Telescope* (*HST*) has changed the situation. The sharp point spread function of *HST* makes it possible to detect host galaxies around QSOs. Recently, several studies based on statistical samples of QSO host galaxies have been done. The samples of the observations and morphology of host galaxies are summarized in Figure 1.3. Important results are 1) There is no difference in luminosity between hosts galaxies of radio-quiet and radio-loud QSOs (Hooper, Impey, & Foltz 1997, McLure et al. 1999). 2) Several radio-quiet QSOs have an elliptical galaxy as a host (Bahcall et al. 1997, Boyce et al. 1998, McLure et al. 1999). The elliptical host galaxies of radio-quiet and radio-loud QSOs follow the the surface brightness / scale length relation of nearby E and S0 galaxies (i.e. Kormendy relation) (McLure et al. 1999). 3) Luminosities of the host galaxies are roughly comparable to or 3 times brighter than the luminosity of the knee of the galaxy luminosity function in the nearby universe. The luminosities of host galaxies do not strongly depend on the nuclear luminosities (Bahcall et al. 1997, Hooper, Impey, & Foltz 1997, Boyce et al. 1998, McLure et al. 1999). 4) Many QSOs have a nearby companion galaxy or are merging (see references in Figure 1.3).

However, as seen in Figure 1.3, even with *HST*, it is difficult to determine the detailed morphology of host galaxies above redshift of 0.4 (e.g. Hooper, Impey, & Foltz 1997). But such limitation will be broken by observing host galaxies of absorbed AGNs/QSOs, like high redshift radio galaxies. The absorption of strong optical emission of AGNs makes it possible to detect faint and small nebulosities around QSOs, especially at intermediate to high redshift universe. Therefore, hard X-ray selected absorbed AGNs will give us precious sites to examine the nature of host galaxies of luminous AGNs, especially for the radio-quiet AGN population.

1.3 *ASCA* Large Sky Survey

As shown in above, hard X-ray selected AGNs are very important to study the fraction of absorbed AGNs and host galaxies of AGNs. *ASCA* satellite, which has the first imaging instrument in the 2–10 keV hard X-ray band, makes it possible to obtain a large sample of faint X-ray sources in the hard X-ray band for the first time. To construct a large sample of hard X-ray selected AGNs, we conducted an unbiased large and deep survey with *ASCA* in the region near the north Galactic pole, i.e., *ASCA* Large Sky Survey (hereafter LSS; Inoue et al. 1996; Ueda 1996; Ueda et al. 1998; Ueda et al. 1999a). The flux limit of the LSS ($\sim 1 \times 10^{-13}$ erg cm^{-2} s^{-1} in the 2–10 keV band) is 100 times deeper than the *HEAO1* A2 survey, which was the deepest systematic survey in the hard band (Piccinotti et al. 1982) before *ASCA*. We have surveyed 7.0 deg^2 and 5.4 deg^2 with the GIS and the SIS detectors, respectively. Combining the data from the GIS and the SIS, we detected 44 sources above a 3.5σ level with either the GIS or the SIS in

the 2–10 keV band (Ueda et al. 1999a). They correspond to 20 – 30% of the energy of the CXB in this band. The advantages of the sample are 1) the survey area as a function of limiting count rate was determined well by simulations, 2) accurate X-ray positions were determined by using the SIS whose resolution is higher than the GIS and by correcting the temperature-dependent misalignment between the focal plane detectors and the attitude sensors, and 3) the X-ray spectrum of each source was determined by power-law fitting to the GIS and the SIS data simultaneously in the 0.7–10 keV band (Ueda et al. 1999a). Determining their X-ray spectra is important not only to know their X-ray properties but also to know the flux limit of the survey, because the limit varies with the X-ray spectrum of each source. The average photon index of 36 X-ray sources detected in the flux range between 0.8 $\times 10^{-13}$ and 4 $\times 10^{-13}$ erg cm^{-2} s^{-1} is 1.49 ± 0.1 (Ueda et al. 1999a), which is significantly harder than the spectra of X-ray sources detected in shallower surveys in the 2–10 keV band and close to that of the CXB. Identification of these sources is clearly important to understand the nature of hard X-ray sources and the origin of the CXB. Most of the sources are thought to originate from AGN, thus we can make a sample of hard X-ray selected AGNs.

Chapter 2

Selection of Optical Candidates

This chapter defines a sample of X-ray sources and introduces selection methods how to pick up candidates of optical counterparts of the X-ray sources. There are several optical objects in an error circle of each X-ray source (see Figure 3.3). From them, we selected candidates of optical counterparts, based on deep X-ray observations, a radio source catalog, and UV and optical colors. Hereafter, we call each X-ray source with the exact name and the identification number, like AX J132032+3326(227), for convenience.

2.1 X-ray Sample Definition

To minimize the effect of the galactic absorption and contamination from bright X-ray sources, the survey area was defined as a continuous region of ~ 5 degree^2 near the north Galactic pole, centered at α=13^{h}14^{m}, δ=31°30′ (J2000). Seventy-six pointings of the survey-observations were done from Dec. 1993 to Jul. 1995. These exposures were designed to evenly cover the whole survey region with a 20 ksec effective exposure of the SIS. The source detections were done with the SIS data in the 0.7–7 keV, 0.7–2 keV, and 2–7 keV bands and the GIS data in the 0.7–7 keV, 0.7–2 keV, and 2–10 keV bands. For details of the survey observation, source extraction, and spectral fitting, including the survey region and the position of the sources on the sky, see Ueda et al. 1999a.

In this dissertation, we concentrate on the 34 X-ray sources detected with the SIS in the 2–7 keV band above 3.5σ (hereafter, the SIS 2–7 keV 3.5σ sample). Table 2.1 shows the survey area as a function of limiting count rates for the sample. The typical and the deepest limiting count rates of

Count Rate (cts ksec^{-1})	Area (degree^2)
1.2	0.5
1.4	1.0
1.6	2.0
2.0	3.0
3.0	4.8
4.0	5.0
6.0	5.5
10.0	5.7
20.0	5.8

Table 2.1: Survey Area as a function of the SIS 2–7 keV count rate for the 3.5σ sample from Ueda et al. (1999a).

the sample are 2 counts ksec^{-1} and 1.2 counts ksec^{-1}, respectively. They correspond to 1.8×10^{-13} erg cm^{-2} s^{-1} and 1.1×10^{-13} erg cm^{-2} s^{-1} in the 2–10 keV band for an X-ray source with a power-law spectrum with a photon index of 1.7. All X-ray sources in the SIS 2–7 keV 3.5σ sample have the significance level larger than 4.5 in summed count rate of the GIS and the SIS in both of the 0.7–7 keV and 2–7 keV bands and the positional uncertainties of such sources were estimated to be 0$'$.6 in radius with the 90% confidence level (Ueda et al. 1999a). The number of spurious sources was estimated to be at most a few percent (Ueda et al. 1999a), thus less than 1 spurious source was expected to be in the SIS 2–7 keV 3.5σ sample.

2.2 Selections of Optical Counterpart Candidates

2.2.1 Optical Imaging Data

AGNs are the most plausible optical counterparts for the majority of the X-ray sources, thus at least we have to reach the optical flux limit which is converted from the deepest X-ray flux limit based on X-ray-to-optical flux ratio of AGN. If we assume power-law spectra with an X-ray photon index of 1.7 and an optical energy index of −0.5 together with the X-ray-to-optical flux ratio of AGNs identified in the *ROSAT* Deep Survey (Schmidt et al. 1998), the expected optical magnitude for the optical counterpart of an X-ray source with 1.1×10^{-13} erg cm^{-2} s^{-1} in the 2–10 keV band is $R = 16 \sim 21$ mag.

Candidates of optical counterparts were mainly selected from the APM catalog which is obtained from scans of glass copies of the Palomar Observatory Sky Survey plate (McMahon et al. 1992). However, the limiting magnitude of the catalog is $R \cong 20$ mag and is not deep enough to pick up optical counterparts for faint X-ray sources. To complement the depth of the data, we made imaging observations of the LSS region at the KISO 1.05m Schmidt telescope in March and April 1994. In these observations, we used the mosaic CCD camera (Sekiguchi et al. 1992) which is made up of 15 1024×1024 CCD chips and covers 2×5 degree^2 with 15 shots. The spatial resolution in the setup was 0$''$.75 pix^{-1}. Images were taken in the R band with an exposure time of 20 minutes. The reduction of the data was done by the usual method for optical imaging data. The weather condition during the observation was neither stable nor photometric and the limiting magnitude changed from field to field. The typical seeing was 4$''$ (FWHM) and the typical limiting magnitude was $R \cong 21$ mag, about one magnitude deeper than the APM data.

There are several optical objects within each error circle of X-ray source above $R = 21$ mag. Two X-ray sources (AX J132032+3326(227) and AX J 130748+2925(002)) show clear excesses of galaxies in and around their error circles (see Figure 3.3). These two objects have been cataloged as candidate clusters of galaxies, Abell 1714 (Abell, Corwin, & Olowin 1989) and Zwcl 1305.4+2941 (Zwicky, Herzog, & Wild 1961), respectively. Zwcl 1305.4+2941 was also detected in the *Einstein* Medium Sensitivity Survey and its redshift was determined to be z=0.241 (Stocke et al. 1991). We took deeper and better resolution images with a Tektronix 2048× 2048 CCD on the University of Hawaii 88$''$ telescope on 1995 March and 1996 April in the R and I band and confirmed the excess of galaxies. Thus, we identified the two sources with clusters of galaxies. For other sources, active galaxies are the most plausible counterparts. From optical objects within 0$'$.8, which is slightly larger than the estimated 90% confidence error radius (0$'$.6), of each X-ray source, we selected targets for spectroscopy, using 1) deeper X-ray follow-up data in the soft and hard band, 2) radio emission, and 3) blueness of UV or optical color which indicate existence of an activity in a object.

2.2.2 Deep Follow-up Observations in X-ray band

To pinpoint optical counterparts of X-ray sources, 20 ksec follow-up observations were made with the *ROSAT* HRI in 2 fields in December 1997 in the 0.5–2 keV soft X-ray band. We selected two fields centered at α=13^{h}14^{m}36^s, δ=32°01$'$12$''$ and α=13^{h}12^{m}29^s, δ=31°13$'$12$''$ (J2000) with a radius of 19$'$, to cover as many *ASCA* sources as possible.

The HRI images are shown in Figure 2.1 and 2.2 with contours of the *ASCA* SIS images. The upper and lower figures are HRI 0.5–2 keV images with contours of SIS 0.7–2 keV and 2–7 keV data, respectively. Thus, HRI and SIS data taken in the almost same soft X-ray band in the upper figure. These data were reduced with EXSAS package (Zimmermann et al. 1994) of the MIDAS. For the source detection, we applied the **detect** command selecting photons in the PHA channel range from 2 to 8, only. X-ray sources detected in the HRI follow-up observations with Maximum Likelihood larger than 10 were listed in Table 2.2. The conversion factor from a count rate to a 0.5–2.0 keV flux is 1.854×10^{-14} erg cm^{-2} s^{-1} cts^{-1} ksec. Thus, the flux of the faintest source corresponds to 1.13×10^{-14} erg cm^{-2} s^{-1} .

All of the X-ray sources in the SIS 2–7 keV 3.5σ sample (AX J131521 +3159(136), AX J131407+3158(127), and AX J131327+3155(121) in the former field, and AX J131249+3112(096), AX J131128+3105(080), and AX J 131321+3119(103) in the latter field) except one (AX J131345+3118(104)) in these fields were detected by the HRI and their optical counterparts were pinpointed thanks to the 5″ positional accuracy of the HRI. On the position of the missed source (AX J131345+3118(104)), there is an X-ray peak in the HRI image, though the significance level is slightly lower than the detection limit. Since there is also an optical object at the position, the X-ray source is pinpointed. It should be noted that there is no hard X-ray source which has an X-ray spectrum with an apparent photon index smaller than 1.0 in these HRI observed fields.

Deep 40 $\sim$ 100 ksec pointing observations for 4 sources, which have hard X-ray spectra, (AX J131501+3141(119), AX J131551+3237(171), AX J 131210+3048(072), and AX J130926+2952(016)) were made by *ASCA* and more precise positions and X-ray spectra were obtained (Sakano et al. 1998; Sakano et al. 1999; Ueda et al. 1999b). The error circles for these sources were estimated to be less than 0.′6 at a 90% confidence level.

By the *ROSAT* PSPC, 15 and 13 *ASCA* LSS sources were detected in the *ROSAT* PSPC All-Sky Survey (Voges et al. 1999) and pointing observations (Voges, private communication) as serendipitous sources, respectively. 9 of them were detected in both of the observations, thus the X-ray positions of 19 *ASCA* sources were determined accurately. In details of the cross-identification, see Table 2.3.

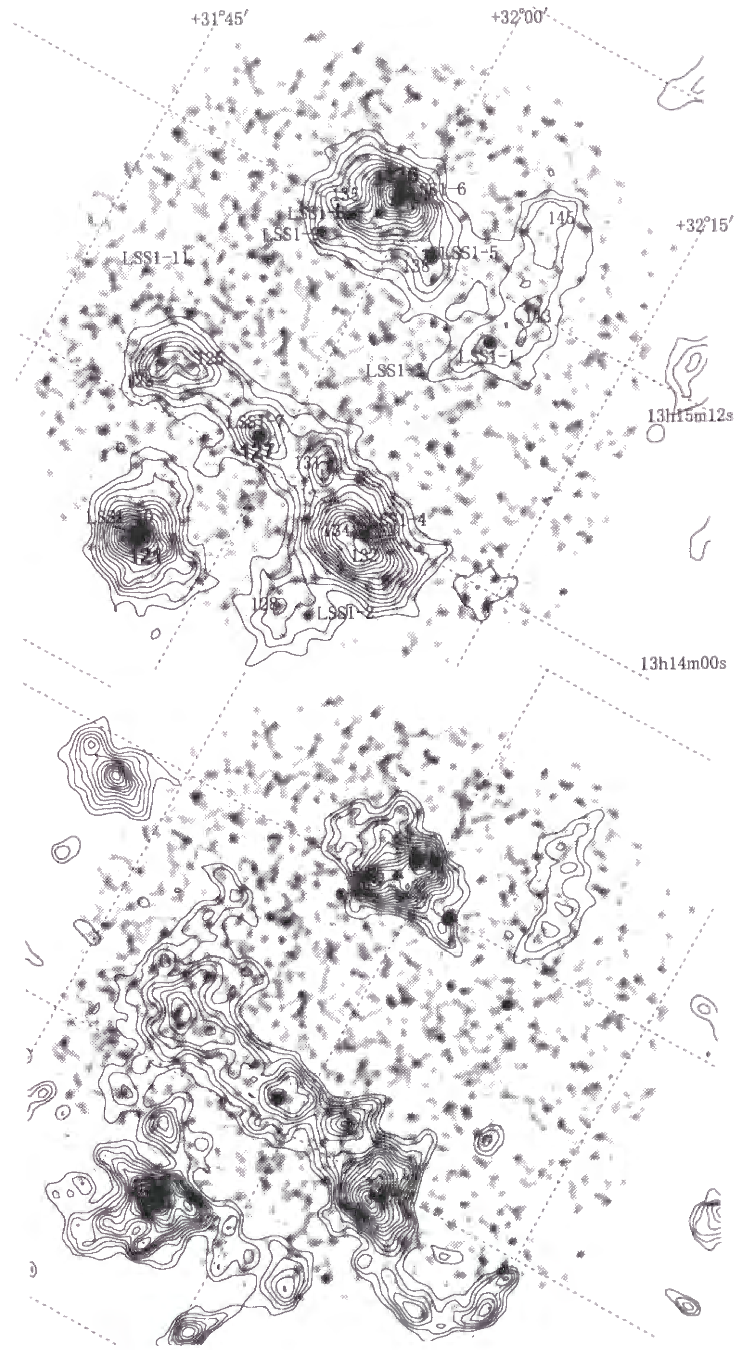

Figure 2.1: *ROSAT* HRI images (grayscale) of LSS field centered on α=13^{h}14^{m}36^{s}, δ=32°01′12″(J2000) in the 0.5–2 keV band. 0.7–2 keV and 2–7 keV SIS contours are superposed on the upper and lower images, respectively. SIS contours, respectively. All detected sources are labeled with id numbers. Sources detected in SIS 2–7 keV band are indicated with bold labels.

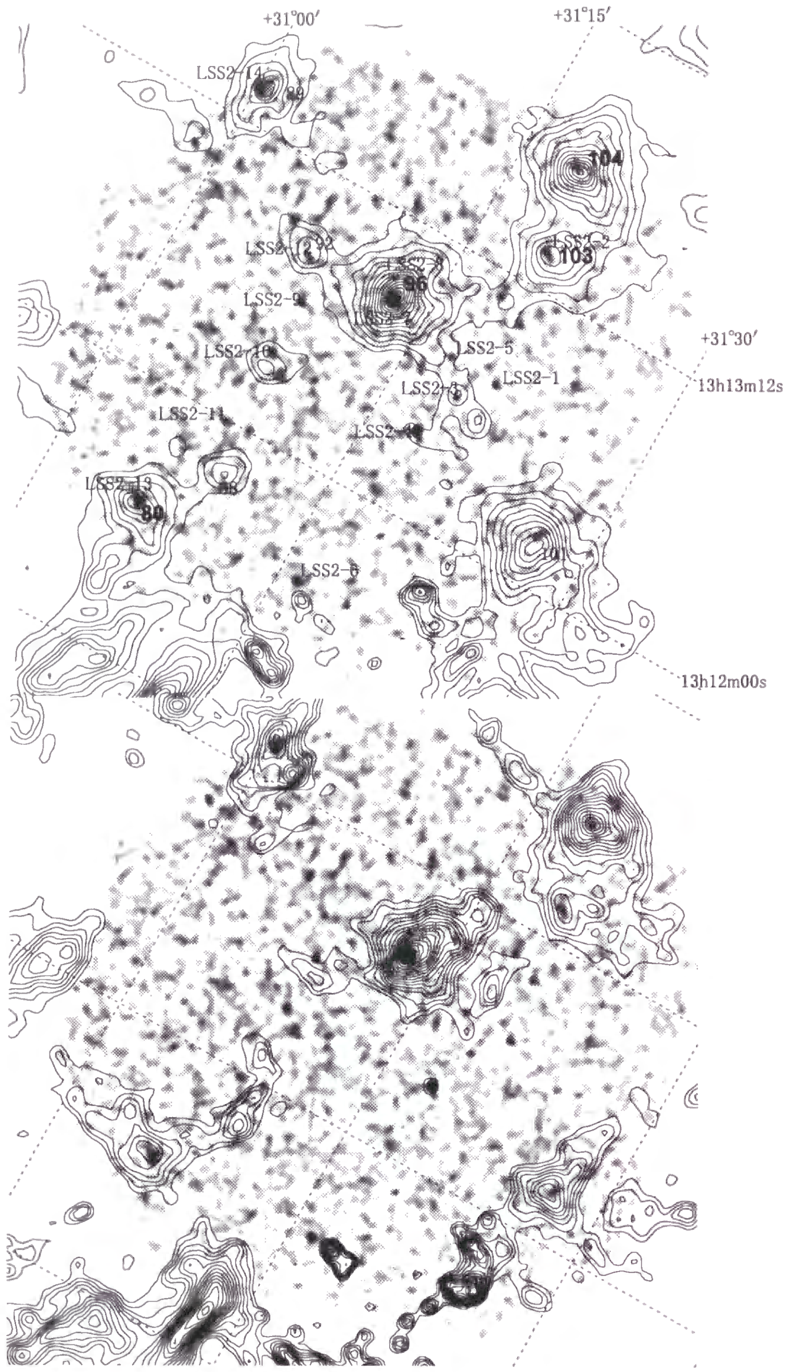

Figure 2.2: *ROSAT* HRI images (grayscale) of LSS field centered on α=13^{h}12^{m}29^s, δ=31°13′12″ (J2000) in the 0.5–2 keV band. 0.7–2 keV and 2–7 keV SIS contours are superposed on the upper and lower images, respectively. All detected sources are labeled with id numbers. Sources detected in SIS 2–7 keV band are indicated with bold labels.

Name	Coordinate (J2000.0)[a] X-ray	ML[b]	Count Rate[b] (cts ksec^{-1})	Coordinate (J2000.0) Optical	R^c	$B-R^c$	Notes
LSS1-01	13 14 58.25 32 07 49.8	76.2	2.64 ± 0.41	13 14 58.11 32 07 48.4	19.48	0.34	
LSS1-02	13 13 29.80 32 06 05.9	10.5	1.59 ± 0.46	13 13 29.39 32 06 07.4	19.83	1.80	
LSS1-03	13 14 41.89 32 05 19.0	15.0	0.61 ± 0.20	13 14 41.80 32 05 17.4	19.67	0.79	
LSS1-04	13 14 09.48 32 03 04.3	10.0	0.61 ± 0.22	13 14 09.82 32 03 00.5	18.55	2.50	
LSS1-05	13 15 11.28 32 02 32.2	219.8	5.20 ± 0.56	13 15 11.12 32 02 29.3	18.99	0.54	
LSS1-06	13 15 21.12 31 59 22.5	401.8	10.13 ± 0.79	13 15 20.93 31 59 21.5[d]	17.72	···	AX J131521+3159(136)
LSS1-07	13 14 06.31 31 58 45.3	169.8	4.37 ± 0.52	13 14 06.40 31 58 44.1	16.66	1.45	AX J131407+3158(127)
LSS1-08	13 15 10.70 31 57 17.7	23.4	1.29 ± 0.31	13 15 10.69 31 57 28.1	16.76	0.94	
LSS1-09	13 15 03.38 31 56 22.8	29.2	1.25 ± 0.29	13 15 03.32 31 56 21.4	18.93	0.96	
LSS1-10	13 13 27.06 31 55 18.8	37.3	4.02 ± 0.66	13 13 27.45 31 55 20.8[d]	17.58	···	AX J131327+3155(121)
LSS1-11	13 14 39.07 31 50 33.5	11.4	1.00 ± 0.31	13 14 39.25 31 50 33.8[d]	···	···	
LSS2-01	13 12 42.47 31 20 32.1	24.3	1.20 ± 0.30	13 12 42.77 31 20 30.5	11.42	···	
LSS2-02	13 13 20.43 31 19 24.5	10.7	1.40 ± 0.41	13 13 20.46 31 19 21.6	19.81	−0.19	AX J131321+3119(103)
LSS2-03	13 12 34.35 31 18 54.2	16.0	0.73 ± 0.23	13 12 34.36 31 18 52.1	20.89	···	
LSS2-04	13 12 21.29 31 17 52.2	121.1	3.20 ± 0.46	13 12 21.26 31 17 50.7	18.13	0.12	
LSS2-05	13 12 43.75 31 17 31.6	16.7	0.78 ± 0.24	13 12 43.59 31 17 28.0[d]	···	···	
LSS2-06	13 11 30.01 31 16 04.3	13.9	1.54 ± 0.42	13 11 30.18 31 16 07.0	18.69	0.00	
LSS2-07	13 12 48.92 31 13 00.6	456.2	9.29 ± 0.77	13 12 48.80 31 13 00.6	17.85	0.77	AX J131249+3112(096)
LSS2-08	13 12 54.80 31 12 26.5	11.9	0.66 ± 0.23	13 12 54.92 31 12 22.7	···	···	2 objects blended
LSS2-09	13 12 36.28 31 08 26.6	31.1	1.17 ± 0.29	13 12 36.41 31 08 26.2	···	···	
LSS2-10	13 12 21.15 31 08 24.1	28.6	1.19 ± 0.30	13 12 21.08 31 08 24.8[d]	···	···	
LSS2-11	13 11 58.49 31 07 53.4	10.2	0.87 ± 0.29	13 11 58.52 31 07 57.6	19.78	1.30	
LSS2-12	13 12 47.79 31 07 43.1	14.8	0.79 ± 0.25	13 12 47.70 31 07 44.1	···	···	
LSS2-13	13 11 28.49 31 05 47.3	16.6	3.17 ± 0.70	13 11 28.41 31 05 51.7	17.15	0.54	AX J131128+3105(080)
LSS2-14	13 13 21.77 31 00 17.0	25.5	4.36 ± 0.80	13 13 21.51 31 00 19.6	19.71	0.19	

Table 2.2: *ROSAT* HRI sources in field 1 and 2

Notes:

a: Considering systematic shifts between candidates of optical counterparts and X-ray sources, we shifted the X-ray positions with $\Delta\alpha = -3\farcs39$, $\Delta\delta = +5\farcs08$ and $\Delta\alpha = -2\farcs37$, $\Delta\delta = +3\farcs18$ for regions LSS-HRI1 and LSS-HRI2, respectively. b: Maximum likelihoods and count rates in the PHS channel range from 2 to 8, only.

c: Coordinates and magnitudes are taken from APM catalog (McMahon et al. 1992), except for objects with notes.

d: Coordinates determined by mosaic CCD image taken at KISO observatory.

Name	No.	*ROSAT* PSPC
AX J131822+3347	235	1RXS J131823.5+334745,1RXP J131824.5+334733
AX J131850+3326	219	1RXS J131851.8+332653,1RXP J131852.1+332616
AX J131345+3118	104	1RXP J131344.8+311841
AX J131831+3341	228	1RXP J131832.1+334146
AX J131758+3257	195	1RXS J131759.6+325741
AX J131805+3349	233	1RXS J131807.5+334929
AX J131831+3320	212	1RXS J131832.4+332019,1RXP J131831.5+332038
AX J131521+3159	136	1RXS J131521.7+315930
AX J131156+3054	075	1RXP J131157.4+305448
AX J131725+3300	192	1RXS J131725.7+330024,1RXP J131725.4+330018
AX J131407+3158	127	1RXS J131405.5+315901
AX J130748+2925	002	1RXS J130749.3+292536,1RXP J130748.7+292542
AX J131327+3155	121	1RXS J131325.4+315515
AX J131529+3117	110	1RXS J131528.9+311737,1RXP J131529.9+311733
AX J131927+3343	238	1RXP J131925.9+334303
AX J130926+2952	016	1RXS J130927.3+295204,1RXP J130927.7+295205
AX J131128+3105	080	1RXS J131128.9+310542,1RXP J131127.8+310539
AX J131015+3004	033	1RXS J131016.3+300408
AX J130826+3005	023	1RXS J130829.6+300536,1RXP J130829.8+300539

Table 2.3: The identifications of the *ASCA* LSS sources with the *ROSAT* PSPC sources

Notes:

a: 1RXS and 1RXP mean sources from *ROSAT* PSPC All-Sky Survey Source Catalog (Voges et al. 1999) and *ROSAT* PSPC Pointing Catalog (Voges, private communication), respectively.

2.2.3 Cross-correlation with FIRST Radio Source Catalog

In the course of the optical counterpart selection, we examined the distribution of FIRST radio sources around LSS X-ray sources to evaluate the cross-correlation between radio and X-ray sources. The FIRST survey is a radio source survey conducted with the Very Large Array in the 1.4 GHz band with a 5σ limiting flux of 1 mJy (Becker, White, & Helfand 1995). Figure 2.3 shows the results of cross-correlation. There are 17 radio sources within $0'.6$ from the centers of the X-ray sources; by contrast no radio source exists between $0'.6$ and $0'.8$ from them. Based on the surface number density of detected radio sources in the LSS field, the contamination of a radio source which is not a counterpart of an X-ray source is expected to 0.73 sources for the whole 34 X-ray sources within $0'.6$. Thus, the 17 radio sources are likely radio-counterparts of X-ray sources. In details of the cross-identification, see Table 2.4. Three X-ray sources have two to four radio sources within $0'.6$. They are thought to be radio-loud objects with radio lobes or clusters of galaxies. One of the three X-ray sources is already identified with a cluster of galaxies (AX J132032+3326(227)). In summary, 35% (12/34) of the SIS 3.5σ sample are detected in the FIRST survey and an optical counterpart is pinpointed thanks to the good positional accuracy ($1''$) of the FIRST catalog, except for AX J131639+3149(137). For the X-ray source, there is no optical object within an error circle of the FIRST radio source (see notes in Section 3.2). In the error circle of AX J131529+3117(110), there is a radio peak with a flux of 0.63 mJy which is slightly lower than the detection limit of the FIRST. Because there is an optical object at the position, we identified the optical object with the counterpart of the radio peak and the X-ray source.

The high fraction of radio-detected X-ray sources in comparison with other results (e.g., 10% in De Ruiter et al. 1997) is due to a match between the flux limit of the *VLA* FIRST 1.4 GHz survey and that of the LSS; the ratio of the flux limits is one order of magnitude larger than the typical radio-to-X-ray flux ratio of *radio-quiet* broad-line AGN (Elvis et al. 1994) but within the scatter of the ratio of the *radio-quiet* population. Thus, not only radio-loud AGNs but also some radio-quiet AGNs are included in the LSS-FIRST sample (see Section 5.2). It is worth noting that radio emission can pass through obscuring material, thus obscured AGNs are detected in the radio wavelength as well as in the hard X-ray band, in an unbiased way.

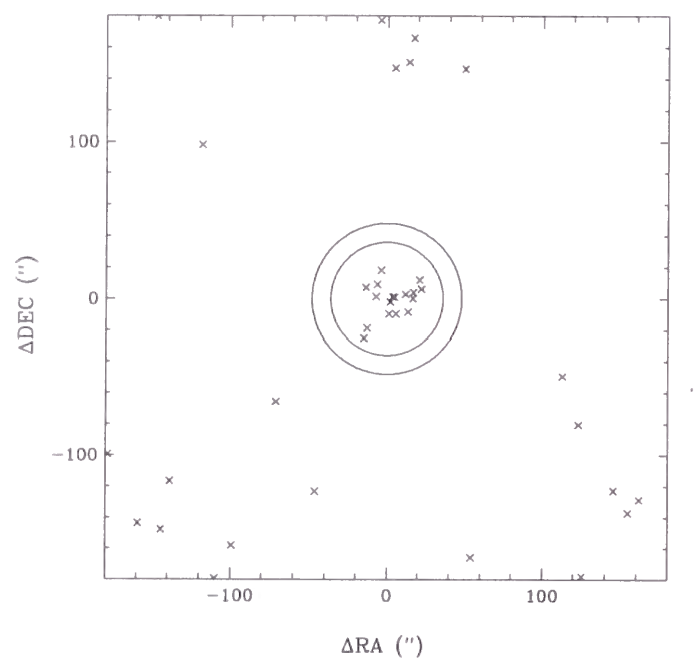

Figure 2.3: Distribution of FIRST radio sources around SIS 2–7 keV 3.5σ sample. The inner and outer circles have radius of 0!6 and 0!8, respectively.

2.2.4 UV and Optical Colors

Based on the results of the optical identification in soft X-ray surveys, a broad-line AGN is a plausible optical counterpart for a part of X-ray sources detected in the hard band and they can be selected by a blueness of their UV or optical color if they are at redshift smaller than 3. There are two UV-excess surveys which cover the southern half ($\delta < 32°10'$) of the LSS. These are Usher (1981) and Moreau & Reboul (1995). Objects with an $U - V$ color bluer than 0.0 down to $B = 20$ mag and 0.1 down to $V = 20$ mag are cataloged in the former and the latter, respectively. 8 out of 20 X-ray sources in the area have one or two UV-excess object(s) within 0!8 in total. 6 are also detected in the X-ray follow-ups with *ROSAT* HRI or in the FIRST survey. Considering the number density of UV-excess objects in Moreau & Reboul (1995), the expected number of contamination within 0!8 from the center of the 20 X-ray sources is calculated to be 0.5, thus all 8 correlated objects can be considered as plausible optical counterparts of X-ray sources. Such a low probability of contamination indicates that there is no serious bias to selecting an UV excess object which is not a true optical counterpart of an X-ray source. Additionally, two galaxies in the 0!8 radii

Name	No.	FIRST
AX J131345+3118	104	FRS J131344.1+311829
AX J131249+3112	096	FRS J131248.7+311300,FRS J131249.4+311249
AX J131831+3341	228	FRS J131831.6+334146
AX J131758+3257	195	FRS J131800.2+325752
AX J131805+3349	233	FRS J131805.2+334938
AX J131054+3004	037	FRS J131055.0+300410
AX J131639+3149	137	FRS J131638.9+314956
AX J132032+3326	227	FRS J132033.4+332633,FRS J132031.1+332614
		FRS J132033.8+332639,FRS J132030.9+332608
AX J131501+3141	119	FRS J131501.1+314129
AX J130748+2925	002	FRS J130749.2+292548
AX J131327+3155	121	FRS J131327.3+315523,FRS J131328.2+315516
AX J131210+3048	072	FRS J131211.9+304821

Table 2.4: The identifications of the *ASCA* LSS sources with the VLA FIRST sources

of AX J131805+3349(233) are cataloged as UV-excess galaxies in the KUG catalog (Takase & Miyauchi-Isobe 1986).

To select candidates of broad-line AGNs with fainter magnitude and to cover the whole LSS area, we also picked up objects with $B-R < 1.0$ mag as a broad-line AGN candidates in the whole area, assuming a typical color of broad-line QSOs ($\alpha = -0.5$, $B - R = 0.52$ mag; Richstone & Schmidt 1980) with a dispersion of distribution ($\Delta B - R = 0.2$ mag) and an error of photometry ($\Delta B - R = 0.3$ mag). The APM $O - E$ color was converted to the $B - R$ color with $(O - E)_{\rm APM} = 1.135 \times (B - R)$ (Evans 1989). 19 X-ray sources have one or two optical object(s) which meet the above criteria within 0!8. 5 of them are also detected in either the X-ray follow-ups with *ROSAT* HRI or in the FIRST survey. Within 0!6 and between 0!6 and 0!8 from the 34 X-ray sources, there are 19 and 6 blue objects, respectively. Based on the number density of objects with $B - R$ color bluer than 1.0 in the APM catalog, the expected number of contamination of blue objects which are not X-ray source is estimated to be 6 and 5 in the inner circles and outer annuli, respectively. Thus, two thirds of the blue objects in the inner circles are expected to be true optical counterpart of X-ray sources, on the other hand, most of the blue objects in the outer annuli are thought to be contamination of non-X-ray objects.

Almost all (5 out of 6) the hard X-ray sources which have a photon index smaller than 1.0 have no such blue object within their error circles; therefore an optical counterpart different from a broad-line AGN is suggested. This tendency is the same as the previous results reported in Akiyama et al. (1998b), but the new result is more significant than the previous one, because we concentrate on brighter X-ray sources whose positions and X-ray photon indices were determined well and more accurate X-ray positions were obtained for each X-ray source by correcting for the temperature effect in the satellite acquisition as mentioned in Section 1.3.

In summary, except for 2 clusters of galaxies, 24 sources were pinpointed by X-ray follow-ups with the *ROSAT* HRI or PSPC or radio detections, 5 more sources have only one object which is selected by its blue optical color, and the remaining 3 sources have no optical counterpart which meets the above criteria. For these 3 sources, we picked up the brightest optical object within each error circle as a primary target. In the next chapter, we show the list of the selected objects in Table 3.1 and, in finding charts of Figure 3.3, they are labeled with "A", "B", and "C" in order of distance from the X-ray centroid. Additionally, we listed some objects which were not selected by the above methods but observed in the optical spectroscopy. These objects were indicated with a label "Z".

Chapter 3

Optical Identification

We made optical spectroscopic observations for the optical-counterpart candidates of the 34 X-ray sources in the SIS 2–7 keV 3.5σ sample. We have successfully identified 33 X-ray sources with 30 AGNs, 2 clusters of galaxies, and 1 galactic star. In this chapter, we summarize the results of the optical identification. We also discuss the reliability of the identification based on probability of chance contamination and optical to X-ray flux ratios of the objects.

3.1 Spectroscopic Observations

At first, for the hardest X-ray source (AX J131501+3141(119)), we made spectroscopic observations with the multislit spectrograph (CryoCam) on the Kitt Peak National Observatories (KPNO) Mayall 4m telescope on 1996 April 9 in the course of spectroscopic observations for X-ray sources detected in the *ASCA* Lynx Deep Survey. We used grism 730 and covered the spectral range from 6000Å to 9000Å with a resolution of 22Å. We used $2.''5$ wide slit. The spectral sampling was 4.3Å pixels^{-1}, and the spatial resolution was $0.''8$ pixels^{-1}. The FWHM of the seeing was $\sim 1''$. The exposure time was 30 minutes. A galaxy in the error circle shows strong Hα, [NII] 6548Å, 6583Å, and [SII] 6717Å, 6731Å with redshift of 0.072. In order to obtain a spectrum in a blue region, we made another spectroscopic observation for the galaxy with KPNO 2.1m telescope and the Goldcam spectrograph on 1997 June 8. Three 30 minute exposures were taken through a $1.''9$ slit. The spectra covered the wavelength range from 3866Å to 7511Å, with a spectral resolution of 5.1Å.

Following the pilot observations, spectroscopic observations for remaining objects were made with the University of Hawaii 88″ telescope on March 1998, except for the hardest source (AX J131501+3141(119)), a candidate of galactic star (AX J131850+3326(219)), and the two clusters of galaxies. We used the Wide Field Grism Spectrograph with a grating of 420 rulings mm^{-1} and the blaze wavelength of 6400Å. The spatial resolution was 0.″354 $pixel^{-1}$ and the seeing during the observation was 0.″8 $\sim$ 1″. A slit width of 1.″2 was used. The spectral coverage ranges from 4000Å to 9000Å and the spectral resolution, which is measured by the HgAr lines in comparison frames and night-sky lines in object frames, is 12Å (FWHM). We also took imaging data of each X-ray source with a better angular resolution without filter for finding charts.

We have also done spectroscopic observations with the 3.5m telescope at Calar Alto observatory for a candidate galactic star (AX J131850+3326(219)) and three objects (AX J131831+3341(228), AX J130840+2955(014), and AX J131639+3149(137)) which were already observed in the previous run. We used the MOSCA instrument in a single-slit mode with a g250 grating which has 250 rulings mm^{-1} and a blaze wavelength of 5700Å. The spectral coverage ranges from 4000Å to 8000Å. In the configuration, the sampling was 5.95 Å $pixel^{-1}$. A slit width of 1.″5, which was the same as the FWHM of the seeing, was used. Thus, the spectral resolution was 22Å (FWHM), which was estimated by measuring widths of night sky lines in object frames. The spatial resolution was 0.″32 $pixel^{-1}$.

The data were analyzed using IRAF.[1] After bias subtraction, flat-fielding, and wavelength calibration, optimum extraction method by **apextract** package was used to extract one dimensional spectral data from the two dimensional original data. For the UH data, flux calibrations were done with Feige 34. The flux calibrations did not work well in the wavelength larger than 7000Å and for some data in the wavelength shorter than 5000Å taken at very large zenith distances. For the Calar Alto data, flux calibrations were done with HD84937. The data were affected by fringes in the wavelength longer than 7000Å. Spectral fitting for emission lines was made by the χ^2 minimization method with **specfit** command in **spfitpkg** package in the IRAF. FWHMs of line widths were deconvolved by the spectral resolution shown above.

[1]IRAF is distributed by the National Optical Astronomy Observatories, which is operated by the Association of Universities for Research in Astronomy, Inc. (AURA) under cooperative agreement with the National Science Foundation.

3.2 Results of Optical Identification

Many (25 out of 34) X-ray sources have one optical-counterpart candidate which shows broad permitted-emission lines whose FWHM is larger than those of forbidden-emission lines or 1000 km s^{-1} in their optical spectra. The detected broad lines and line widths are summarized in Table 3.2. This suggests that most of the X-ray sources originate from AGNs.

In the remaining sources, 5 X-ray sources have only an object with narrow-emission lines. For 4 of them (AX J131758+3257(195), AX J131551 +3237(171), AX J131501+3141(119), AX J131210+3048(072)), both the Hα and Hβ regions were observed. We classified these objects, using the [NII] 6583Å-to-Hα and [OIII] 5007Å-to-Hβ line ratios (Osterbrock 1989). All of them show strong [NII] 6583Å line as well as an Hα line and they fall in the region occupied by AGNs. For the remaining one object, AX J130840 +2955(014), spectroscopic observations cover only the Hβ emission line region, because of atmospheric absorption and fringes. It shows a large [OIII] 5007Å-to-Hβ flux ratio and the existence of an AGN is suggested, but the ratio is not large enough to exclude possibility of star-forming galaxy. However, the spectrum shows optical continuum which is dominated by old stellar populations and there is no indication of star-formation activity. Thus, the object is also identified with AGN.

In the 34 X-ray sources, 2 X-ray sources (AX J131551+3237(171) and AX J131724+3203(152)) have an galaxy with an HII-region like optical spectrum in their error circles. But they also have an optical counterpart candidate with AGN activity and a AGN is more plausible as a origin of the X-ray source than a starforming galaxy based on their optical to X-ray flux ratio, thus we identified the X-ray sources with the AGNs.

We list notes on problematic cases, below.

AX J131054+3004(037) The FIRST source (A in Figure 3.3) in the error circle was identified with a narrow-line AGN at a redshift of 0.245. There is also a blue object within the error circle (B) and it was identified with a broad-line AGN at a redshift of 1.577. Because most other X-ray sources whose X-ray spectra are similar to this X-ray source were identified with broad-line AGNs, we assigned the broad-line AGN as the optical counterpart of the X-ray source. It is possible that the narrow-line AGN or both is the origin of the X-ray source.

AX J131639+3149(137) At the position of the FIRST source in the error circle (α=13^{h}16^{m}38.9^s, δ=31°49′57.8″), no optical object brighter than R = 22.5 mag can be seen. The nearest object, which is separated by

Name	No.	σ^a	Coordinate (J2000) X-ray		No.^{b}	Optical		Offset (′)	R^c (mag)	$B-R^c$ (mag)	Selection^d	Classification	z
AX J131822+3347	235	10.0	13 18 22.92	33 47 41.6	A	13 18 23.75	33 47 36.6	0.19	16.35	0.91	P,B	**AGN**^{e}	0.1186
AX J131850+3326	219	9.4	13 18 50.66	33 26 10.0	A	13 18 52.12	33 26 17.9	0.33	9.92	1.97	P	**K-type star**^{f}	
AX J131345+3118	104	7.1	13 13 45.24	31 18 22.7	A	13 13 44.16	31 18 31.2^g	0.27	19.26^h	···	H^i,P,F	**AGN**	0.7887
AX J131249+3112	096	6.3	13 12 49.34	31 12 59.4	A	13 12 48.80	31 13 00.6	0.12	17.85	0.77	H,F,U,B	**AGN**^{j}	1.0549
					B	13 12 51.37	31 13 08.4	0.46	18.17	0.93	B	···	
AX J131831+3341	228	5.7	13 18 31.27	33 41 45.6	A	13 18 31.59	33 41 45.3	0.07	20.60^k	1.12^k	P,F	**AGN**	0.6529
					B	13 18 33.27	33 41 07.7	0.76	18.74	1.00	B	···	
AX J131758+3257	195	5.5	13 17 58.87	32 57 48.6	A	13 18 00.20	32 57 52.1	0.28	17.99^k	1.77^k	P,F	**AGN**	0.2138
					B	13 17 56.89	32 58 00.8	0.46	18.12	0.82	B	Early-type star	
					Z	13 18 00.29	32 57 58.8	0.34	16.44	3.87	···	Late-type star	
AX J131816+3240	183	5.5	13 18 16.08	32 40 56.3	A	13 18 17.59	32 40 53.3	0.32	17.46^k	0.55^k	B	**AGN**	1.6487
AX J131551+3237	171	5.5	13 15 51.60	32 37 30.7^l	A	13 15 50.34	32 37 37.0	0.29	18.12^k	1.62^k	Br	**AGN**	0.1275
					Z	13 15 51.66	32 37 33.4	0.05	20.17^k	1.29^k	···	HII galaxy	0.2135
AX J131805+3349	233	5.5	13 18 05.78	33 49 28.9	A	13 18 05.37	33 49 36.9	0.16	13.38	0.44	F,U,B	**AGN**	0.0345
					B	13 18 08.43	33 49 27.6	0.55	16.58	1.26	P	···	
					C	13 18 02.73	33 49 51.9	0.74	14.55	0.78	U,B	···	
AX J131054+3004	037	5.2	13 10 54.17	30 04 08.0	A	13 10 55.11	30 04 11.5	0.21	17.68	2.01	F	AGN	0.2449
					B	13 10 53.43	30 04 30.0^g	0.40	19.17	0.73	B	**AGN**	1.5774
AX J131831+3320	212	5.2	13 18 31.73	33 20 30.1	A	13 18 31.63	33 20 36.6	0.11	19.70	0.72	P,B	**AGN**	0.5350
AX J131724+3203	152	4.9	13 17 24.31	32 03 24.1	A	13 17 24.06	32 03 45.5	0.36	18.20	0.46	B	HII galaxy	0.0586
					B	13 17 25.98	32 02 59.9	0.54	19.10	0.55	B	**AGN**	0.8489
AX J131521+3159	136	4.7	13 15 21.41	31 59 13.6	A	13 15 20.93	31 59 21.5^g	0.17	17.72^m	···	H,P,U	**AGN**	0.8382
AX J131021+3019	039	4.6	13 10 21.53	30 19 40.8	A	13 10 24.57	30 19 28.3	0.69	18.32	0.52	B	**AGN**^{n}	1.4886
					Z	13 10 22.00	30 19 50.6	0.19	19.42^h	2.13^k	···	No emission line	
AX J131639+3149	137	4.6	13 16 39.22	31 49 38.6	A	13 16 37.91	31 49 52.1	0.36	19.98	−0.01	F^o,B	**AGN**	0.6218
					B	13 16 36.70	31 49 43.3	0.54	18.96	0.80	B	Early-type star	
AX J132032+3326	227	4.5	13 20 32.14	33 26 33.4	A	13 20 31.25	33 26 26.9	0.21	18.28	···	F,E	**Cluster**	···
AX J131501+3141	119	4.5	13 15 00.91	31 41 28.0^l	A	13 15 01.15	31 41 28.1^g	0.05	15.62^k	1.63^k	F	**AGN**	0.072
AX J131156+3054	075	4.4	13 11 56.50	30 54 43.2	A	13 11 56.41	30 54 47.3	0.07	19.25	1.12	P	**AGN**	0.3656
AX J131725+3300	192	4.4	13 17 25.58	33 00 03.2	A	13 17 26.99	33 00 22.6	0.44	16.64	2.25	P	**AGN**	0.1261
AX J131407+3158	127	4.3	13 14 07.25	31 58 30.0	A	13 14 06.40	31 58 44.1	0.30	16.66	1.45	H,P	**AGN**	0.1766
AX J130748+2925	002	4.3	13 07 48.82	29 25 58.1	A	13 07 49.30	29 25 47.8^g	0.20	16.34^h	···	F,P,E	**Cluster**^{p}	0.241
AX J131327+3155	121	4.1	13 13 27.22	31 55 25.3	A	13 13 27.45	31 55 20.8^g	0.09	17.58^h	···	H,F,U	**AGN**^{p}	0.3033
AX J131832+3259	199	4.1	13 18 32.18	32 59 14.3	A	13 18 29.98	32 58 45.9	0.66	16.79	1.24	Br	G-type star	
AX J131529+3117	110	4.0	13 15 29.02	31 17 32.6	A	13 15 28.58	31 17 43.4	0.20	18.79	0.14	P,F^q,U,B	**AGN**	0.4485
AX J131927+3343	238	4.0	13 19 27.14	33 43 12.4	A	13 19 27.16	33 43 12.9	0.01	18.90^k	0.60^k	P,B	**AGN**	0.4156
AX J130926+2952	016	4.0	13 09 29.04	29 52 01.2^l	A	13 09 28.29	29 52 11.1	0.23	19.93^k	1.94^k	P	**AGN**	0.3751
					B	13 09 26.31	29 51 36.1	0.73	14.16	1.00	B	···	
AX J131707+3237	175	3.9	13 17 07.80	32 37 22.4	A	13 17 09.54	32 37 13.5	0.40	18.64	0.88	B	**AGN**	0.7446
					B	13 17 09.75	32 38 02.4	0.78	16.31	0.99	B	···	
AX J131210+3048	072	3.7	13 12 12.72	30 48 21.2^l	A	13 12 12.00	30 48 21.4^g	0.15	18.40^k	2.05^k	F	**AGN**	0.1888
AX J130840+2955	014	3.7	13 08 40.73	29 55 27.1	A	13 08 41.31	29 55 47.4	0.36	17.34	1.81	Br	**AGN**	0.1635
AX J131128+3105	080	3.6	13 11 28.70	31 05 43.1	A	13 11 28.41	31 05 51.7	0.16	17.15	0.54	H,P,U,B	**AGN**	1.3314
					B	13 11 27.34	31 05 43.4	0.29	19.31	0.02	U,B	···	
AX J131321+3119	103	3.6	13 13 21.07	31 19 30.0	A	13 13 20.46	31 19 21.6	0.19	19.81	−0.19	H,U,B	**AGN**	0.8338
AX J131928+3251	197	3.6	13 19 28.37	32 51 03.2	A	13 19 29.89	32 50 45.6	0.43	18.43	0.95	B	**AGN**	0.3107
AX J131015+3004	033	3.5	13 10 15.26	30 04 19.2	A	13 10 16.01	30 04 16.8	0.17	17.90	1.01	P,U	**AGN**	1.1651
AX J130826+3005	023	3.5	13 08 26.42	30 05 40.6	A	13 08 29.66	30 05 39.1	0.70	16.29	0.77	P,U,B	**AGN**^{r}	0.8033

Table 3.1: Candidates of Optical Counterparts and Results of Identifications

Notes:

a: Detection significances in the SIS 2–7 keV band.

b: Identification numbers of optical objects in Figure 3.1. A, B, and C are selected targets in order of a distance from an X-ray center. Z is an additional object which was spectroscopically observed.

c: Coordinates and magnitudes are taken from APM catalog (McMahon et al. 1992), except for objects with notes.

d: Selection methods of candidates of optical counterparts. H:*ROSAT* HRI, P:*ROSAT* PSPC (Voges et al. 1998), F:FIRST (Becker, White, & Helfand 1995), E:Galaxy excess, U:UV excess (Usher 1981; Moreau & Reboul 1995; Takase & Miyauchi-Isobe 1986), B:Blue color, Br:Brightest object in the error circle. For detail, see Section 2.2.

e: Already cataloged in Bade et al. (1998)

f: Already cataloged as HD115781.

g: Coordinate determined by CCD image taken during the spectroscopic observations.

h: Determined by relative photometry with mosaic CCD image taken at KISO observatory.

i: In the *ROSAT* HRI image, there is an X-ray peak whose significance level is slightly lo wer than the detection limit.

j: Already cataloged in Falco, Kochanek, & Munoz (1998).

k: Determined by CCD photometry done at University of Hawaii 88″ telescope in March 1996 and March 1999.

l: X-ray positions were determined by deep pointing observations by *ASCA* (Sakano et al. 1998; Sakano et al. 1999; Ueda et al. 1999b).

m: APM magnitude data is blended.Deblending was done using CCD image taken during the spectroscopic observations.

n: Already cataloged in Schade (1991).

o: The nearest object to a FIRST radio source. The radio source is 14″ offsetted from the optical object. See notes in Section 3.2.

p: Identified in the *Einstein* Medium Sensitivity Survey (Stocke et al. 1991).

q: In the FIRST radio map, there is a radio peak whose significance level is slightly lower than the detection limit.

r: Already cataloged in Wills & Wills (1976).

Name	No.	P.I.[a]	$F^b_{\rm XH}$	$L^c_{\rm XH}$	$F^d_{\rm XS}$	$L^e_{\rm XS}$	$N^f_{\rm H}$	R	M^g_V	$S^h_{\rm peak}$	$L^i_{\rm R}$	
AX J131822+3347	235	2.08 ± 0.07	12.71	43.91	9.20	43.77	<0.0056	16.35	−22.69	···	<22.78	AGN
AX J131850+3326	219	2.65 ± 0.09	3.10	···	5.16	···	···	9.92	···	···	···	K-type star
AX J131345+3118	104	1.69 ± 0.14	2.39	44.84	1.22	44.55	$0.005^{+0.419}_{-0.005}$	19.26	−23.87	2.13	24.75	AGN
AX J131249+3112	096	1.62 ± 0.13	3.70	45.27	1.47	44.87	$0.345^{+0.632}_{-0.345}$	17.85	−25.90	90.08[o]	26.62	AGN (RL)
AX J131831+3341	228	1.45 ± 0.14	5.81	45.01	2.01	44.55	$0.583^{+0.443}_{-0.416}$	20.60	−22.13	2.03	24.56	AGN
AX J131758+3257	195	1.64 ± 0.15	2.47	43.70	0.93	43.27	$0.045^{+0.192}_{-0.045}$	17.99	−22.33	3.51	23.84	AGN
AX J131816+3240	183	1.33 ± 0.16	2.24	45.32	0.55	44.72	$3.217^{+1.958}_{-1.758}$	17.46	−27.23	···	<25.04	AGN
AX J131551+3237	171	0.32 ± 0.34	2.61	43.20	0.15	41.95	$1.9^{+1.3}_{-1.0}$[p]	18.12	−21.08	···	<22.84	AGN
AX J131805+3349	233	1.68 ± 0.21	3.80	42.29	1.98	42.01	$0.134^{+0.185}_{-0.134}$	13.38	−22.98	1.46	21.87	AGN
AX J131054+3004	037	1.58 ± 0.19	1.91	45.32	0.98	45.03	$1.685^{+2.008}_{-1.685}$	19.17	−25.43	···	<25.00	AGN
AX J131831+3320	212	1.83 ± 0.11	2.63	44.57	0.92	44.11	<0.218	19.70	−22.60	···	<24.08	AGN
AX J131724+3203	152	1.23 ± 0.22	1.67	44.63	0.50	44.11	$1.588^{+1.074}_{-0.945}$	19.10	−24.19	···	<24.48	AGN
AX J131521+3159	136	1.86 ± 0.16	2.55	44.97	1.30	44.68	<0.191	17.72	−25.54	···	<24.47	AGN
AX J131021+3019	039	1.24 ± 0.21	2.31	45.22	0.54	44.59	$5.120^{+2.642}_{-2.257}$	18.32	−26.16	···	<24.96	AGN
AX J131639+3149	137	1.72 ± 0.21	1.30	44.37	0.59	44.03	$0.070^{+0.508}_{-0.070}$	19.98	−22.64	64.55	26.02	AGN (RL)
AX J132032+3326	227	1.96 ± 0.16	2.56	···	1.60	···	···	18.28	···	18.44[o]	24.50	Cluster
AX J131501+3141	119	-0.68 ± 0.45	4.78	42.96	0.06	41.09	$6.4^{+3.1}_{-2.3}$[p]	15.62	−22.34	3.74	22.92	AGN
AX J131156+3054	075	1.55 ± 0.26	0.79	43.66	0.49	43.45	$0.197^{+0.439}_{-0.197}$	19.25	−22.23	···	<23.76	AGN
AX J131725+3300	192	1.52 ± 0.21	1.74	43.08	0.44	42.48	$0.247^{+0.243}_{-0.221}$	16.64	−22.53	···	<22.83	AGN
AX J131407+3158	127	1.76 ± 0.23	1.37	43.28	0.87	43.08	<0.194	16.66	−23.24	···	<23.13	AGN
AX J130748+2925	002	1.96 ± 0.16	4.14	44.06	2.93	43.91	···	16.34	···	2.80	23.84	Cluster
AX J131327+3155	121	1.76 ± 0.17	3.05	44.11	1.24	43.72	<0.165	17.58	−23.49	72.24[o]	25.45	AGN (RL)
AX J131832+3259	199	0.58 ± 0.35	1.41	···	0.19	···	···	···	···	···	···	No ID
AX J131529+3117	110	2.11 ± 0.23	1.37	44.17	1.34	44.16	<0.101	18.79	−23.13	0.63	23.72	AGN
AX J131927+3343	238	1.48 ± 0.21	2.09	44.18	0.61	43.65	$0.365^{+0.443}_{-0.365}$	18.90	−22.86	···	<23.87	AGN
AX J130926+2952	016	0.81 ± 0.30	1.47	43.85	0.16	42.88	$2.3^{+1.8}_{-1.2}$[p]	19.93	−21.60	···	<23.78	AGN
AX J131707+3237	175	1.95 ± 0.24	1.32	44.60	0.93	44.44	<0.240	18.64	−24.37	···	<24.37	AGN
AX J131210+3048	072	0.76 ± 0.31	1.76	43.37	0.28	42.57	$1.1^{+0.9}_{-0.6}$[p]	18.40	−21.65	1.92	23.47	AGN
AX J130840+2955	014	0.34 ± 0.44	1.39	43.13	0.15	42.16	$2.857^{+1.191}_{-1.114}$	17.34	−22.40	···	<23.06	AGN
AX J131128+3105	080	1.65 ± 0.24	1.41	45.08	0.36	44.49	<1.430	17.15	−27.09	···	<24.86	AGN
AX J131321+3119	103	1.54 ± 0.18	2.36	44.85	0.71	44.33	$0.252^{+0.695}_{-0.252}$	19.81	−23.44	···	<24.46	AGN
AX J131928+3251	197	1.65 ± 0.26	1.19	43.71	0.50	43.33	$0.055^{+0.386}_{-0.055}$	18.43	−22.70	···	<23.62	AGN
AX J131015+3004	033	1.70 ± 0.19	2.17	45.16	0.81	44.73	<0.622	17.90	−26.06	···	<24.75	AGN
AX J130826+3005	023	1.83 ± 0.17	2.84	44.97	1.56	44.71	<0.334	16.29	−26.88	···	<24.43	AGN

Table 3.2: Photometric and Spectroscopic Properties of the Identified Objects

Notes:

a: X-ray power-law photon index determined in the 0.7–10 keV band with GIS and SIS.

b: 2–10 keV flux in 10^{-13} erg cm^{-2} s^{-1} derived from the GIS data. Conversions from count rates were done based on the best fit power-law indices.

c: Logarithmic 2–10 keV luminosity in erg s^{-1}. k-correction was made with the measured photon index.

d: 0.5–2 keV flux in 10^{-13} erg cm^{-2} s^{-1} derived from the GIS data. Conversions from count rates were done based on the best fit power-law indices.

e: Logarithmic 0.5–2 keV luminosity in erg s^{-1}. k-correction was made with the measured photon index.

f: The best-fit intrinsic column densities from absorption fitting in unit of 10^{22} cm^{-2}. The intrinsic photon index of 1.7 and the absorption at the object redshift are assumed. The errors indicate 1σ error regions.

z	Note	Detected Broad Lines	Hα FWHM[k] (km s^{-1})	Hβ FWHM[k] (km s^{-1})	MgII FWHM[k] (km s^{-1})	log(Hα/[NII])[l]	log(Hβ/[OIII])[m]	MgII EW (Å)
0.1186	S+D	Hδ,Hγ,Hβ,Hα	569,3397[n]	867,5233[n]	···	$1.31^{+0.08}_{-0.07}$	$0.52^{+0.07}_{-0.08}$	···
	S							
0.7887	S	MgII2800Å	···	···	9695	···	···	83
1.0549	S	MgII2800Å	···	···	6854	···	···	29
0.6529	S+D	MgII2800Å	···	849	8684	···	$-0.54^{+0.53}_{-0.73}$	99
0.2138	G	Only Narrow Line	666	768	···	$0.28^{+0.55}_{-0.29}$	<−0.63	···
1.6487	S	CIII]1909Å,MgII2800Å	···	···	6949	···	···	33
0.1275	G	Only Narrow Line	<486	<657	···	$0.35^{+0.12}_{-0.14}$	$-0.45^{+0.10}_{-0.15}$	···
0.0345	G	Hα	<530,5817[n]	···	···	$1.03^{+0.11}_{-0.10}$	<−0.63	···
1.5774	S	CIII]1909Å,MgII2800Å	···	···	6136	···	···	50
0.5350	S	MgII2800Å,Hγ,Hβ	···	647,9988[n]	···	···	$0.55^{+0.09}_{-0.09}$	···
0.8489	S	MgII2800Å	···	···	7804	···	···	69
0.8382	S	MgII2800Å	···	···	6661	···	···	29
1.4886	S	CIII]1909Å,MgII2800Å	···	···	1999	···	···	17
0.6218	S	MgII2800Å	···	···	8486	···	···	59
···								
0.072	G	Only Narrow Line	325	325	···	$0.06^{+0.10}_{-0.10}$	$-0.65^{+0.10}_{-0.10}$	···
0.3656	S	Hβ	···	<542,4711[n]	···	···	$0.33^{+0.31}_{-0.18}$	···
0.1261	G	Hα	<487,4966[n]	<658	···	$1.18^{+0.26}_{-0.23}$	$-0.34^{+0.25}_{-0.16}$	···
0.1766	G	Hβ,Hα	<466,3196[n]	3984	···	$0.82^{+0.12}_{-0.11}$	$-0.46^{+0.11}_{-0.14}$	···
0.241								
0.3033	S	Hβ	···	4088	···	···	$0.29^{+0.16}_{-0.17}$	···
0.4485	S	Hδ,Hγ,Hβ	···	840,4094[n]	···	···	$0.20^{+0.05}_{-0.06}$	···
0.4156	S	Hδ,Hγ,Hβ	···	<523,3711[n]	···	···	$0.15^{+0.06}_{-0.07}$	···
0.3751	G	Hβ	···	696,1791[n]	···	···	$-0.59^{+0.18}_{-0.34}$	···
0.7446	S	MgII2800Å	···	···	1485,7886[n]	···	$0.45^{+0.55}_{-0.52}$	25[n]
0.1888	G	Only Narrow Line	<461	<630	···	$0.08^{+0.40}_{-0.09}$	<−0.53	···
0.1635	G	Only Narrow Line	···	···	···	···	<−0.63	···
1.3314	S	CIII]1909Å,MgII2800Å	···	···	7807	···	···	29
0.8338	S	MgII2800Å	···	···	8073	···	···	41
0.3107	G	Hγ,Hβ	···	2946	···	···	$-0.29^{+0.09}_{-0.10}$	···
1.1651	S	MgII2800Å	···	···	5859	···	···	25
0.8033	S	MgII2800Å	···	···	4854	···	···	17

g: Optical V-band absolute magnitude derived in assumption of optical power-law index of −0.5 which corresponds to $V - R$ color of 0.22mag.

h: Radio peak flux at 1.4GHz in mJy from FIRST radio catalog.

i: Logarithmic radio luminosity at 1.4GHz in W Hz^{-1}. K-correction was made with power-law index of −0.5. Upper limit was estimated using the flux limit of 1mJy.

j: Notes on optical images of the objects. S:Stellar, S+D:Stellar component with faint nebulosity, and G:Galaxy.

k: FWHMs are corrected for the instrumental broadening with the spectral resolution of 12Å.

l: Logarithmic equivalent width ratio of broad-plus narrow-Hα lines-to-narrow [NII]6583Å line.

m: Logarithmic equivalent width ratio of broad-plus narrow-Hβ lines-to-narrow [OIII]5007Å line.

n: Fitted with 2 components.

o: Summed flux of multi components.

p: Determined from deep follow-up observations with *ASCA* (Sakano et al. 1998; Sakano et al. 1999; Ueda et al. 1999b).

14″ from the radio position and has a blue color, was identified with a broad-line AGN at z=0.622. The projected distance between radio and optical source corresponds to 108 kpc at the redshift. If we assume that the radio emission is originated from the object, the radio-to-X-ray flux ratio corresponds to that of radio-loud objects (see Section 5.2).

AX J131832+3259(199) The brightest stellar object (A in Figure 3.3) in the 0.′8 error circle was identified with a G-type star. Based on an X-ray-to-optical flux ratio of a G-type star, this object cannot be the origin of the X-ray source. This source is not identified yet.

As a result, 34 X-ray sources in the SIS 2–7 keV 3.5σ sample were identified with 30 AGNs including 5 objects with only narrow-emission lines, 2 clusters of galaxies, and 1 galactic star. Only 1 source is still unidentified. The resulting identification and classification for each X-ray source is indicated with bold characters in Table 3.1. The optical spectra of the identified objects are shown in Figure 3.3. Detected broad-lines in each object are listed in Table 3.2. Physical parameters of the identified objects are also summarized in Table 3.2. In the next section, we discuss the reliability of the identification.

3.3 Reliability of the Identification

3.3.1 Contamination

Figure 3.1 shows the distribution of optically identified objects in the X-ray error circles. Almost all X-ray sources were identified with optical objects within 0.′6, though we picked up the candidates within 0.′8. This result confirms the estimated 90% confidence error radius (0.′6) of the SIS 2–7 keV 3.5σ sample.

First, to examine the reliability of our selection methods of optical counterpart candidates with radio emission, UV excess, and optical color, we compared the number of objects which are selected with the three methods but not identified with X-ray sources (Table 3.3, colum 5 and 6) with the expected number of contamination of objects which meet either of the three criteria but are not X-ray source (Table 3.3, colum 7 and 8). The expected number of contamination is estimated, based on surface number density of radio sources, UV excess objects, and blue color objects (see Section 2.2.3 and 2.2.4). The number of the non-X-ray objects agree with the expected number of contamination. Thus, misidentification of a radio source, UV-

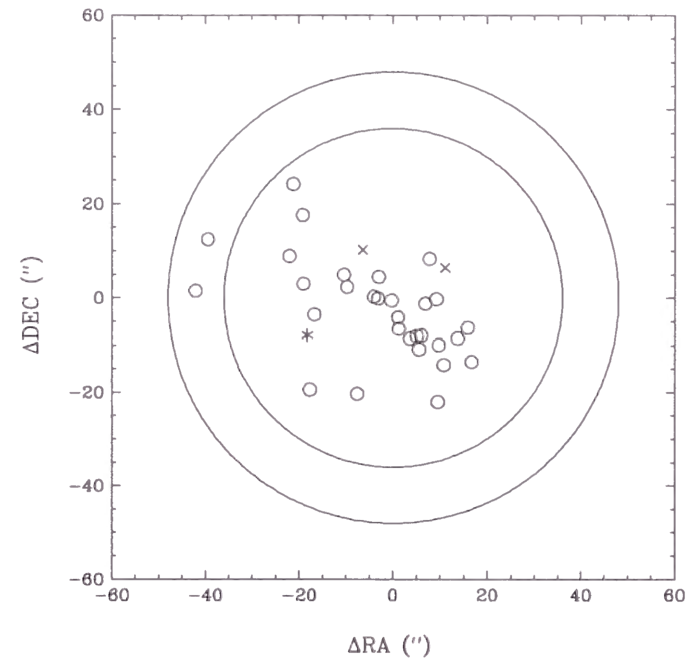

Figure 3.1: The distribution of the identified objects within the X-ray error circles. Open circles, crosses, and an asterisk represent AGNs, clusters of galaxies, and a galactic star, respectively. Inner and outer circles have radii of 0.′6 and 0.′8. The inner circle corresponds to the estimated error radius of the LSS X-ray sources in the 90% confidence level.

excess object, and blue object which are not true X-ray source as an optical counterpart is not serious.

We also checked the reliability of our identification by estimating chance contamination of broad-line AGN in the error circle. Based on number counts of optically-selected broad-line AGN brighter than B = 21.0 mag with a redshift smaller than 3 (Hartwick and Schade 1990), the expected number of chance contamination of broad-line AGN within 34 error circles is 0.29 and is negligible.

3.3.2 X-ray-to-optical Flux Ratio

An X-ray-to-optical flux ratio is one of useful tools to check the reliability of identification. To compare the X-ray-to-optical flux ratios of identified objects with $\log f_X/f_V$ of the *Einstein* Medium Sensitivity Survey (EMSS) sample (Stocke et al. 1991), we plot the relation between optical magnitude and hard X-ray flux in Figure 3.2. To plot the equal $\log f_X/f_V$ lines, we converted the V band magnitude to the R band magnitude and 0.3–3.5 keV

	X-ray Source	Selected Candidates		Not Optical Counterpart		Expected Contamination	
		in	out	in	out	in	out
FIRST	34	17	0	1	0	0.76	0.60
UV	20	8	1	1	0	0.28	0.22
Blue	34	19	6	5	4	6	5

Table 3.3: Comparison of the number of objects which are selected with a methods but not identified with X-ray source with the expected number of contamination. Column 1: Selection methods. Column 2: Number of X-ray sources in an area covered by the each selection method. The UV surveys do not cover the whole LSS area. Column 3 and 4: Number of radio sources, UV-excess objects, and blue objects within $r < 0.''6$ and in outer anuli $0.''6 < r < 0.''8$. Column 5 and 6: Number of radio sources, UV-excess objects, and blue objects which are not counterpart of X-ray source. Number in the left colum is within $r < 0.''6$ and right colum is in outer anuli $0.''6 < r < 0.''8$. Column 7 and 8: Expected number of contamination of radio sources, UV-excess objects, and blue objects. Number in the left colum is within $r < 0.''6$ and right colum is in outer anuli $0.''6 < r < 0.''8$.

flux to 2–10 keV flux for the EMSS sample, using a $V - R$ color of 0.22 mag, which is equivalent to a typical optical energy index of broad line AGNs (-0.5) and a photon index of 1.7 in the 0.3–10 keV band, respectively. The $\log f_X/f_V$ values of the EMSS AGNs, clusters of galaxies, and galactic G-type stars are distributed -1.0 to $+1.2$, -0.5 to $+1.5$, and -4.3 to -2.4 (Stocke et al. 1991), respectively. In the fainter flux range, the AGNs detected in the *ROSAT* HRI Lockman Hole Deep survey also occupy the same value of $\log f_X/f_V$ (Schmidt et al. 1998). The $\log f_X/f_V$ values of the identified AGNs, clusters of galaxies, and a galactic star in our sample are consistent with the distribution of the EMSS sample. The consistency of $\log f_X/f_V$ with the EMSS objects supports the reliability of the identification in the LSS sample.

However, there are two AGNs which have values of $\log f_X/f_V$ slightly outside of the EMSS sample. One AGN (AX J131831+3341(228)) has a $\log f_X/f_V$ value of $+1.3$, which is X-ray louder than the EMSS AGNs. The AGN has a strong narrow [OIII] 5007Å line compared with the broad Hβ line. Thus, the large $\log f_X/f_V$ value might be explained by an optical absorption of its nucleus. The other AGN (AX J131805+3349(233)), whose $\log f_X/f_V$ is smaller than -1.0, is dominated by its host galaxy in the optical light (see Figure 3.3) and this component makes the object optically brighter in comparison with other AGNs. The lower limit of $\log f_X/f_V$ on the optical counterpart of the unidentified source, AX J131832+3259(199), is $\sim +1$. This value is consistent with that of the EMSS AGNs.

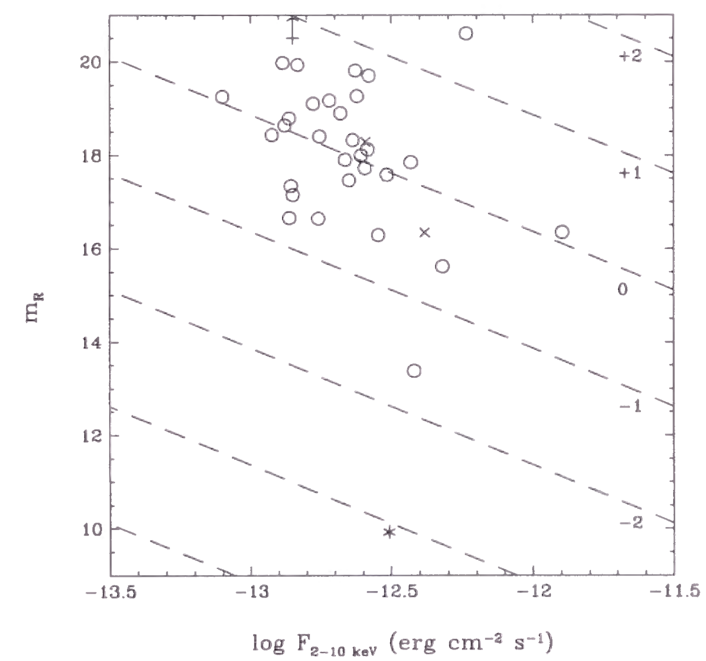

Figure 3.2: 2–10 keV flux versus optical R band magnitude diagram of the identified objects. Open circles, crosses, and an asterisk represent AGNs, clusters of galaxies, and a galactic star, respectively. The upper limit of the optical magnitude of AX J131832+3259(199) is indicated with a plus sign with an upward arrow. Dashed lines represent X-ray-to-optical flux ratio of $\log f_X/f_V = +2, +1, 0, -1, -2, -3$, and -4 from top to bottom.

Figure 3.3: Optical finding charts and spectra of identified objects. The field of view of the finding charts is 1.′6 × 1.′6. Large circles have a radius of 0.′6 and correspond to the 90% confidence error circles of ASCA sources. Middle and small size circles have radii of 20″ and 5″ and correspond to error circles of *ROSAT* PSPC and HRI sources, respectively. Positions of FIRST radio sources are indicated by small rectangles. Objects which have an UV-excess or a blue $B-R$ colors are marked with pentagons. The objects listed in Table 2 are labeled with "A", "B", "C", and "Z". The spectrum of each identified object is shown with the identification label and classification. Positions of atmospheric absorption lines are shown as a cross with a circle.

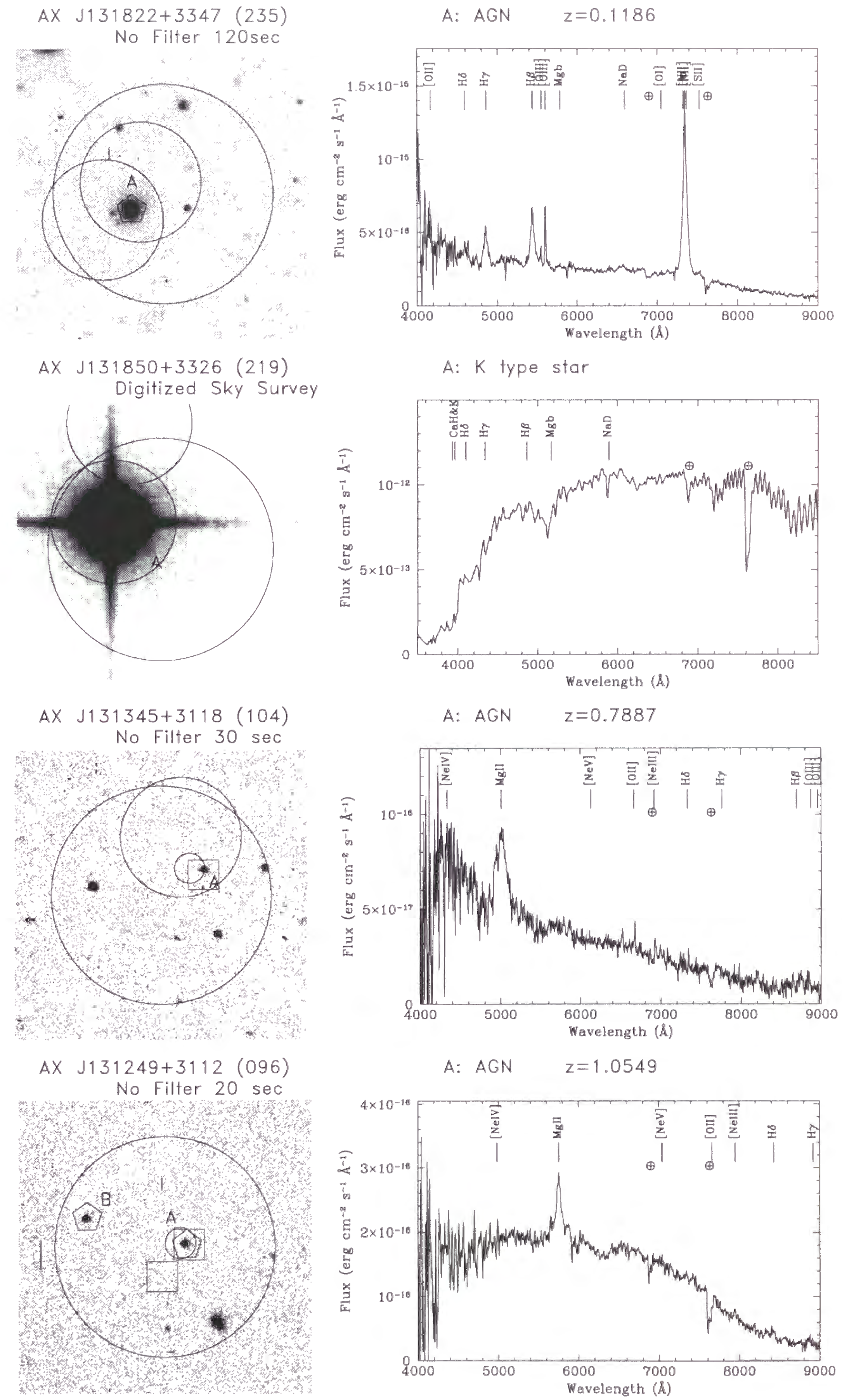

AX J131831+3341 (228)
No Filter 180 sec

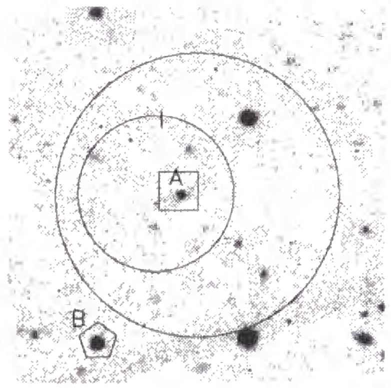

A: AGN z=0.6529

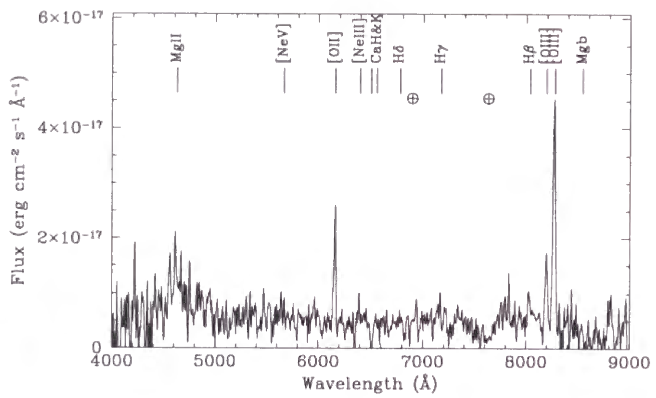

AX J131758+3257 (195)
No Filter 120 sec

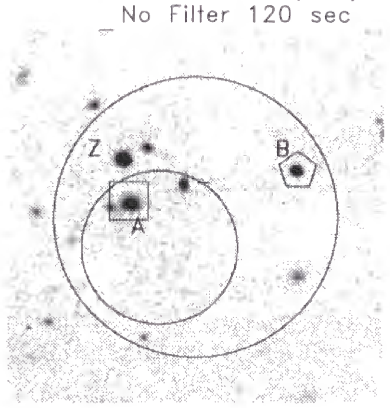

A: AGN z=0.2138

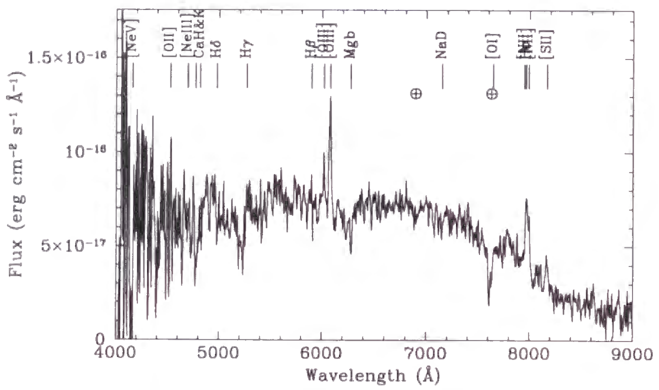

AX J131816+3240 (183)
R band 1200 sec

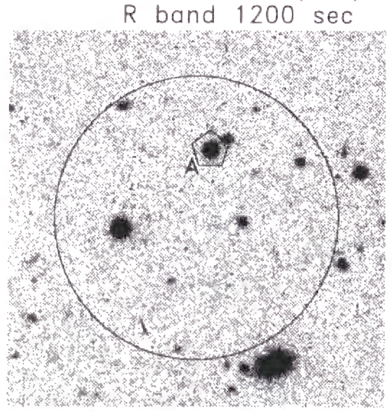

A: AGN z=1.6487

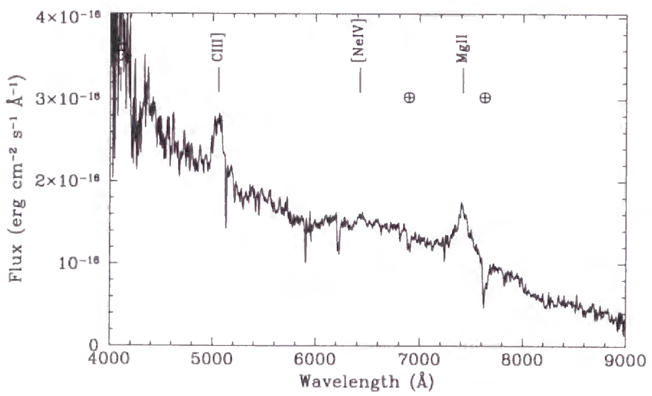

AX J131551+3237 (171)
R band 1200 sec

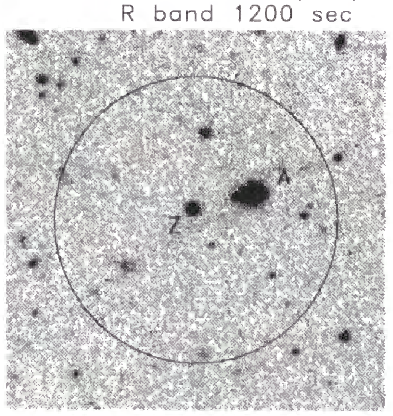

A: AGN z=0.1275

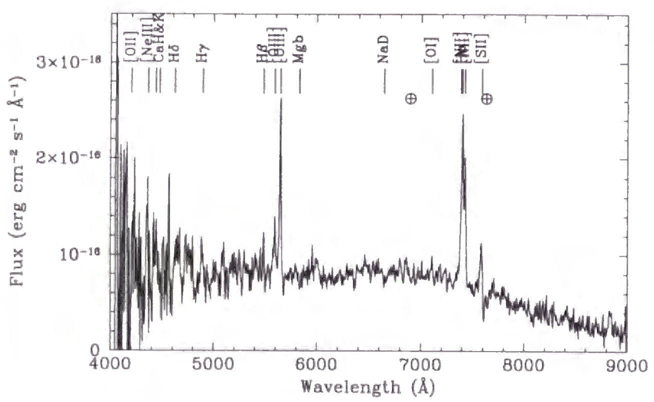

AX J131805+3349 (233)
No Filter 30 sec

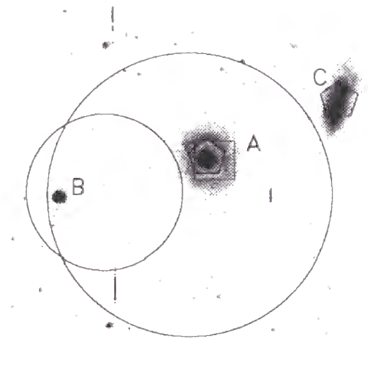

A: AGN z=0.0345

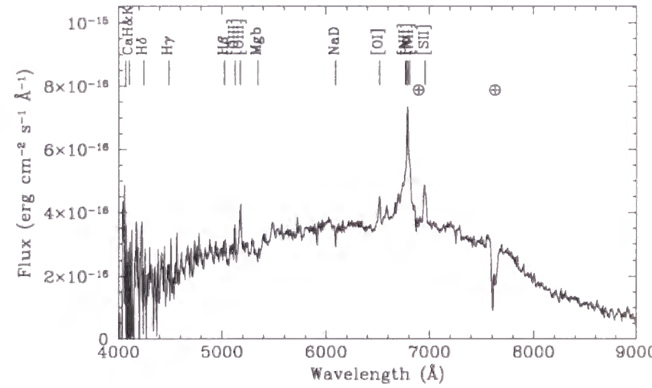

AX J131054+3004 (037)
No Filter 30 sec

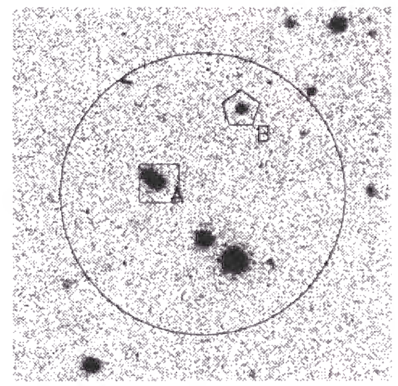

A: AGN z=0.2449

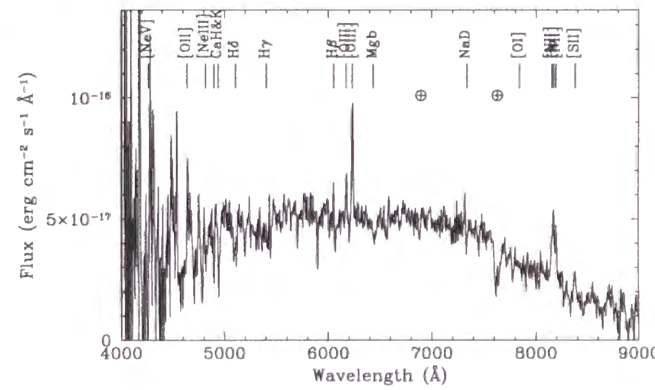

B: AGN z=1.5774

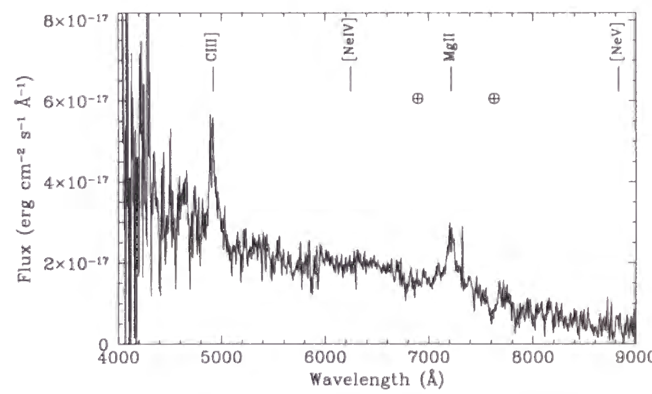

AX J131831+3320 (212)
No Filter 300 sec

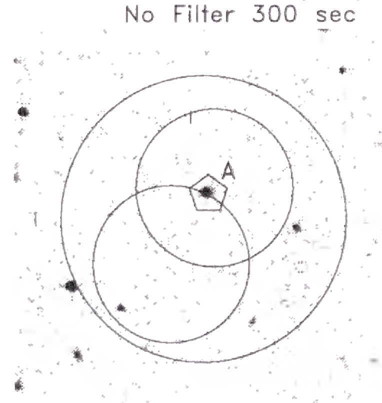

A: AGN z=0.5350

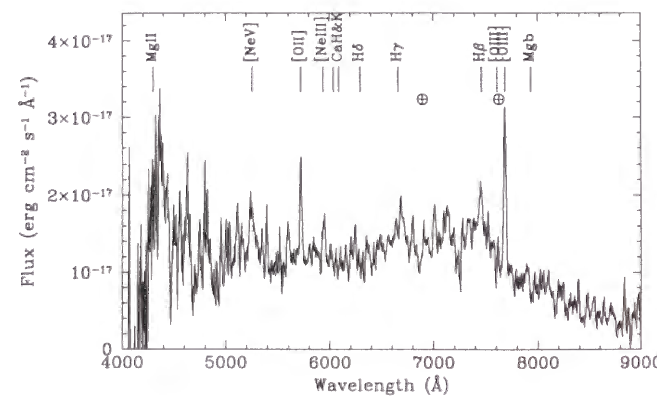

AX J131724+3203 (152)
No Filter 30 sec

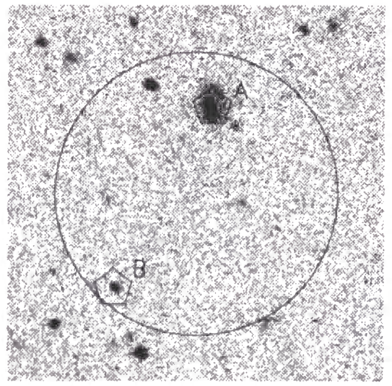

B: AGN z=0.8489

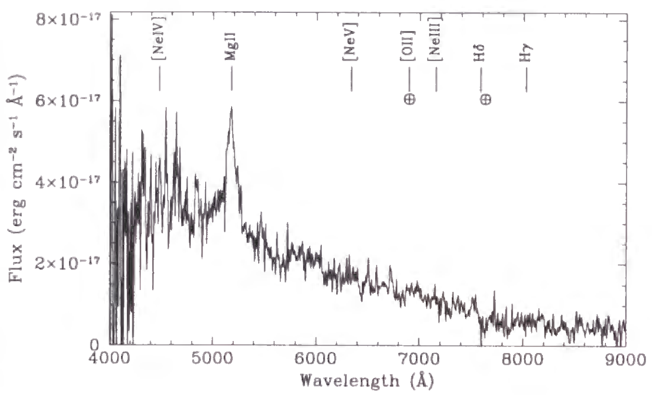

AX J131521+3159 (136)
No Filter 20 sec

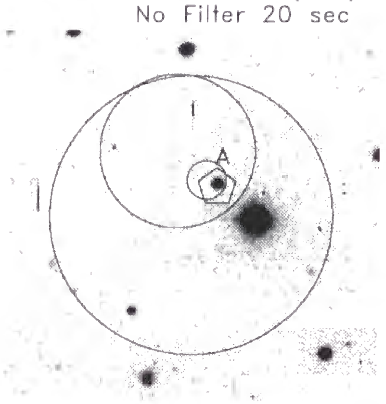

A: AGN z=0.8382

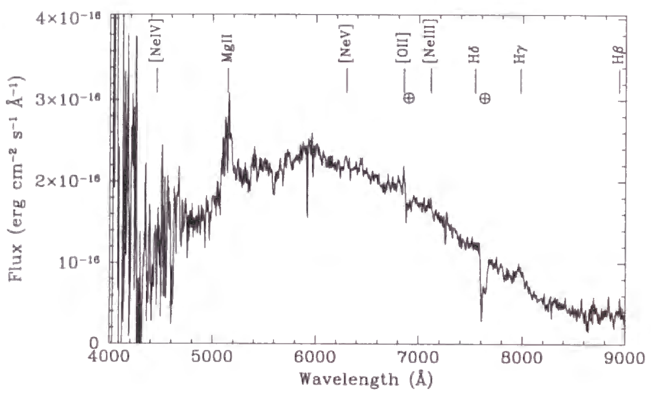

AX J131021+3019 (039)
No Filter 30 sec

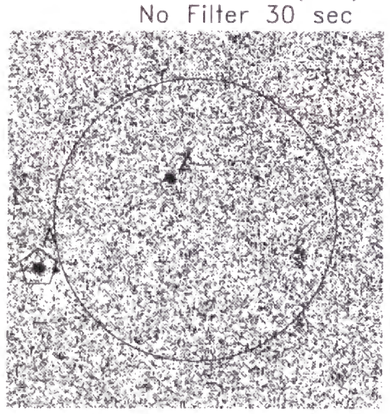

A: AGN z=1.4886

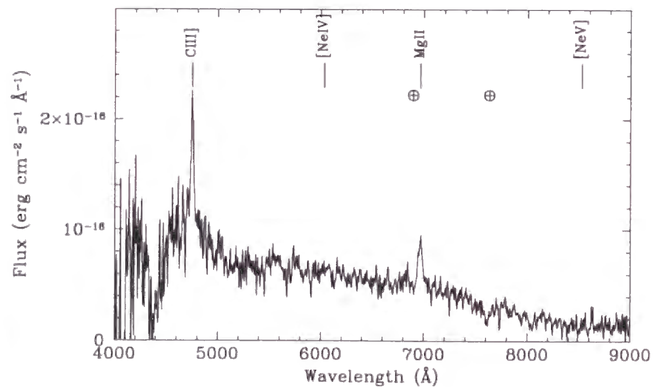

AX J131639+3149 (137)
No Filter 180 sec

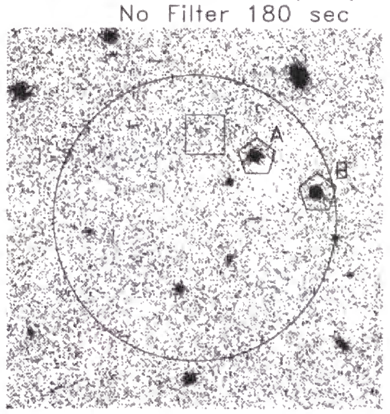

A: AGN z=0.6218

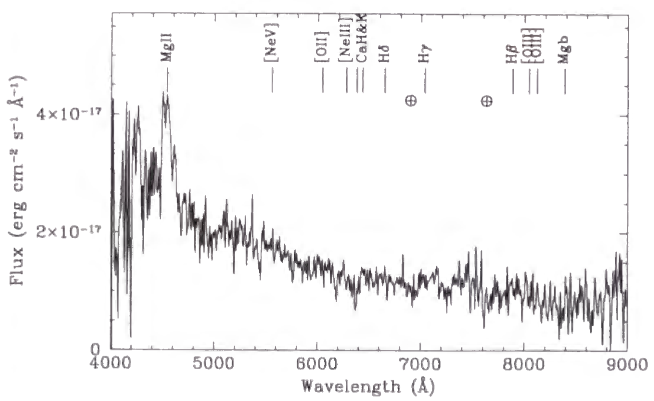

AX J132032+3326 (227)
R band 1200 sec

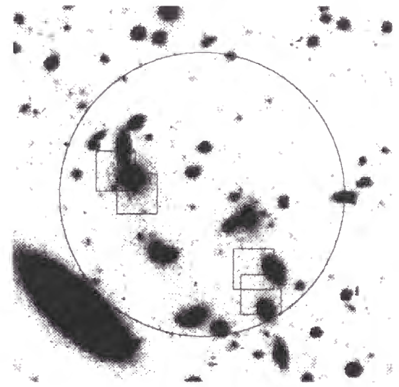

Cluster of Galaxies

AX J131501+3141 (119)
R band 1200 sec

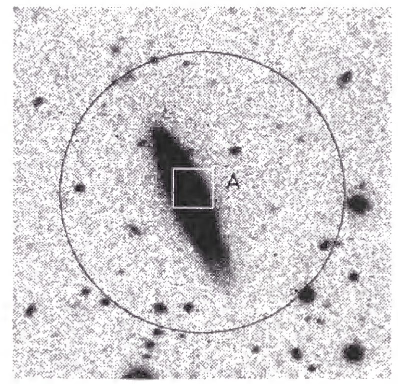

A: AGN z=0.072

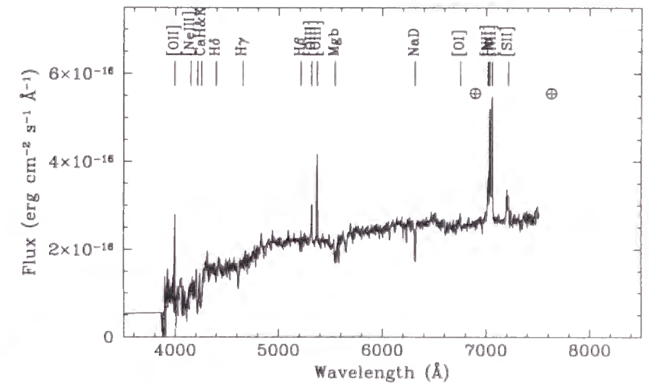

AX J131156+3054 (075)
No Filter 180 sec

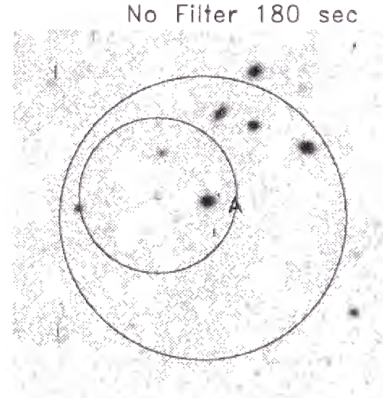

A: AGN z=0.3656

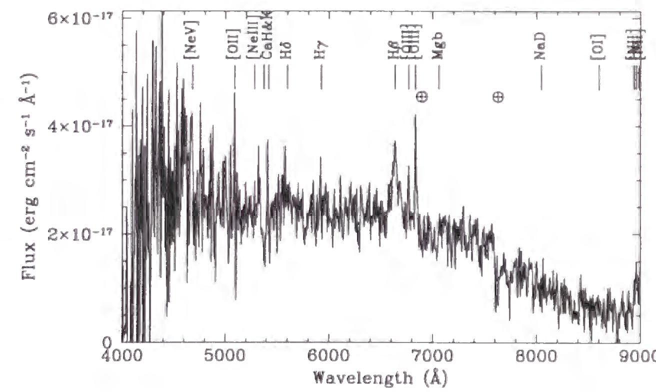

AX J131725+3300 (192)
No Filter 30 sec

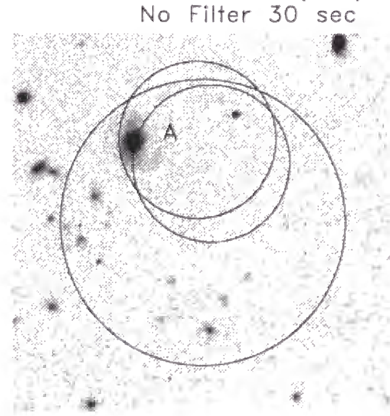

A: AGN z=0.1261

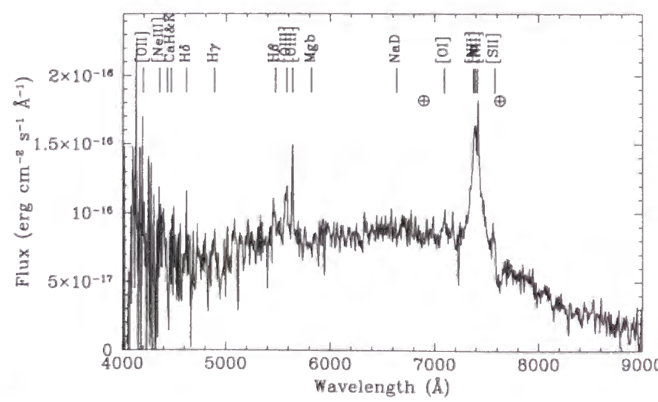

AX J131407+3158 (127)
No Filter 30 sec

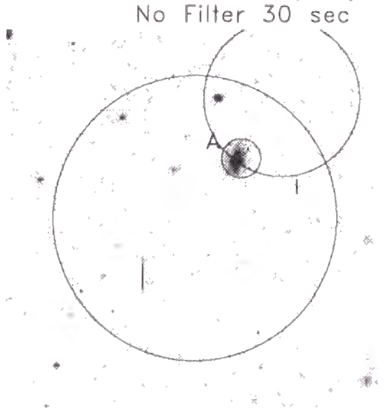

A: AGN z=0.1766

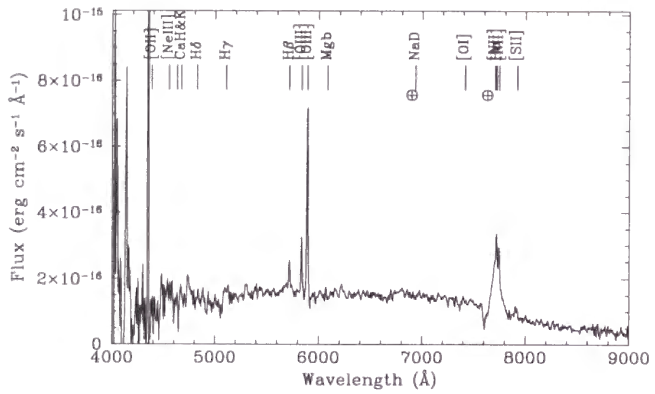

AX J130748+2925 (002)
R band 1200 sec

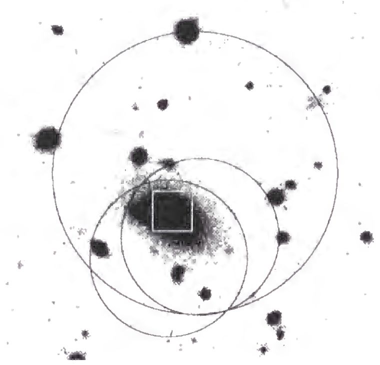

Cluster of Galaxies z=0.241

AX J131327+3155 (121)
No Filter 30 sec

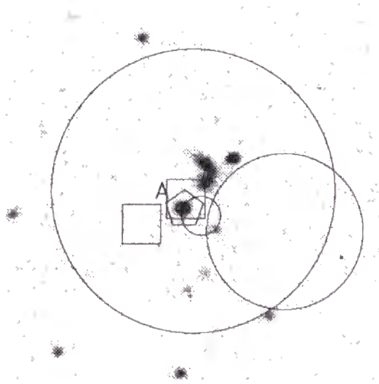

A: AGN z=0.3033

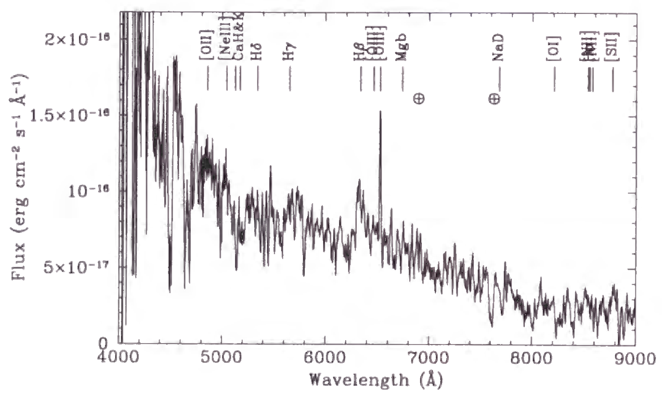

AX J131832+3259 (199)
No Filter 300 sec

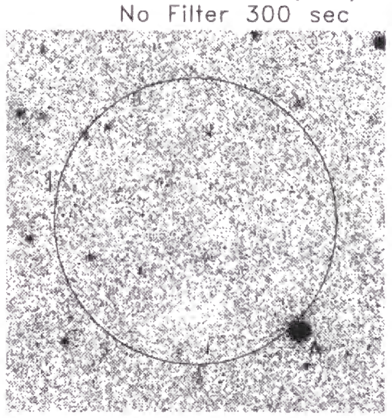

AX J131529+3117 (110)
No Filter 30 sec

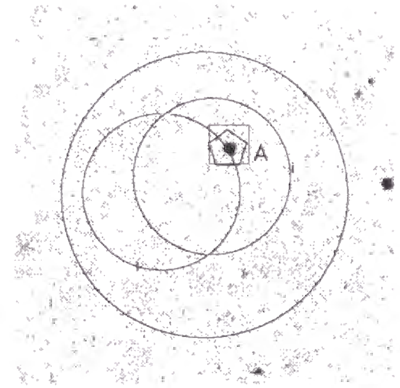

A: AGN z=0.4485

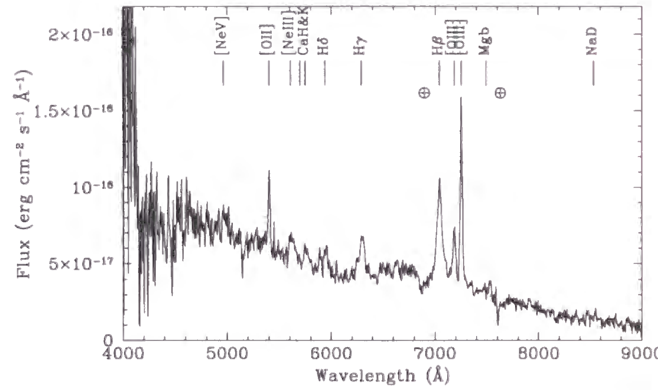

AX J131927+3343 (238)
R band 1200 sec

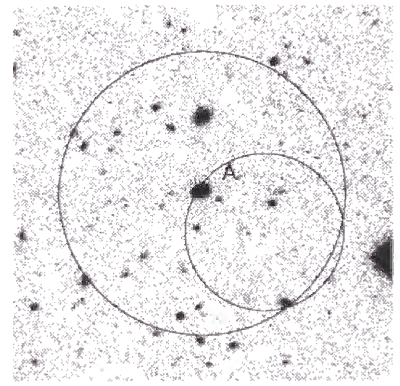

A: AGN z=0.4156

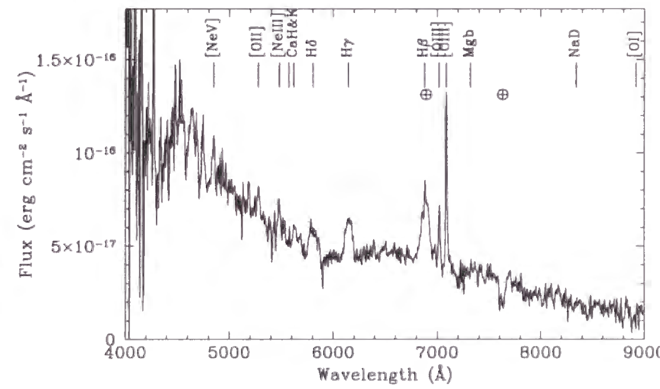

AX J130926+2952 (016)
No Filter 300 sec

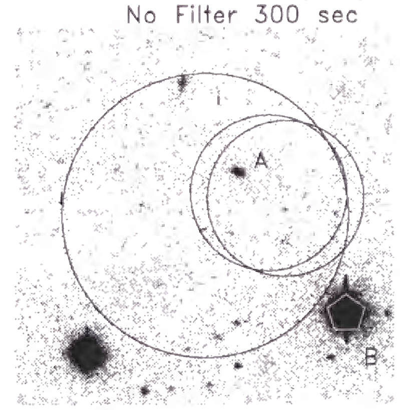

A: AGN z=0.3751

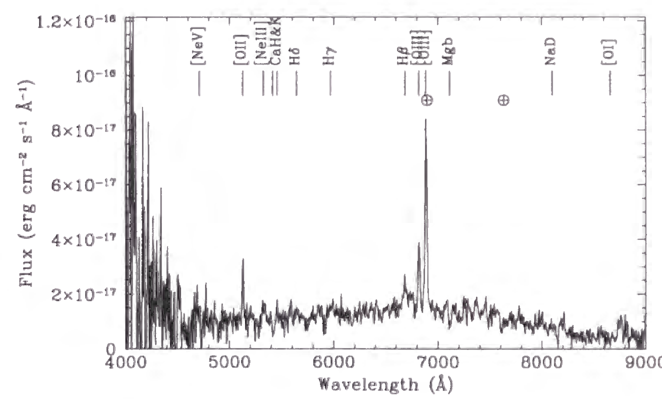

AX J131707+3237 (175)
No Filter 30 sec

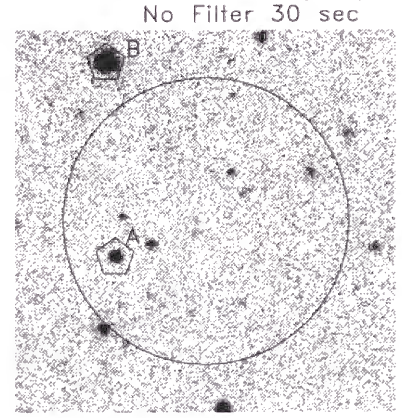

A: AGN z=0.7446

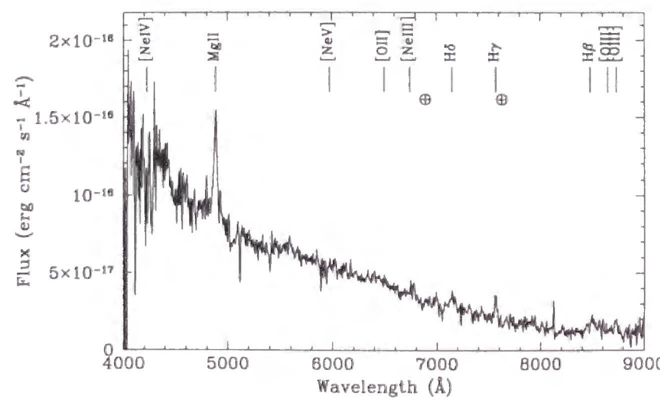

AX J131210+3048 (072)
No Filter 30 sec

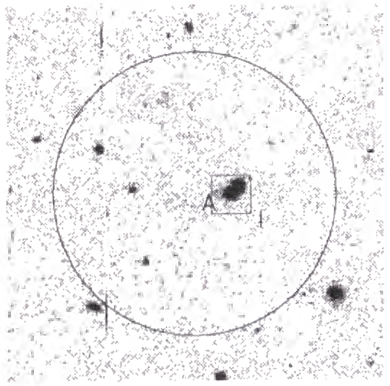

A: AGN z=0.1888

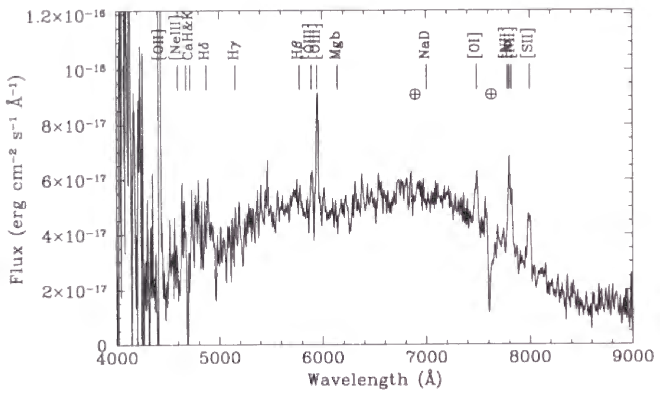

AX J130840+2955 (014)
No Filter 30 sec

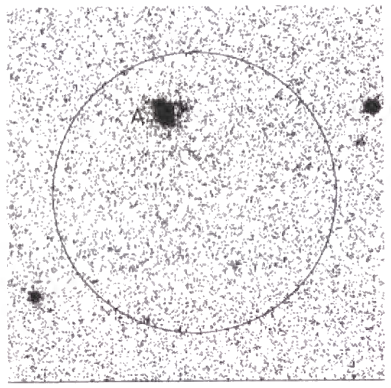

A: AGN z=0.1635

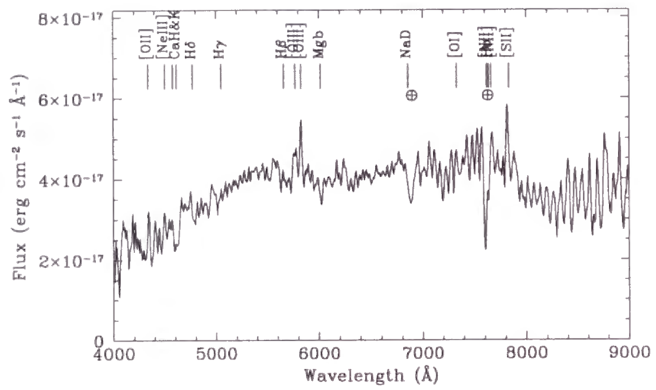

AX J131128+3105 (080)
No Filter 30 sec

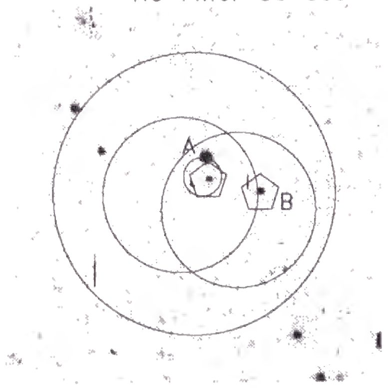

A: AGN z=1.3314

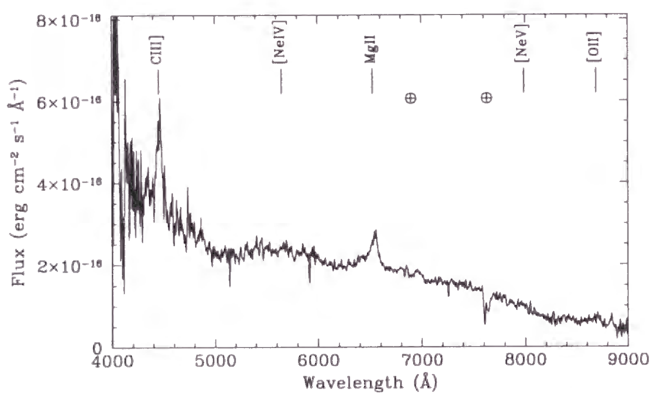

AX J131321+3119 (103)
No Filter 30 sec

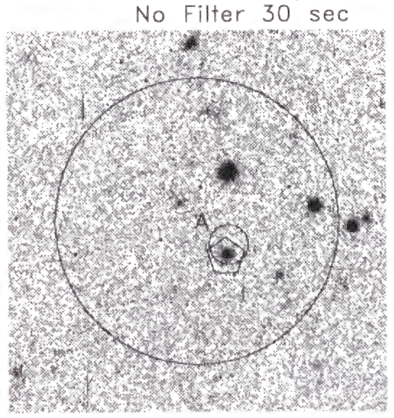

A: AGN z=0.8338

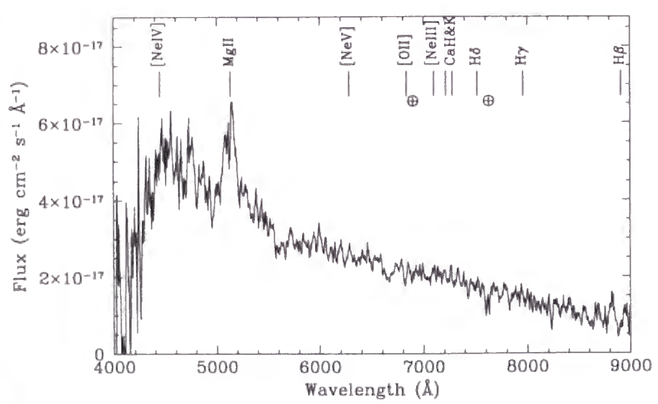

AX J131928+3251 (197)
No Filter 180 sec

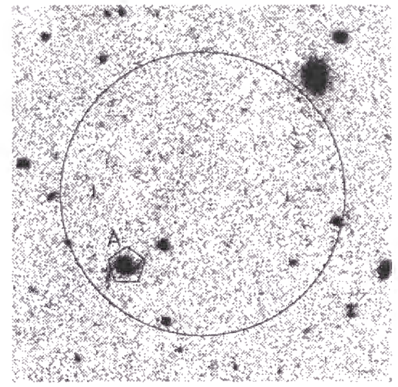

A: AGN z=0.3107

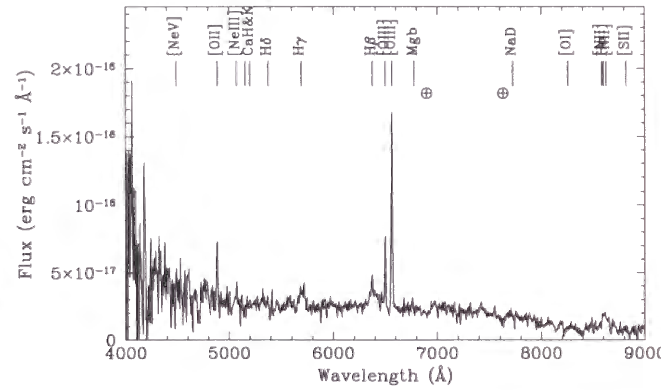

AX J131015+3004 (033)
No Filter 30 sec

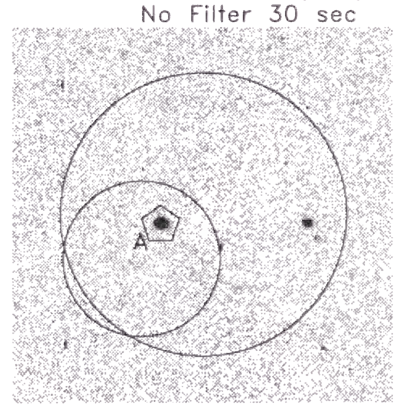

A: AGN z=1.1651

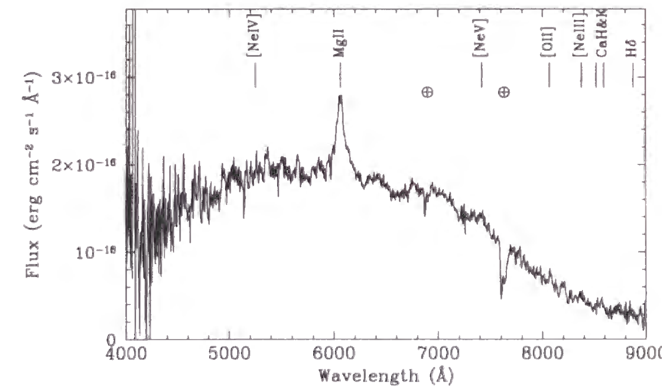

AX J130826+3005 (023)
No Filter 30 sec

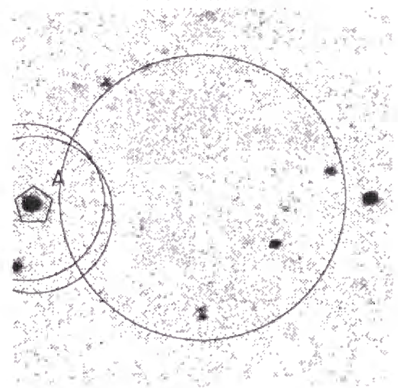

A: AGN z=0.8033

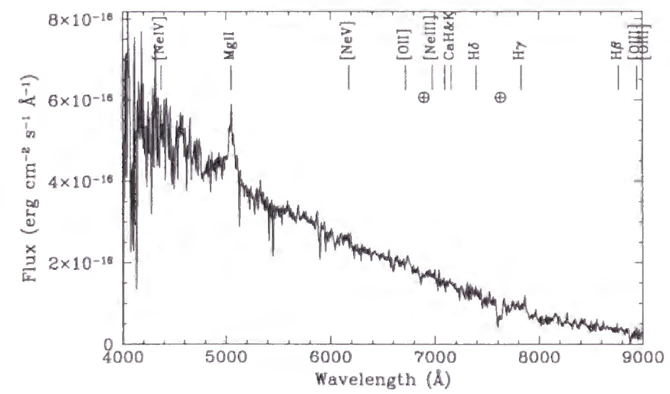

Chapter 4

Optical and X-ray Spectral Properties

In this chapter, the optical and X-ray spectral properties of the LSS AGNs are examined. First, based on the strength of the optical broad emission lines and hardness of the X-ray spectrum, we estimate the strength of absorption to the nucleus in the optical and X-ray bands, respectively. Next, we will compare the optical and X-ray absorptions.

4.1 Strength of Optical Emission Lines

To examine the strengths of broad-lines in comparison with narrow-lines, we measured the equivalent width ratios of *broad plus narrow permitted lines-to-a narrow forbidden line*. For objects at low redshifts, we measured the equivalent width ratios of Hα-to-[NII] 6583Å and Hβ-to-[OIII] 5007Å. For objects at redshifts between 0.3 and 0.75, we could measure only Hβ-to-[OIII] 5007Å ratio (we could not measure the ratio of AX J131639+3149(137), because of the fringe effect, thus the object is included in the higher redshift sample). The results are summarized in Table 3.2 and shown in Figure 4.1. The objects with strong broad Hα and Hβ lines occupy the upper-right region of the figure. Most objects at redshifts lower than 0.3 do not show significant broad component in the Hβ line and are placed in the lower part. About half of them show a broad component in the Hα line and are distributed in the lower-right region. In the right box, among objects with redshifts between 0.3 and 0.75, most of the objects show significant broad component in the Hβ line. In this redshift range, the fraction of objects with large Hβ-to-[OIII] 5007Å ratio is larger than the lower redshift sample in the left box. Based

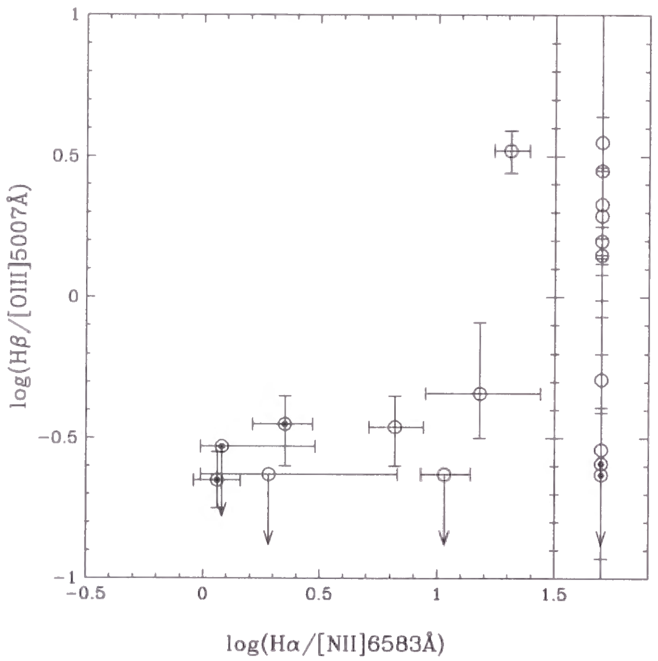

Figure 4.1: The distribution of identified AGNs in the log(Hα/[NII]6583Å) versus log(Hβ/[OIII]5007Å) diagram. Equivalent widths for Balmer lines include both broad and narrow emission lines. Objects which were not observed in the Hα region are plotted in the right box. Upper limits are indicated with downward arrows. AGNs which have a hard X-ray spectrum (an apparent photon index smaller than 1) are indicated with dots.

on the criteria used in Winkler (1992), the upper and lower boundary of the Hβ-to-[OIII] 5007Å ratio distribution in our sample correspond to type 1.2 and type 1.8 $\sim$ 2 Seyfert, respectively.

All 11 objects at redshift above 0.75 and AX J131639+3149(137) show broad MgII 2800Å or MgII 2800Å and CIII] 1909Å lines. The equivalent widths and the line widths of their MgII 2800Å lines are summarized in Table 3.2. Their equivalent widths are consistent with those of a composite spectrum of optically-selected QSOs (50 $\pm$ 29Å; Francis et al. 1991). AX J 131707+3237(175) and AX J131021+3019(039) have a narrow-emission component in the MgII 2800Å and CIII] 1909Å, respectively. Their line widths are as large as 1400 km s^{-1} in FWHM and significantly larger than line widths of typical narrow-lines. Thus, there is no high-redshift luminous cousin of a narrow-line AGN in our sample. Dependence of the strength of broad line on the luminosity is also seen in Figure 4.1.

4.2 X-ray Spectral Properties

The distribution of the apparent photon indices of the identified objects determined in the 0.7–10 keV band as a function of redshift is shown in Figure 4.2. All X-ray sources which have an apparent photon index smaller than 1 are identified with AGNs at redshifts smaller than 0.5. In the previous Figure 4.1, we mark the X-ray sources which have photon indices smaller than 1 with dots. AX J131551+3237(171), AX J131501+3141(119), AX J 131210+3048(072), and AX J130840+2955(014) were identified with AGNs which show no significant broad line in Hα and Hβ. Among them, the hardest source, AX J131501+3141(119), is identified with a type 2 Seyfert at z=0.072 (Akiyama et al. 1998a; Sakano et al. 1998). The remaining hard X-ray source (AX J130926+2952(016)) was identified with an AGN which shows a weak broad Hβ line and has a small Hβ-to-[OIII]5007Å ratio. Thus, the object corresponds to a type 1.8 Seyfert (Winkler 1992). These identification support the picture (e.g., Comastri et al. 1995) that the absorbed X-ray spectrum of narrow-line and weak-broad-line AGNs make the CXB spectrum harder than X-ray spectrum of broad-line AGN in the hard band. There still remains one hard source with a photon index of 0.58 unidentified.

Photon indices of other AGNs are distributed in the range from 1.2 to 2.1. There are three broad-line AGNs with an apparent photon index as small as 1.4 at intermediate to high redshifts. A dashed line in the figure shows the expected change of the *apparent* photon index in the 0.7–10 keV band with redshift for a type 1 Seyfert. It is derived by fitting a power-law model to the redshifted average X-ray spectrum of type 1 Seyferts (Gondek et al. 1996) in the 0.7–10 keV band. Because of the reflection component, the observed photon index of type 1 Seyfert in the 0.7–10 keV band is expected to get harder to $z \sim 2$ and to reach a minimum photon index of 1.4 at a redshift of 2.5. The photon index distribution of the broad-line AGN sample is consistent with this line. Thus, the hardness of the apparent photon indices of the three high-redshift broad-line AGNs may be explained by the existence of the reflection component. It should, however, be noted that the existence and the strength of a reflection component in AGNs with a hard X-ray luminosity of 10^{45} erg s^{-1} is not clear, so far (e.g., Nandra et al. 1997).

For the AGNs, we also fitted their X-ray spectra with an absorbed power-law model, assuming absorbing matter at the object's redshift and an intrinsic photon index of 1.7. The results are shown in column 8 of Table 3.2 and shown in Figure 4.3 and 4.4 as functions of redshifts and X-ray luminosities, respectively. The upper boundary ($\sim \log N_{\rm H}({\rm cm}^{-2}) = 23$) of the distribution of the column density is consistent with an estimated limit on the column density in the LSS sample (see Section 7.1). The lower right forbid-

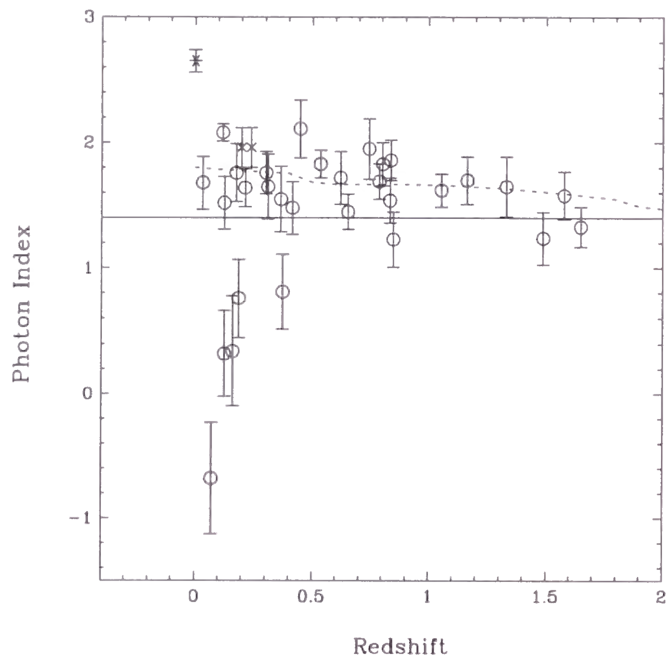

Figure 4.2: Apparent photon index (0.7–10 keV) versus redshift diagram of the identified objects. Open circles, crosses, and an asterisk represent AGNs, clusters of galaxies, and a galactic star, respectively. Horizontal solid line shows the photon index of the CXB. Expected apparent photon index for a type 1 Seyfert in the observed 0.7–10 keV band is shown with a dashed line as a function of redshifts.

den area in the diagrams is also caused by observational limit: we observe higher energy range in the rest frame for higher redshift object, therefore, the upper limit of the hydrogen column density is getting larger for higher redshift object. It should be noted that redshifts and hard X-ray luminosity correlate each other in our sample of AGNs (see Figure 7.1), thus, the two figures have similar distributions.

Hard X-ray sources which were identified with narrow-line or weak-broad-line AGNs at redshift smaller than 0.5 are fitted with column densities of $\log N_{\rm H}({\rm cm}^{-2}) = 22 \sim 23$. Most of the other AGNs are fitted with column densities less than $\log N_{\rm H}({\rm cm}^{-2}) = 22$. However, four high-redshift ($0.5 < z < 2$) luminous ($L_{2-10\ {\rm keV}} = 10^{44.5\sim45.5}$ erg s^{-1}) broad-line AGNs (AX J 131816+3240(183), AX J131054+3004(037), AX J131724+3203(152), and AX J131021+3019(039)) are fitted with large column densities. Such large neutral hydrogen column densities conflict with the existence of broad MgII lines and strong UV continua in their optical spectra. However, there is a possibility that optical extinction is not always strongly correlated with X-ray absorption (e.g., NGC4151), as in the case where the X-ray absorbing gas

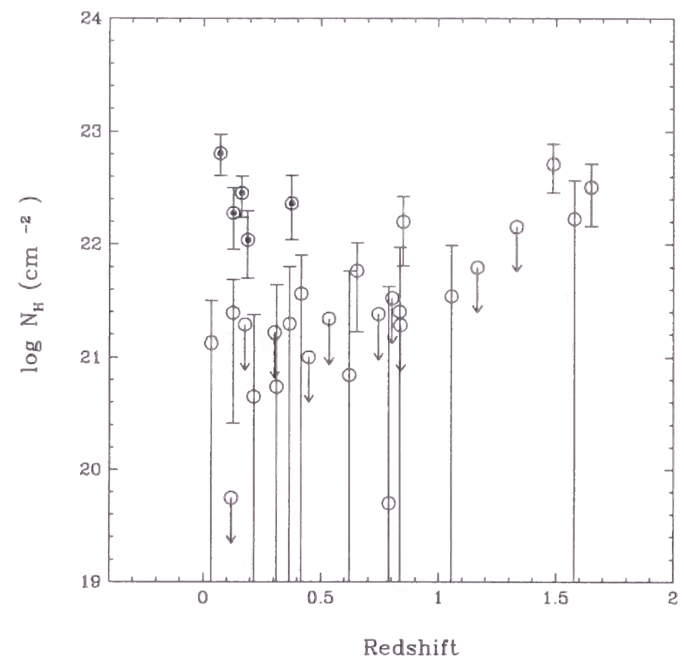

Figure 4.3: Fitted column density versus redshift diagram of the identified AGNs. AGNs with a hard X-ray spectrum which have an apparent photon index smaller than 1 are indicated with dots. Upper limits for column densities are indicated with downward arrows.

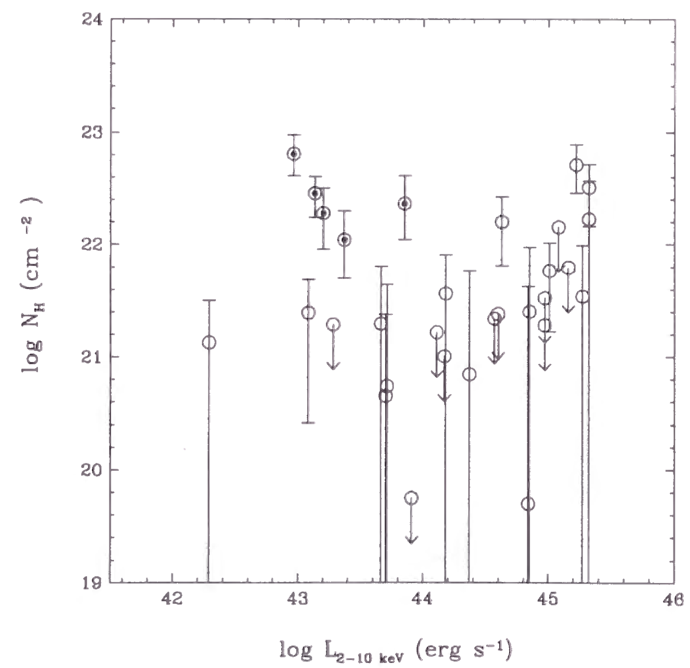

Figure 4.4: Fitted column density versus 2–10 keV luminosity diagram of the identified AGNs. The X-ray luminosities are not corrected for the absorption. AGNs with a hard X-ray spectrum which have an apparent photon index smaller than 1 are indicated with dots. Upper limits for column densities are indicated with downward arrows.

is located within the dust sublimation radius, the absorbing column density is variable, or if the gas-to-dust ratio or the composition is different from the Galactic interstellar gas. These hardness may also be explained by the effect of the reflection component. The presence of the reflection component makes observed type 1 AGN spectrum harder than a photon index of 1.7 in the 0.7–10 keV band at high-redshift, as shown in Figure 4.2. The slightly hardened X-ray spectrum in the observed band is spuriously fitted with large column density in the rest-frame band (1.8–25 keV at a redshift of 1.5) at a high redshift. Similar apparent hard X-ray spectrum (apparent photon index of 1.3 $\sim$ 1.7) of broad-line QSOs is also reported from obasevations of high-redshift ($1.2 < z < 3.4$) luminous ($L_{2-10\ \mathrm{keV}} = 10^{46} \sim 10^{48}$ erg s^{-1}) radio-loud broad-line QSOs (Cappi et al. 1997, Reeves et al. 1997) and is explained by intrinsic absorption with $\log N_{\mathrm{H}}(\mathrm{cm}^{-2}) = 22 \sim 23$. It should be noted that such hard X-ray spectrum is not observed in high-redshift ($z \sim 2$) luminous ($L_{2-10\ \mathrm{keV}} \sim 10^{46}$ erg s^{-1}) radio-quiet QSOs (Vignali et al. 1999).

4.3 Correlation between X-ray and Optical Absorption

To examine the correlation between the strength of optical broad-line and the X-ray absorption column density, we plotted the AGNs with redshift smaller than 0.75 in the Hβ-to-[OIII] 5007Å versus hydrogen column density diagram in Figure 4.5. The narrow- or weak-broad-line AGNs with $\log N_{\mathrm{H}}(\mathrm{cm}^{-2}) = 22 \sim 23$ have 10 times smaller values of Hβ/[OIII]5007Å than typical QSOs. The small ratio suggests existence of absorption with A_V of larger than 2$\sim$3 mag to the broad-line region. The optical extinction corresponds to a hydrogen column density of $\log N_{\mathrm{H}}(\mathrm{cm}^{-2}) = 21.5 \sim 21.7$, according to the relation $N_{\mathrm{H}}/A_V = 1.79 \times 10^{21}$ cm^{-2} mag^{-1}, which is determined from observations of Galactic objects (e.g., Predehl & Schmitt 1995). Thus, the optical extinction derived from the Hβ region is consistent with the X-ray spectra for these objects. One narrow-AGN and 5 weak-broad-line AGNs with log(Hβ/[OIII]5007Å) of less than 0 are fitted with smaller hydrogen column densities than $\log N_{\mathrm{H}}(\mathrm{cm}^{-2}) = 22$. In the H$\alpha$ region, however, 3/6 of them have a significant broad Hα line and are plotted with open rectangles or an open star in Figure 4.5. They fall in the lower-right region in Figure 4.1. The small hydrogen column density is consistent with the existence of a broad Hα line, which suggests smaller absorption to the broad-line region than AGNs with $\log N_{\mathrm{H}}(\mathrm{cm}^{-2}) = 22 \sim 23$. All strong-broad-line AGNs with log(Hβ/[OIII]5007Å) larger than 0 are fitted with

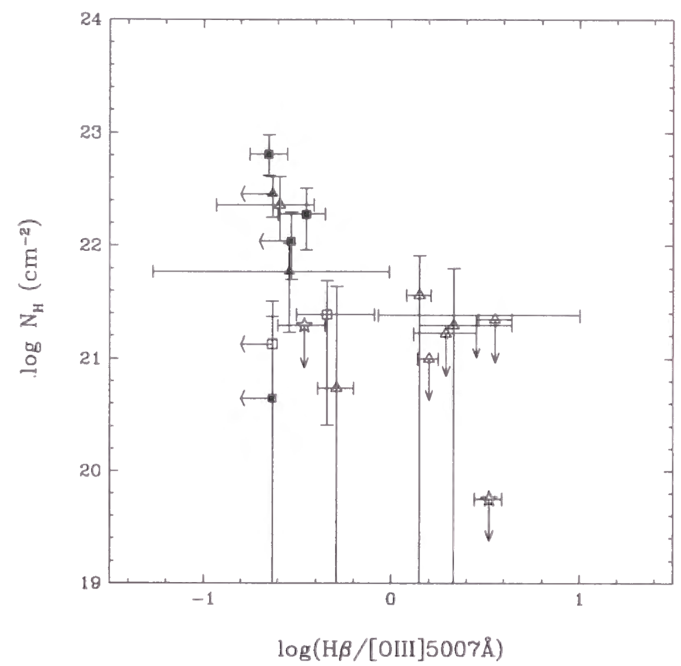

Figure 4.5: Fitted column density versus log(Hβ /[OIII] 5007Å) of the identified AGNs. The equivalent width of Hβ lines include both broad and narrow emission lines. An AGN which shows a broad Hα and a broad Hβ lines is shown with an open star, AGNs with a broad Hα and no significant broad Hβ line are plotted with open squares, and AGNs without significant broad Hα nor Hβ are indicated with filled rectangles. Note these AGNs are observed in both Hα and Hβ regions. AGNs which are observed only in the Hβ region are plotted with open triangles for objects with a broad Hβ line, and with filled triangles for objects without broad Hβ line. Upper limits are indicated with downward and leftward arrows.

hydrogen column density of less than $\log N_{\mathrm{H}}(\mathrm{cm}^{-2}) = 22$. These facts suggest the critical column density which divides the narrow-line and broad-line AGN is around $\log N_{\mathrm{H}}(\mathrm{cm}^{-2}) = 22$. The critical column density is consistent with the lower boundary of the distribution of absorbing column densities of Seyfert 2 galaxies (Risaliti, Maiolino, & Salvati 1999). We also plot the same diagram for the *HEAO1* A2 sample of AGNs. The sample follows similar correlation. In summary, for AGNs with redshift smaller than 0.75, there is no strong-broad-line AGNs (log(Hβ /[OIII] 5007Å)> 0) with large column density ($\log N_{\mathrm{H}}(\mathrm{cm}^{-2}) > 22$) in the low and intermediate redshift sample and the strengths of the broad Balmer lines are consistent with the hydrogen column density derived from the X-ray spectra. The consistency conflicts with the existence of large column densities in the high redshift luminous QSOs with strong broad emission lines. As mentioned above, one possibility is that

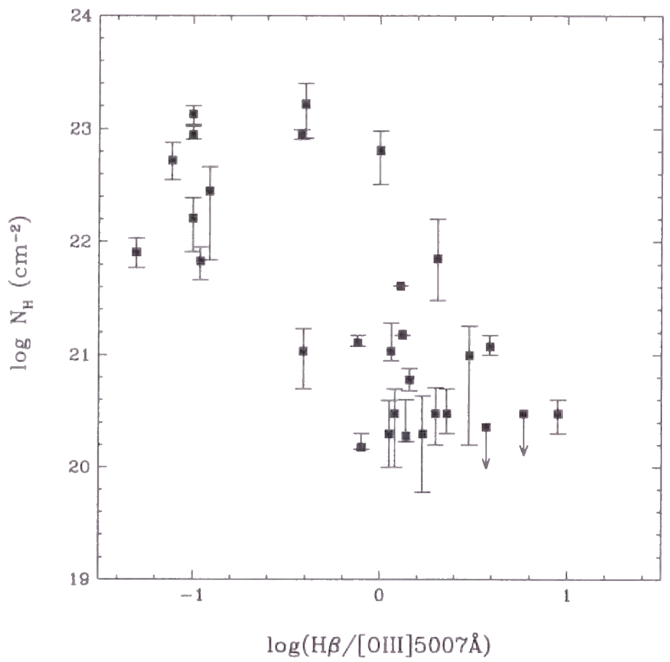

Figure 4.6: Fitted column density versus log(Hβ /[OIII] 5007Å) of the AGN sample of *HEAO1 A2* survey. The equivalent width of Hβ line include both broad and narrow emission lines. Upper limits are indicated with downward and leftward arrows. Log(Hβ /[OIII] 5007Å) ratios are from Osterbrock (1977), Whittle (1992), Winkler (1992), Tadhunter et al. (1993), de Grijp et al. (1992), Phillips et al. (1979), and Vaceli et al. (1997). Hydrogen colum densities are from Schartel et al. (1997).

the hardness of the high redshift luminous QSOs is not caused by absorption but by intrinsically hard X-ray spectrum of QSOs in the high energy band, such as reflection component. The other possibility is that dusts in the X-ray absorbing matter evaporate in the luminous QSOs. To distinguish the effect of a real X-ray absorption and the intrinsically hard spectrum, such as reflection component, X-ray spectroscopic observations for such broad-line AGNs below 0.7 keV in the observed frame are critical.

Chapter 5

Spectral Energy Distributions

We discuss spectral energy distributions (SEDs) of LSS AGNs, based on the correlation between radio, optical, and X-ray luminosities and optical colors.

5.1 Optical Photometric Properties

We have examined the optical appearance of each identified object. The results are indicated in the last column of the Table 3.2. All of the low-luminosity AGNs show their host galaxy component in the optical light. We calculate optical total absolute magnitudes of the identified objects, using $\alpha = -0.5$, which corresponds to $V - R$ of 0.22 mag. The results are shown in Table 3.2 and plotted in Figure 5.1 as a function of X-ray luminosity. For high-luminosity AGNs, hard X-ray luminosities correlate with optical luminosities. On the other hand, for the low-luminosity AGNs whose optical light is affected and maybe dominated by their host galaxy components, the correlation is broken. Considering the break, we estimate the absolute magnitudes of the host galaxies to be around $M_V = -21 \sim -23.5$ mag and are similar to that of QSO host galaxies (Bahcall et al. 1997). Excluding objects which show host galaxy components in optical images, we plot the same figure for the remaining stellar objects (Figure 5.2) Several radio-quiet QSOs observed with *ASCA* (Reeves et al. 1997) are also plotted in the same diagram. The LSS AGNs and the QSOs follow the same sequence on the diagram. The sequence suggests that the LSS AGNs have similar optical-to-X-ray luminosity ratio to normal QSOs (see also Figure 3.2) and no excess extinction in the optical wavelength.

The optical colors of luminous broad-line AGNs with stellar optical images distribute from $B - R$ of -0.2 mag to 1.1 mag (Figure 5.3). The color

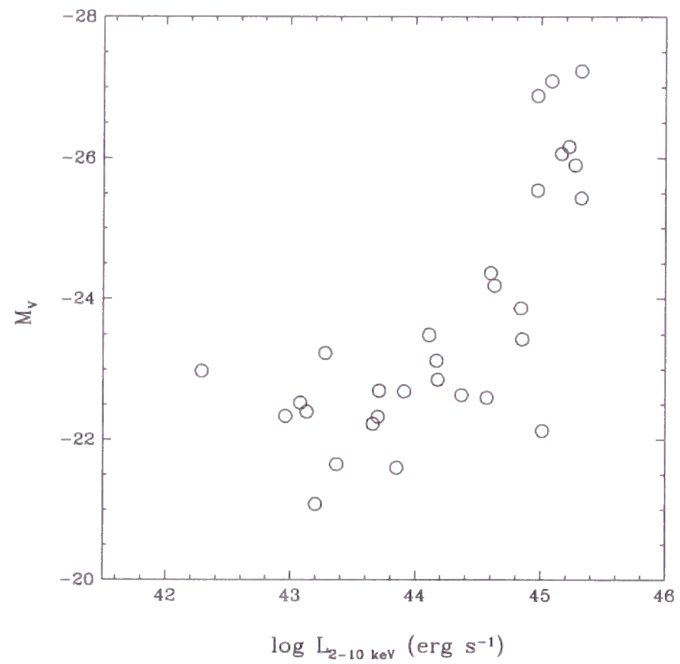

Figure 5.1: Hard X-ray luminosity versus optical V band absolute magnitude diagram of the identified AGNs.

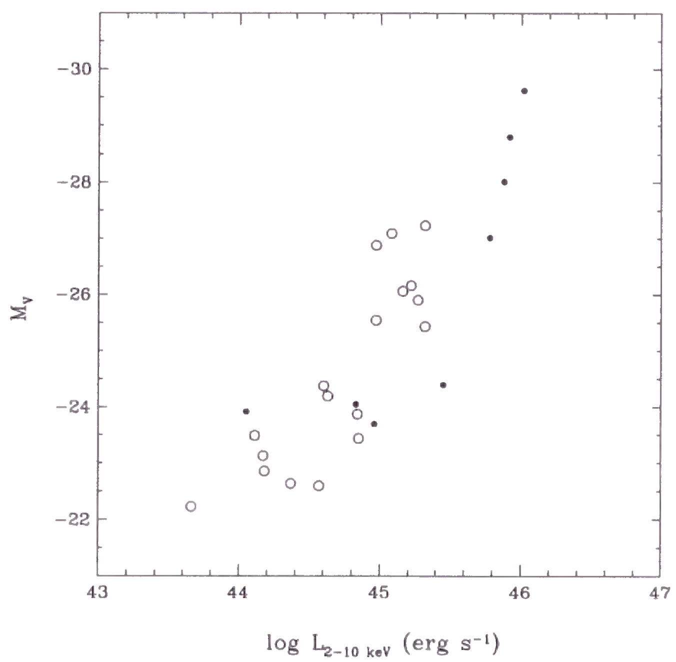

Figure 5.2: Hard X-ray luminosity versus optical V band absolute magnitude diagram of the identified AGNs with stellar image. Radio-quiet QSOs observed with *ASCA* (Reeves et al. 1997) are plotted with small dots.

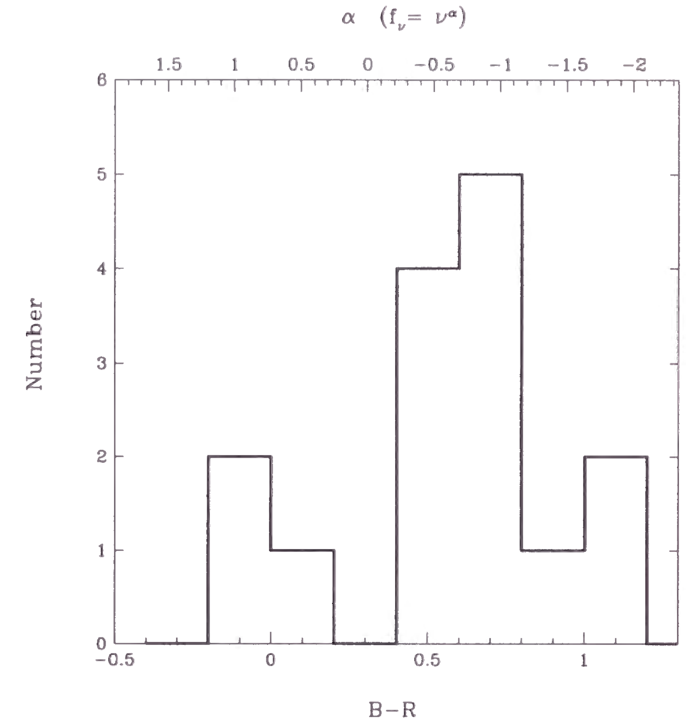

Figure 5.3: Optical $B-R$ color distribution of the identified AGNs with stellar image. The upper horizontal axis indicates the corresponding energy index of the color, if we assume a pure power-law spectrum.

range corresponds to the energy index range of $\alpha = -2.1 \sim 1.3$, if we assume the power-law spectrum. The distribution is roughly consistent with that of optically selected QSOs ($\alpha = -1.5 \sim 1$, Francis et al. 1991), however, slightly extends to blue region in comparison with radio selected QSOs ($\alpha = -2 \sim 0$, Richstone & Schmidt 1980, Francis et al. 1999). There is no broad-line QSO which has a $B-R$ color larger than 2.0 mag, which is a criterion for *red* QSOs in Kim & Elvis (1999). Two low-luminosity broad-line AGNs (AX J131725+3300(192) with $B-R = 2.3$ mag and AX J131407+3158(127) with $B-R = 1.5$ mag) which show a broad Hα emission have red optical colors. Their X-ray spectra and large Balmer decrements suggest the extinction of $\log N_{\rm H}({\rm cm}^{-2}) = 21.3$ which corresponds to $A_V = 1$ mag to their nucleus (see Section 4.3, Figure 4.1 and 4.5). Considering that $E(B-R)$ corresponds to 0.6 A_V, the red colors may be originate from their absorbed nuclei. However, the colors are also probably affected by the host galaxy, because their optical images show the host galaxy components.

Absorbed AGNs have redder $B-R$ colors than non-absorbed AGNs in the

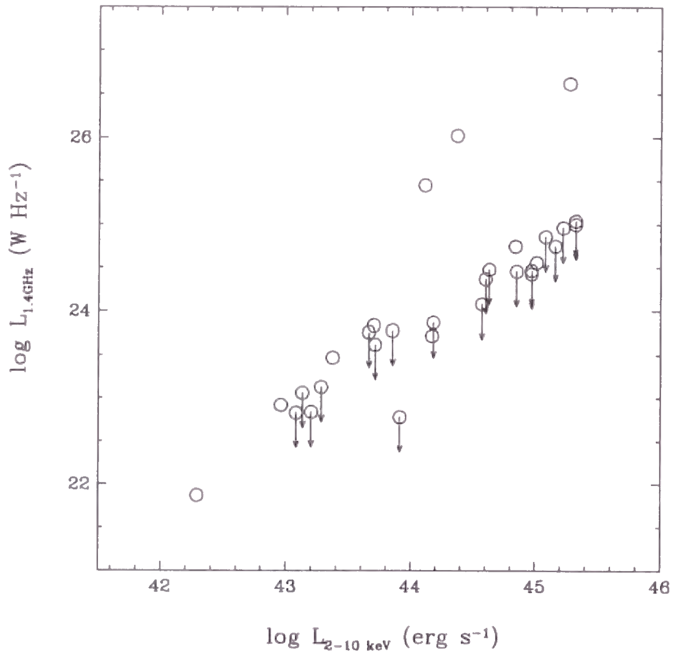

Figure 5.4: Hard X-ray luminosity versus radio 1.4 GHz luminosity diagram of the identified AGNs. Downward arrows show upper limit on the radio luminosities.

ASCA Large Sky Survey sample. Red colors of host galaxies of the absorbed AGNs or absorbed nuclear light are thought to be the origin of the redness of the optical colors. We discuss optical colors of absorbed AGNs in Chapter 8.

5.2 Radio and Far-infrared Properties

To examine radio properties of the identified AGNs, we show a radio versus hard X-ray luminosity diagram in Figure 5.4. There are two sequences in the diagram; three objects which have large radio-to-hard X-ray luminosity ratios correspond to radio-loud AGNs and others which have smaller ratios correspond to radio-quiet AGNs. The radio-to-hard X-ray ratios of the radio-loud sequence are consistent with the average SED of radio-loud QSO (Elvis et al. 1994). On the other hand, the radio-quiet sequence has one order of magnitude larger radio-to-hard X-ray luminosity ratio than the average SED of radio-quiet QSO (Elvis et al. 1994). Based on the dispersion of the radio-to-optical luminosity ratios of radio-quiet QSOs (Visnovsky et al. 1992), the large radio-to-hard X-ray luminosity ratio is accounted by a scatter and a selection bias for radio louder objects. The fraction (3/30) of radio-loud

AGNs in the total AGN sample is consistent with that in the low-luminosity sample of optically selected QSOs (13%) (Visnovsky et al. 1992). In radio images, all radio-quiet AGNs show only one point-like component. Two radio-loud AGNs consist of two components; one dominates the total flux located on the optical position and the other fainter source is $\sim$ 15 arcsec away from the central component.

In the LSS sample, only the galactic star is detected in the *IRAS* survey (Moshir et al. 1992). None of the AGN is detected in the *IRAS* Faint Source Survey. Based on the flux limit of the *IRAS* survey in the LSS region (0.1 Jy in 60 μm), most of the AGNs have lower limits to the logarithmic ratio of 2–10 keV luminosity-to-far-infrared luminosity ($\nu_{60\mu m} L\nu_{60\mu m}$) of less than -1, consistent with those known for QSOs (-1) and only one object (AX J131822+3347 (235)) has a lower limit (-0.6) to the logarithmic ratio larger than the typical value of QSOs. The lower limits to the logarithmic ratio are significantly larger than those of star-forming galaxies, which have logarithmic ratios around -4.

Chapter 6

Number Counts

This chapter estimate contribution to the CXB from each population using the logN-logS relations, that is, relation between a flux limit (S) and surface number density of sources (N) above the flux limit. The LSS AGN sample is divided into two populations: absorbed and less-absorbed AGN, based on hydrogen column densities derived from X-ray spectra. We also compare the logN-logS relation with soft X-ray logN-logS relation determined from *ROSAT* surveys.

6.1 LogN-logS Relation of Each Population

We hereafter divide the AGN sample at the intrinsic column density of $\log N_{\rm H}({\rm cm}^{-2}) = 22$: we refer the AGNs with the column density larger and smaller than $\log N_{\rm H}({\rm cm}^{-2}) = 22$ as "the absorbed AGN" and "the less-absorbed AGN", respectively. At first, we include the four high-redshift broad-line AGNs fitted with the large column densities in the less-absorbed sample, because such large column densities could be only apparent (Section 4.2 and 4.3).

Figure 6.1 shows the cumulated logN-logS relations for the absorbed and for the less-absorbed samples in the SIS 3.5σ sample. Since the sensitivity limit is given in count rates, the actual flux limit depends on X-ray spectrum of sources. For an X-ray spectrum with the canonical photon index of type 1 AGNs ($\Gamma = 1.7$), the deepest source-detection limit of the SIS 3.5σ sample (1.2 cts ksec^{-1}; see Table 2.1) is equivalent for 1.1×10^{-13} erg cm^{-2} s^{-1} in the 2–10 keV band. If we assume an object with hydrogen column density of $\log N_{\rm H}({\rm cm}^{-2}) = 23$ at redshift of 0.1, which corresponds to the hardest object in the LSS sample, the flux limit is estimated to be 1.6×10^{-13} erg cm^{-2} s^{-1} in

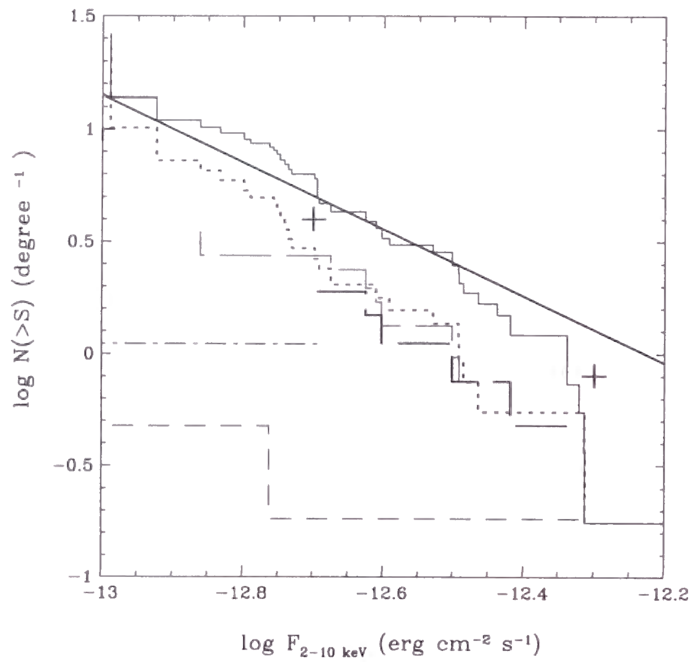

Figure 6.1: Cumulative logN-logS relations in the 2–10 keV band for the SIS 2–7 keV 3.5σ sample. The thin solid line, the thick dotted line, the thick long-dashed line, and the thin long-dashed line correspond to the logN-logS relations for all sources, the less-absorbed ($\log N_{\rm H}({\rm cm}^{-2}) < 22$) AGNs, the absorbed ($\log N_{\rm H}({\rm cm}^{-2}) > 22$ without the 4 hard broad-line AGNs) AGNs, and the absorbed ($\log N_{\rm H}({\rm cm}^{-2}) > 22$ with the 4 hard broad-line AGNs) AGNs, respectively. The short dashed line indicates the logN-logS relations of clusters of galaxies, and the dot dashed line shows that of an unidentified source. The thick solid line represents extrapolation with a slope of -1.5 from the *HEAO1* A2 results. The plus signs represent 2–10 keV logN-logS relation from *ASCA* Medium Sensitivity Survey (Ueda et al. 2000) Survey limits for less-absorbed AGNs and clusters of galaxies are 1×10^{-13} erg cm^{-2} s^{-1} , whereas it is 1.6×10^{-13} erg cm^{-2} s^{-1} for absorbed AGNs with the hardest X-ray spectrum.

	log N(>S)[b]		α[c]	Contributions[d]
	HEAO1 A2	*ASCA* LSS		
Flux limit[a]	3×10^{-11}	2×10^{-13}		2×10^{-13}
Total	-2.62	$0.80^{+0.07}_{-0.08}$	$1.55^{+0.03}_{-0.05}$	16%
Less-absorbed AGN	-2.66	$0.47^{+0.08}_{-0.10}$	$1.42^{+0.04}_{-0.05}$	9%
Absorbed AGN (without 4 broad-line AGN)	-3.68	$0.28^{+0.16}_{-0.25}$	$1.80^{+0.07}_{-0.11}$	4%
Absorbed AGN (with 4 broad-line AGN)	-3.68	$0.44^{+0.13}_{-0.19}$	$1.89^{+0.06}_{-0.09}$	6%
Cluster	-2.98	$-0.74^{+0.23}_{-0.52}$	$1.02^{+0.11}_{-0.24}$	1%

Table 6.1: LogN-logS relations of various populations and their contributions to the CXB in the 2–10 keV band.

Notes:
a: Flux limit in unit of erg cm^{-2} s^{-1} in the 2–10 keV band.
b: Source number densities at the flux limits in degree^{-2}. The errors of the LSS source number densities are estimated with the square root of the detected number.
c: Slopes of logN-logS relations in the flux range.
d: Contributions to the CXB from the sources in the flux range from 3×10^{-11} erg cm^{-2} s^{-1} to the flux limits.

the 2–10 keV band. In the calculation of Figure 6.1, the SIS count rate was converted into the flux with the best-fit photon index determined in the 0.7–10 keV band for each source to take into account this effect. As noted from Figure 6.1, the surface number density of the absorbed AGNs is comparable to that of the less absorbed AGNs at flux larger than 2×10^{-13} erg cm^{-2} s^{-1} . The large fraction of the less-absorbed AGNs in the identified sample is due to different limiting flux for different X-ray spectra.

At the first step, we estimate the contributions to the CXB, integrating the logN-logS relations from the brightest to the faintest object in each population of the LSS sample. For less-absorbed AGNs, absorbed AGNs, and clusters of galaxies, the summed fluxes of sources per unit area are 3.3×10^{-12} erg cm^{-2} s^{-1} degree^{-2}, 6.3×10^{-13} erg cm^{-2} s^{-1} degree^{-2}, and 1.4×10^{-13} erg cm^{-2} s^{-1} degree^{-2} and contributions to the CXB are 17%, 3%, and 0.7% , respectively, if we use the CXB flux determined in the LSS field (Ishisaki et al. 1999, 2.0×10^{-11} erg cm^{-2} s^{-1} degree^{-2} in the 2–10 keV band).

As the second step, to determine contributions of each population in a wider flux range, we combined results of the *HEAO1* A2 sample (Piccinotti et al. 1982). The sample consists of 30 AGNs, 4 BL Lac objects, 30 clusters of galaxies, 1 starburst galaxy, and 3 unidentified sources with the flux limit of 3.1×10^{-11} erg cm^{-2} s^{-1} in the 2–10 keV band. In the 30 AGNs, 6 AGNs are fitted with hydrogen column density larger than $\log N_{\rm H}({\rm cm}^{-2}) = 22$ (Schartel et al. 1997). The source number density at the flux limit is 2.4×10^{-3} degree^{-2}. If we assume that there is no break in the logN-logS relations, the slopes of the relations between the *HEAO1* A2 and the LSS limits can be determined. The results are shown in Table 6.1. In this flux range, the total number count in the 2–10 keV band has a slope (α of $N(>S) = kS^{-\alpha}$) of 1.5 and is consistent with that of smoothly distributed sources in a simple Euclidean geometry as reported in Ueda et al. (1998). However, the slope is a summation of steep slopes for AGNs and a shallow slope for clusters of galaxies. Thus the Euclidean distribution is an apparent effect. The slope of the logN-logS relation of clusters of galaxies in the flux range is consistent with that determined in the 0.5–2 keV band (1.15, Vikhlinin et al. 1998). Based on the slope of the logN-logS relation, the contributions from less-absorbed AGNs, absorbed AGNs, and clusters of galaxies are estimated to be 9%, 4%, and 1%, respectively, integrating the logN-logS relations from 3×10^{-11} erg cm^{-2} s^{-1} down to the flux limit of 2×10^{-13} erg cm^{-2} s^{-1} , which is the limit for absorbed AGNs and at which 16% of the CXB was resolved into discrete sources. The logN-logS relation of the absorbed AGNs with the four high-redshift broad-line AGNs is also shown in Figure 6.1 with a thin long-dashed line. Based on the logN-logS relation, the contribution of the absorbed AGNs with the four AGNs to the CXB is estimated to be 6%.

6.2 Comparison with a Soft X-ray LogN-logS Relation

We compared the logN-logS relation of the LSS AGN populations with the logN-logS relation of AGNs determined in 0.5–2 keV band by *ROSAT* surveys (Miyaji et al. 2000). The soft X-ray logN-logS relation is dominated by broad-line AGNs, though it includes narrow-emission line galaxies. We plotted the soft X-ray logN-logS relation on the hard X-ray logN-logS relations assuming photon index of 1.9, 1.7, 1.5, and 1.3 in Figure 6.2. The 2–10 keV

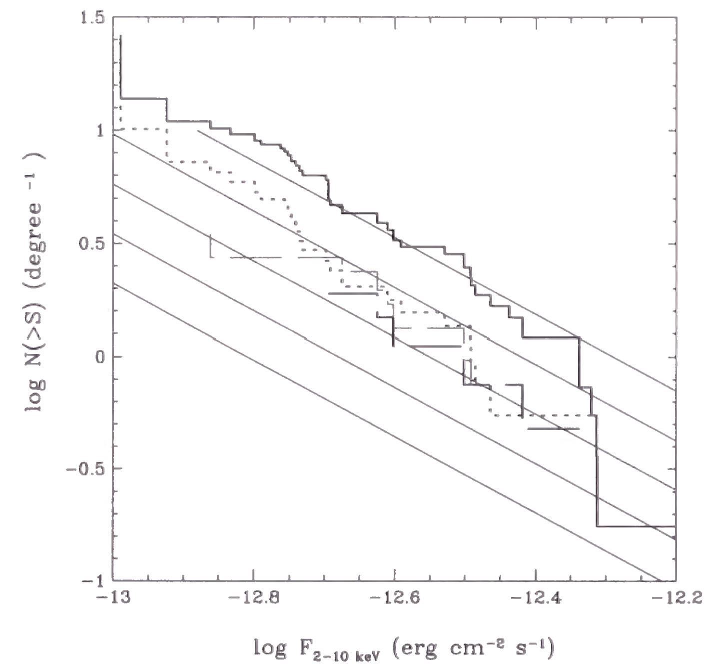

Figure 6.2: LSS AGN logN-logS relations compared with AGN logN-logS relation in the 0.5–2 keV band derived by *ROSAT* surveys. The thin solid line, the thick dotted line, the thick long-dashed line, and the thin long-dashed line correspond to the logN-logS relations for all sources, the less-absorbed ($\log N_{\rm H}({\rm cm}^{-2}) < 22$) AGNs, the absorbed ($\log N_{\rm H}({\rm cm}^{-2}) > 22$ without the 4 hard broad-line AGNs) AGNs, and the absorbed ($\log N_{\rm H}({\rm cm}^{-2}) > 22$ with the 4 hard broad-line AGNs) AGNs, respectively. Thin solid straight lines indicate 0.5–2 keV logN-logS relation. The 0.5–2 keV logN-logS relations converted to 2–10 keV logN-logS relation assuming photon index of 1.9, 1.7, 1.5, and 1.3 from bottom to top.

logN-logS relation of all sources is consistent with the 0.5–2 keV logN-logS relation with photon index of 1.3 as reported in Ueda et al. (1999a). The logN-logS relation of broad-line AGNs in the 2–10 keV band shows excess in comparison with that in the 0.5–2 keV band. If we use the typical photon index of broad-line AGNs ($\Gamma = 1.7$ in the 2–10 keV band, $\Gamma = 2.0$ in the 0.5–2 keV band) to convert the soft X-ray flux to the hard X-ray flux, the converted 0.5–2 keV logN-logS relations have at least two times smaller normalization than the 2–10 keV logN-logS relation of broad-line AGN of the LSS sample. The 2–10 keV logN-logS relation is roughly consistent with the soft X-ray logN-logS relation of AGNs converted with photon index of 1.5. The results support the suggestion that broad-line QSOs have harder X-ray spectra than photon index of 1.7, which is typical value of nearby QSOs, as mentioned in Section 4.2.

Chapter 7

Redshift Distribution

This chapter discuss the fraction of absorbed AGNs as a function of luminosity and redshift. As mentioned in Section 4.1, there is no narrow-line or weak-broad-line AGN at high redshift in the LSS sample. The LSS AGN sample is divided into absorbed and less-absorbed AGNs the same as in Chapter 6 and compare the redshift distribution of the two populations.

7.1 Redshift - luminosity Relation

We plot the X-ray luminosity versus redshift diagram of all the identified AGNs of the SIS 3.5σ sample in Figure 7.1a. Absorbed AGNs are marked with dots. At first, the high-redshift broad-line AGNs which are fitted with large column densities are included in the less-absorbed sample as in Chapter 6. The number ratio of absorbed AGNs-to-less-absorbed AGNs is clearly changing with redshift, luminosity, or both. If we limit the sample above the flux level of 2×10^{-13} erg cm^{-2} s^{-1} , which is the flux limit for the absorbed AGNs, the redshift and luminosity distribution of the limited sample is also significantly different between these two populations. The number count of the absorbed AGNs is dominated by nearby low-luminous objects, in contrast to that of less-absorbed AGNs, which are dominated by QSOs at intermediate to high redshifts. In the same figure, the AGN sample from the *HEAO1* A2 survey (Piccinotti et al. 1982) is also plotted with small marks. Objects with hydrogen column density larger than $\log N_{\rm H}({\rm cm}^{-2}) = 22$ are also marked with small dots (Schartel et al. 1997). The same tendency of deficiency of absorbed AGNs with a large luminosity is seen in their sample. Such a deficiency of luminous absorbed AGNs is also found in the *ROSAT*, *ASCA*, and *Beppo-SAX* deep surveys in the Lockman Hole (Hasinger et al. 1999).

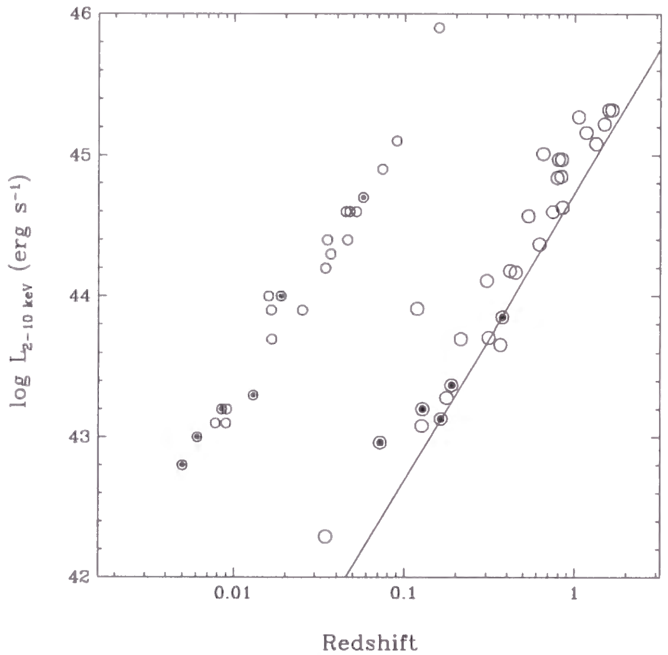

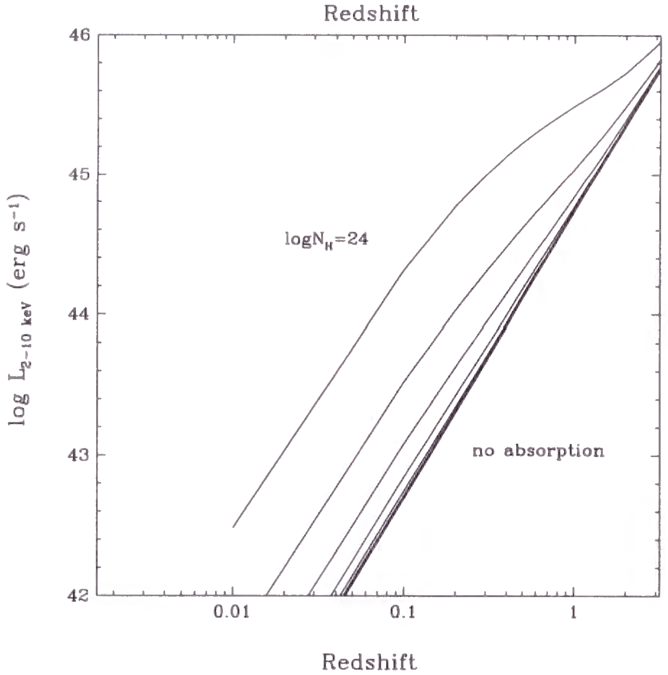

Figure 7.1: a) 2–10 keV luminosity versus redshift diagram of the identified sample. The LSS AGNs are plotted with large open circles. Absorbed ($\log N_{\rm H}({\rm cm}^{-2}) > 22$) AGNs are marked with dots. The solid line is the detection limit of the SIS 2–7 keV 3.5σ sample for non-absorbed AGN. We also plot the *HEAO1* A2 sample of AGNs (Piccinotti et al. 1982) with small marks. b) Detection limit of the SIS 2–7 keV 3.5σ sample to an *intrinsic* 2–10 keV luminosity as a function of redshift. From top to bottom, column densities of $\log N_{\rm H}({\rm cm}^{-2}) = 24.0, 23.5, 23.0, 22.5, 22.0, 21.5, 21.0$, and no absorption with an intrinsic photon index of 1.7 are assumed. The survey limit of the SIS 3.5σ sample is 1.2 cts ksec^{-1} in the 2–7 keV band.

In Figure 7.1b, detection limits of the SIS 2–7 keV 3.5σ sample for intrinsic luminosities with various absorption column densities is shown as a function of redshift. In this calculation, we assume the intrinsic photon index of 1.7 and consider the response function of *ASCA* with the SIS. The difference between the survey limits of non-absorbed objects and that of objects with $\log N_{\rm H}({\rm cm}^{-2}) = 22.5$ is less than 0.2 in the logarithmic-scale intrinsic luminosity at the redshift range from 0 to 1.5. Thus, we can detect objects with intrinsic column densities of up to $\log N_{\rm H}({\rm cm}^{-2}) = 22.5$ at redshifts smaller than 1.5 in an unbiased fashion. At higher redshifts objects with column densities of up to $\log N_{\rm H}({\rm cm}^{-2}) = 23$ are detected without bias, thanks to the redshift effect. It should be noted that the peak of the distribution of absorption column densities of type 2 Seyferts in the nearby universe ($\log N_{\rm H}({\rm cm}^{-2}) > 23$; Risaliti et al. 1999) is beyond the detection limit.

7.2 Redshift Distribution

To examine the deficiency of luminous absorbed AGNs more quantitatively, we compare the redshift distribution of absorbed AGNs and that of less-absorbed AGNs, considering the difference of their X-ray spectra. In Figure 7.2a, we show the redshift distribution of less-absorbed AGNs as well as the expected redshift distribution of broad-line AGNs. The four high-redshift broad-line AGNs which are fitted with large column densities are included in the less-absorbed sample. The expected redshift distribution of broad-line AGNs is calculated based on a hard-band X-ray luminosity function of broad-line AGNs and its evolution (Boyle et al. 1998a); they are determined by an AGN sample from *ASCA* observations of Deep *ROSAT* fields and optical identifications of the Large Area Sky Survey/Modulation Collimator catalog obtained from *HEAO1* mission. The expected redshift distribution matches well to that of the LSS sample. Based on Kolmogorov-Smirnov test, the probability that the observed redshift distribution agrees with the model is calculated to be 64%. Thus, we use the hard-band X-ray luminosity function as a base model for less-absorbed AGNs. In Figure 7.2b, we compare the redshift distribution of absorbed AGNs in the LSS sample with the expected distribution of them calculated by assuming that the shape of the intrinsic (which means absorption corrected) luminosity function of absorbed AGNs is the same as that of less-absorbed AGNs. The equal number density of AGNs with $\log N_{\rm H}({\rm cm}^{-2}) = 22 \sim 23$ to that of less-absorbed AGN is the same as in the spectrum model of the CXB; e.g., Comastri et al. (1995) used the value of 1.23 for the number ratio of AGNs with absorption of $\log N_{\rm H}({\rm cm}^{-2}) = 22 \sim 23$ to those with absorption less than $\log N_{\rm H}({\rm cm}^{-2}) =$

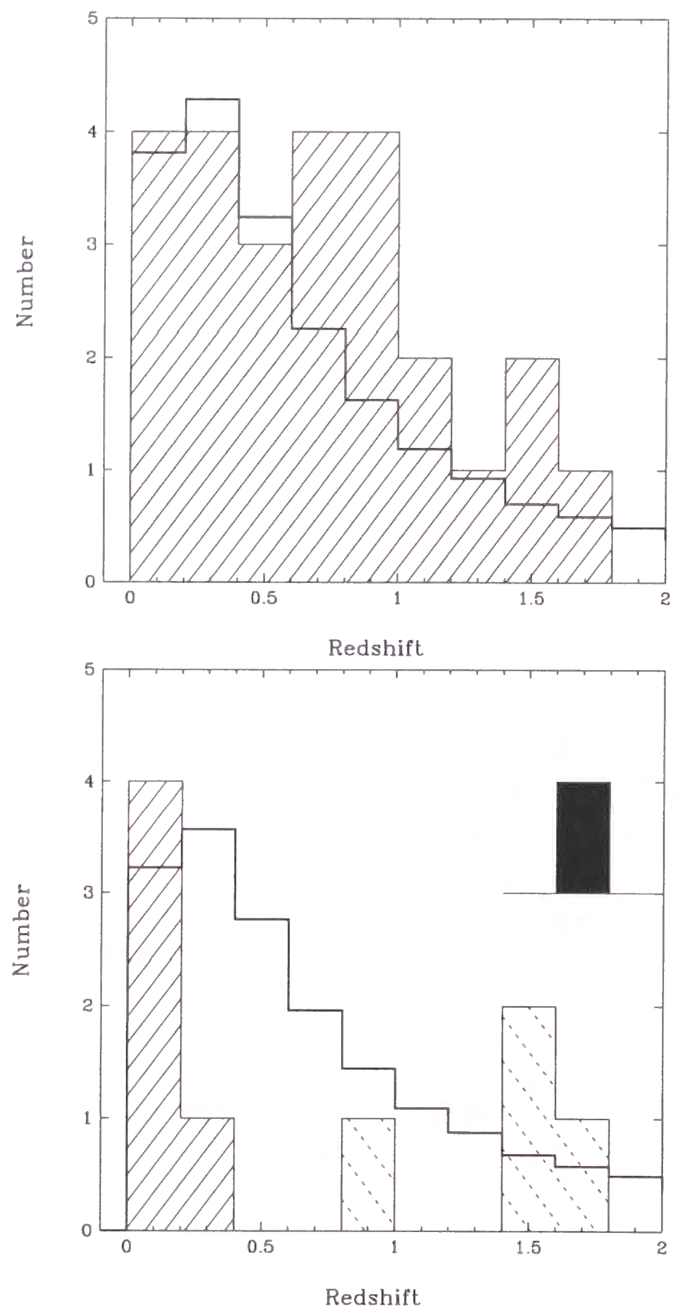

Figure 7.2: a) Comparison of redshift distribution of the less-absorbed ($\log N_{\rm H}({\rm cm}^{-2}) < 22$) AGNs in the LSS sample with that expected from a broad-line AGN luminosity function in the hard X-ray band. The shaded histogram is the redshift distribution of the LSS AGN sample and the solid line is the expected redshift distribution. The four high redshift broad line AGNs with a hard X-ray spectrum are included in this histogram. See Section 6. b) Comparison of redshift distribution of the absorbed ($\log N_{\rm H}({\rm cm}^{-2}) > 22$) AGNs in the LSS sample with that expected from a broad-line AGN luminosity function in the hard X-ray band with an absorption of $\log N_{\rm H}({\rm cm}^{-2}) = 22.5$. The shaded histogram is the redshift distribution of the absorbed AGNs and the histogram shaded with dashed lines is that of the broad-line AGNs with a hard X-ray spectrum mentioned above. The solid line is the expected redshift distribution. The black histogram at the right-top corner refers to unidentified source.

22. As seen in Figure 7.2b, at redshift smaller than 0.4, in which the X-ray luminosity of the sample AGN is less than 10^{44} erg s^{-1}, the number of absorbed AGNs is comparable to the expectation. However, at redshifts larger than 0.4, the total expected number is about 10, which contrasts to the non-detection. The observed redshift distribution is different from the model redshift distribution; Kolmogorov-Smirnov test gives a probability of only 5% for the null hypothesis that the redshift distribution of absorbed AGNs is the same as the model, thus the hypothesis is rejected. Therefore, our sample suggests the deficiency of the absorbed AGNs with the column density of $\log N_{\rm H}({\rm cm}^{-2}) = 22 \sim 23$, in the redshift range between 0.5 and 2.0, or in the X-ray luminosity range larger than 10^{44} erg s^{-1}, or both. We plot the redshift distribution of the four high-redshift broad-line AGNs with hard X-ray spectra in Figure 7.2b with a histogram shaded with dashed lines. By including the four AGNs, the observed redshift distribution agrees the model redshift distribution with probability of 60%. If their large column densities are real, they could complement the deficiency of absorbed high-redshift luminous AGNs.

Chapter 8

Host Galaxies

We discuss optical morphological and photometric properties of absorbed and/or narrow-line AGNs in the LSS sample. Their optical lights are dominated by host galaxies as suggested in Section 5.1. We also discuss optical properties of high-redshift absorbed AGNs found in other surveys. It is worth noting that the X-ray luminosities of these objects correlate with their redshifts because of a selection limitation: low redshift objects have Seyfert luminosities and high redshift objects have QSO luminosities.

8.1 Optical Imaging Observations

8.1.1 Photometric Observations

We made optical photometric observations for 6 absorbed and/or narrow-line AGNs in the *ASCA* LSS sample and absorbed narrow-line QSOs found in the *ASCA* Lynx Deep Survey (AX J08494+4454) and the *ROSAT* Medium Sensitivity Survey (RX J1011.2+5545) (for the 2 additional objects, see Table 1.1). Except for RX J1011.2+5545, all objects are radio-quiet (Section 5.2), though 5 of them are detected in radio surveys (AX J131501 +3141(119), AX J131210+3048(072), AX J131758+3257(195), AX J131831 +3341(228), and AX J08494+4454).

Optical photometric observations were made with the Tektronix 2048 $\times$ 2048 CCD at the University of Hawaii (UH) 88″ telescope on April 20, 21, 1996 and March 5, 6, 1999. Images were obtained with Mould B, V, R, and I band filters, respectively. Exposure times in each objects are summarized in Table 8.1. For photometric calibrations, 50 Landolt's standard stars (Landolt 1992) were observed. The seeing size was $\sim 0.''8$ and the pixel scale

Name	Period	Exposure time (s)			
		B	V	R	I
AX J131501+3141(119)	Apr. 96	1200	···	900	···
AX J131551+3237(171)	Apr. 96	1200	···	900	···
AX J131210+3048(072)	Mar. 99	600	420	900	300
AX J131758+3257(195)	Mar. 99	300	300	600	300
AX J130926+2952(016)	Mar. 99	600	420	1800	420
AX J131831+3341(228)	Mar. 99	600	450	1500	300
AX J08494+4454	Mar. 99	1200	1200	1200	1200
RX J1011.2+5545	Mar. 99	900	1200	600	300

Table 8.1: Journal of Photometric Observations.

was 0.″2194 pixel^{-1}.

The data were analyzed using IRAF. Bias subtraction and flat-fielding with dome flats were done. Based on scatters of countrate-to-magnitude conversion factors of the observed 50 Landolt's standard stars, uncertainties of the photometric calibrations were estimated to be 0.03, 0.06, 0.03, and 0.06 mag in B, V, R, and I bands, respectively. The uncertainties include errors of flat fielding.

8.1.2 Deep Imaging Observations for AX J131831 +3341(228)

AX J131831+3341(228) is the most luminous absorbed AGN in the LSS AGN sample. For the object, we have done deep optical imaging observations with the Suprime-Cam attached to the Cassegrain focus of the 8.2m Subaru telescope on May 13, June 11, and June 12, 1999 during the first-light phase of the telescope. The pixel scale of the camera was 0.″03 pixel^{-1}. The camera consists of 6 4096 × 2048 CCD chips. For the observation, a SITe 4096 × 2048 chip was used. The seeing condition during the observation was not so good (FWHM is ∼ 0.″7). Three 600 s exposures in R band and two 900 s exposures in V band were obtained. Unfortunately, the object falls at the edge of the CCD in one frame in each band, therefore the northern part of the image in R band and the southern part of the image in V band are covered with shorter effective exposure time than the other region. Photometric calibrations of the V and R band images were made with stars in the frames whose magnitudes were already calibrated in the previous UH photometric observations.

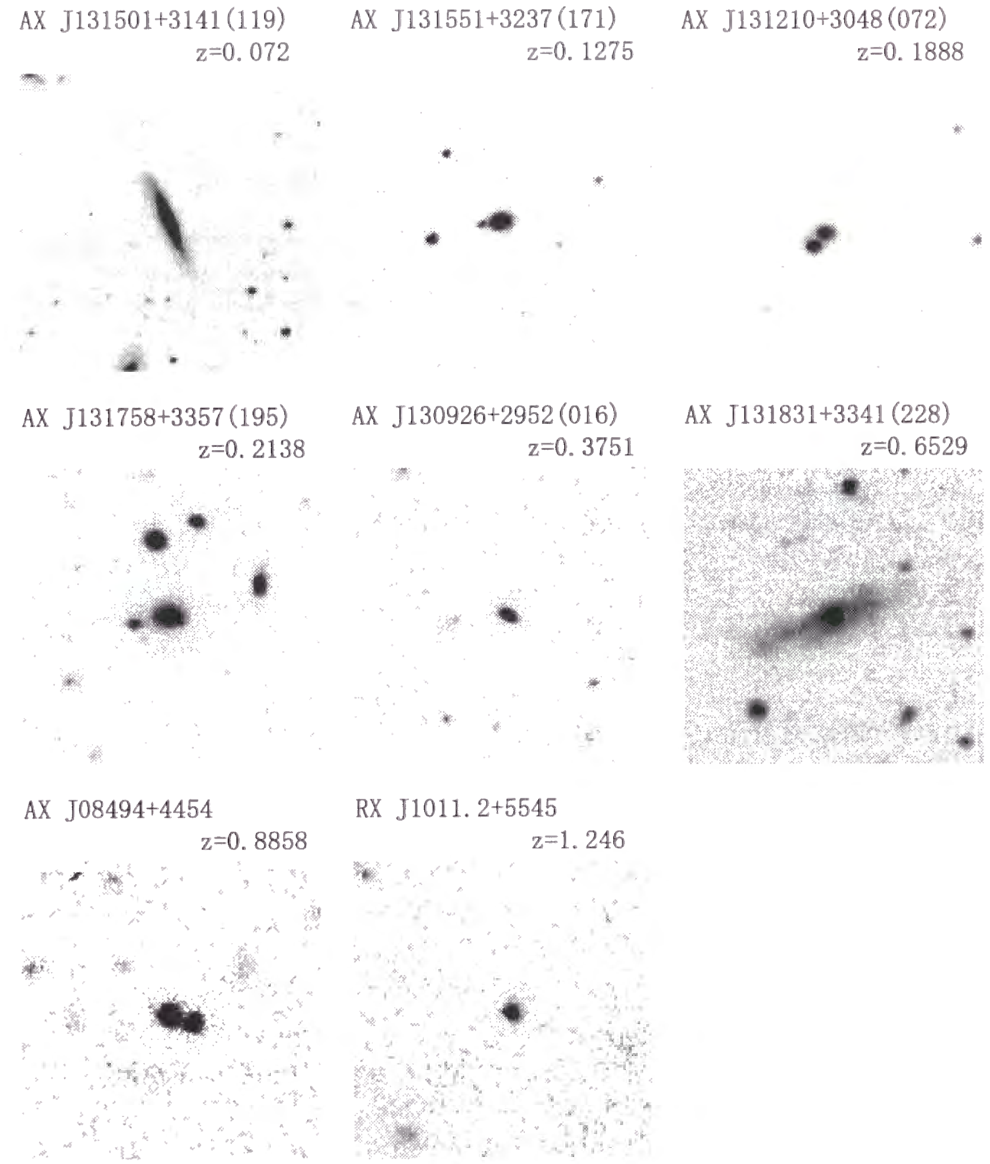

Figure 8.1: R band images of the absorbed and/or narrow-line AGNs. Field of view of each image is 200 kpc × 200 kpc at objects redshift with H_0 = 50 km s^{-1} Mpc^{-1} and q_0 = 0.5. 200 kpc corresponds to 108″ for AX J131501+3141(119), 67″ for AX J131551+3237(171), 49″ for AX J131210+3048(072), 45″ for AX J131758+3357(195), 32″ for AX J130926+2952(016), 26″ for AX J131831+3341(228), 24″ for AX J08494+4454, and 23″ for RX J1011.2+5545. North is up and east is to the left.

Name	z	B (mag)	V (mag)	R (mag)	I (mag)	$B-R$ (mag)	$V-R$ (mag)	$R-I$ (mag)
AX J131501+3141(119)	0.072	17.25	...	15.62	...	1.63	...	...
AX J131551+3237(171)	0.1275	19.74	...	18.12	...	1.62	...	...
AX J131210+3048(072)	0.1888	20.13	19.05	18.28	17.57	1.85	0.77	0.71
AX J131758+3257(195)	0.2138	19.76	18.69	17.99	17.22	1.77	0.70	0.77
AX J130926+2952(016)	0.3751	21.87	20.99	19.93	19.26	1.94	1.06	0.67
AX J131831+3341(228)	0.6529	21.23	21.06[a]	20.04[a]	18.96	1.19	1.02	1.08
AX J08494+4454	0.8858	22.07	21.42	20.78	20.19	1.29	0.64	0.59
RX J1011.2+5545	1.246	22.60	21.73	21.11	19.91	1.49	0.62	1.20

Table 8.2: Optical magnitudes and colors of the absorbed and/or narrow-line AGNs. All magnitudes are derived from the observations with the UH88″ telescope, except for magnitudes indicated with "a" which are determined based on the observations with the Subaru telescope.

8.2 Results

The resultant image of the each object in R band is shown in Figure 8.1. Except for the two highest redshift objects, all objects show extended components. Based on the data, we derived the total magnitudes and the surface brightness profiles of each object.

8.2.1 Total Magnitudes

We derived the total magnitudes of the each object within a radius of ~ 3 FWHM, masking objects around the primary object. The derived magnitudes and colors are summarized in Table 8.2.

All of them have redder $B-R$ colors than non-absorbed AGNs in our sample, whose colors distribute from -0.2 mag to 1.1 mag (see Figure 5.3). A color-color diagram of each object is shown in Section 8.2.3.

We compared the colors of the objects, with spectral evolution models of galaxies. We used two models; 1) elliptical model (plotted with a solid line in color-color diagrams) in which star formation occurs during the first 0.353 Gyr with an initial mass function with a slope of 1.20 and after that the galaxy evolves passively (Kodama & Arimoto 1997) and 2) disk model (plotted with a dotted line in color-color diagrams) in which star formation occurs constantly with the same initial mass function as the elliptical model. The colors of these models at ages from 0.01 Gyr to 12 Gyr at the objects redshifts are shown as tracks in each color-color diagram. We put tick marks on the model tracks at the age which corresponds to the age of the universe at the objects' redshifts with the cosmological parameters of $H_0 = 50$ km s^{-1} Mpc^{-1} and $q_0 = 0.5$. The colors of the 12 Gyr elliptical and the 12 Gyr disk models shifted to redshift range from 0 to 1 are consistent with

expected colors of nearby early- (NGC 224, NGC 1023, and NGC 3031) and late- (NGC 598) type galaxies at the redshift (derived based on SEDs from McQuade, Calzetti, & Kinney 1995), respectively.

In the color-color diagrams, we also plotted the expected colors of an average QSO SED (Francis et al. 1991) and power-law models with energy indices of -2.0, -1.0, 0.0, and 1.0 which cover the distribution of the QSO continuum slope (see Section 5.1).

8.2.2 Profile Measurements

To derive the surface brightness profiles of the objects, we made model surface brightnesses of the objects and measured the cross section of the model as the profiles of the objects. First, we fitted ellipses whose centers, position angles, ellipticities, and surface brightness are free parameters to the isophotes of the objects, using **ellipse** command of the **isophot** package in the IRAF. Next, based on the fitted parameters, we constructed the model images of the objects with **bmodel** command in the above package. Finally, the surface brightness profiles were derived as sections of the models along the major-axes. The method was applied to the R band images of the objects and the deep V, R, and I band images of AX J131831+3341(228). The resultant R band profiles of each object are shown in the next section. The profiles are plotted as a function of r and $r^{1/4}$ in the left and right panels, respectively. The exponential and de Vaucouleurs $r^{1/4}$ laws are straight line in the left and right panels, respectively. In each figure of the profile, we also plotted best fit model profiles of host galaxies of $z \sim 0.2$ QSOs by *Hubble Space Telescope*, except for 2 objects which are fitted well with the exponential law (McLure et al. 1999). The model profiles are converted from those of $z \sim 0.2$ to the redshift of the comparison object by correcting the $(1+z)^{-4}$ surface brightness dimming and the band shift effect. The model profiles are not convolved with the seeing size of the imaging observations.

8.2.3 Properties of Each Object

In this section, we discuss the derived colors and profiles of the each object in redshift order.

AX J131501+3141(119): $z = 0.072$, $\log L_{2-10\mathrm{keV}}(\mathrm{erg\ s^{-1}}) = 43.0$

AX J131501+3341(119) is the hardest X-ray source in the *ASCA* LSS sample of X-ray sources (Akiyama et al. 1998a, Sakano et al. 1998). Its optical spectrum is a typical narrow-line Seyfert. The R band image of the object is

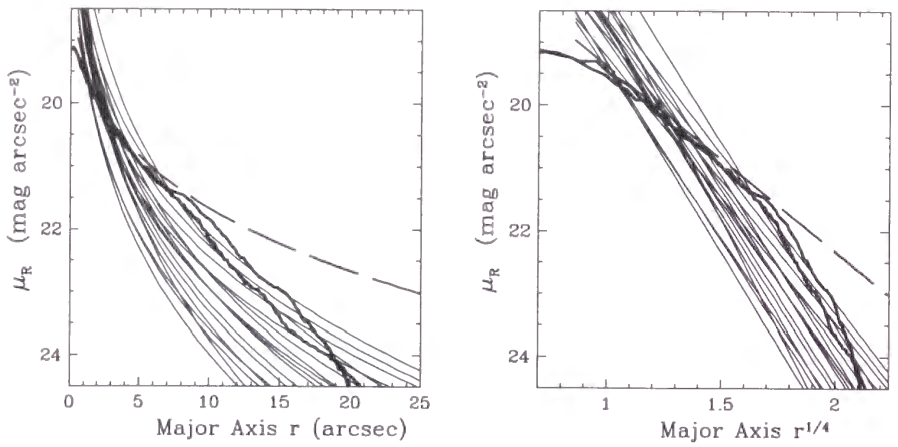

Figure 8.2: Observed R band profiles of AX J131501+3141(119). Left and right panels show the profiles as a function of r and $r^{1/4}$, respectively. Thick solid lines are the observed profiles of AX J131501+3141(119) along the major axis (position angles of 25° and 205°). Thick dashed lines are the best fit de Vaucouleurs $r^{1/4}$ law of these profiles. The fitting was done in the range from 1″ to 5.″06. Thin solid lines indicate the best fit model profiles of host galaxies of QSOs in McLure et al. (1999). We shifted the model profiles −0.667 mag for corrections of the $(1+z)^{-4}$ surface brightness dimming and the band shift effect derived from the 12 Gyr elliptical model which represents their $R-K$ colors (McLure et al. 1999).

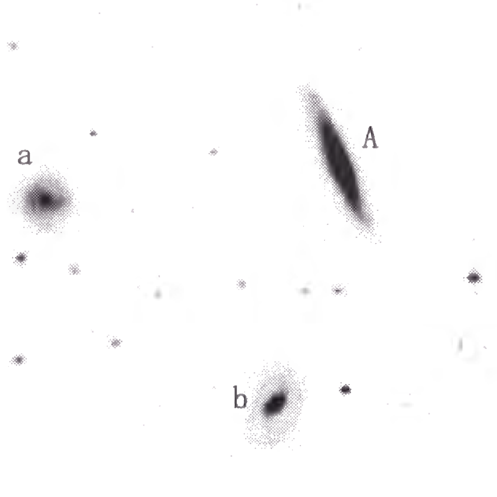

Figure 8.3: R band image of AX J131501+3141(119). Field of view of the image is $2' \times 2'$ (223kpc × 223kpc at z=0.072). Object **a** is at the same redshift of AX J131501+3141(119). Object **b** has redshift of 0.189 and it is not a member of the pair galaxies. North is up and east is to the left.

similar to that of an early-type spiral galaxy, however the R band profile of the object is peculiar as a normal early-type spiral galaxy (see Figure 8.2): though within 5″ the profile is well fitted with the de Vaucouleurs $r^{1/4}$ law, in the outer region it truncates. Galaxy interaction may cause the truncated profile. The inner bulge region is fitted with the parameters of $\mu_e = 25.06$ mag and $r_e = 139$ kpc. The galaxy has a surface brightness similar to those of the host galaxies of QSOs at $z \sim 0.2$, but has a much flat profile than them.

There are two other bright galaxies of similar size within 2′ from the object, one (galaxy **a**) located at 67″ east and the other (galaxy **b**) located at 55″ south of AX J131501+3141(119) (see Figure 8.3). In course of the multislit spectroscopy for the identification, we also observed these galaxies. The galaxy **a** has redshift of 0.072 and the velocity difference between galaxy A and **a** is 90 km s^{-1}. The projected separation corresponds to 124 kpc at the object redshift. The galaxy **b** is at redshift of 0.189, thus its closeness to galaxy A is just a chance projection.

The $B-R$ color of AX J131501+3141(119) is 1.6 mag, which is consistent with that of 12 Gyr elliptical model ($B-R = 1.75$ mag) at the redshift within the uncertainty of the photometries. The absolute magnitudes of the object are estimated to be $M_R = -22.66$ mag and $M_V = -21.96$ mag, based on the R band magnitude, k-correction and $V-R$ color of the 12 Gyr elliptical model.

AX J131551+3237(171): $z = 0.1275$, $\log L_{2-10\mathrm{keV}}(\mathrm{erg\ s^{-1}}) = 43.2$

AX J131551+3237(171) is a narrow-line Seyfert. The X-ray spectrum is consistent with an absorbed Seyfert. Morphology of the object in R band is an elliptical galaxy. The R band profiles of the galaxy are shown in Figure 8.4. They follow the de Vaucouleurs $r^{1/4}$ law well. The best fit parameters of the de Vaucouleurs $r^{1/4}$ law in the range from 1.″2 to 3.″8 are $\mu_e = 18.99$ mag and $r_e = 1.98$ kpc. The profiles are steeper than those of the QSOs at $z \sim 0.2$. The surface brightness corresponds the faintest host galaxy of the QSO sample.

The $B-R$ color of AX J131551+3237(171) is 1.62 mag, which is bluer than 11 Gyr elliptical model($B-R = 2.0$ mag) at the redshift. No radial gradient of the $B-R$ color is detected, therefore the blueness may originate from young stars distributed in the whole galaxy. The absolute magnitudes of the object are estimated to be $M_R = -21.50$ mag and $M_V = -20.85$ mag, based on the R band magnitude, k-correction and $V-R$ color of the 11 Gyr elliptical model.

The galaxy may be interacting with a small galaxy 4.″4 (13kpc at $z =$

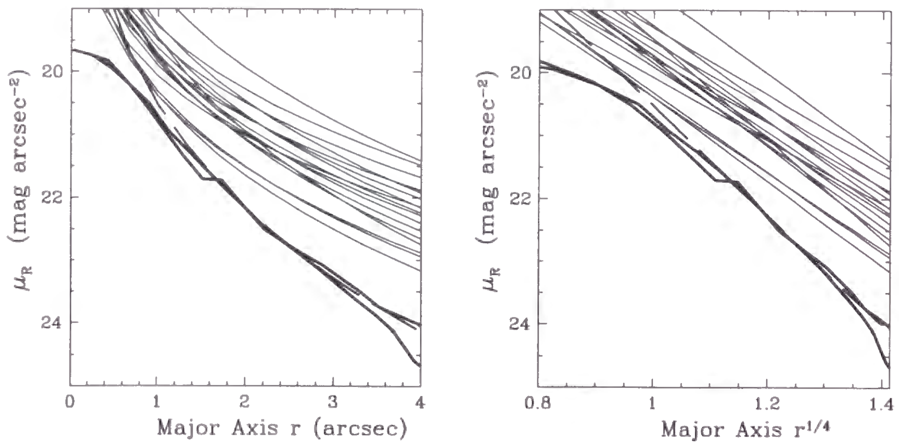

Figure 8.4: Observed R band profiles of AX J131551+3237(171). Left and right panels show the profiles as a function of r and $r^{1/4}$, respectively. Thick solid lines are the observed profiles of AX J131551+3227(171) along major axis (position angles of 100° and 280°). Thick dashed lines are the best fit de Vaucouleurs $r^{1/4}$ law of these profiles. The fitting was done in the range from 1.″2 to 3.″8. Thin solid lines indicate the best fit model profiles of QSO host galaxies in McLure et al. (1999). We shifted the model profiles −0.407 mag for corrections of the $(1+z)^{-4}$ surface brightness dimming and the band shift effect derived from 12 Gyr elliptical model which represents their $R-K$ colors (McLure et al. 1999).

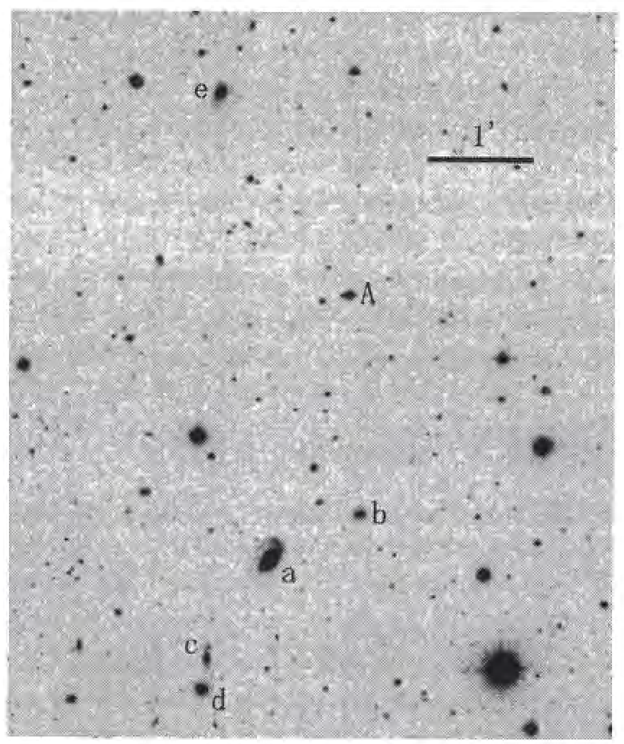

Figure 8.5: R band image of AX J131551+3227(171). Galaxy A represents AX J131551 +3227(171). Galaxy **a** and **b** have the same redshift as galaxy A. Galaxy **c**, **d**, and **e** are candidate of member galaxies of the group. North is up and east is to the left.

0.1275) east. The redshift of the small object is unknown. The small galaxy has a slightly redder color than that of AX J131551+3237(171) ($m_R = 20.70$ mag and $B-R = 1.78$ mag). In course of multislit spectroscopy of the identification, we obtained spectra of galaxies **a** and **b** in Figure 8.5. They show a strong narrow Hα emission line at $z = 0.1275$ and they possibly are member of a group of galaxies with AX J131551+3227(171). There are other candidates of members of the group of galaxies; galaxies **c**, **d**, and **e** which have a similar size to those of galaxies A, **a**, and **b** in Figure 8.5.

AX J131210+3048(072): $z = 0.1888$, $\log L_{2-10\mathrm{keV}}(\mathrm{erg\ s^{-1}}) = 43.4$

AX J131210+3048(072) is a narrow-line Seyfert. The X-ray spectrum is consistent with an absorbed Seyfert. The host galaxy is an elliptical galaxy in the R band image. The R band profiles are shown in Figure 8.6. They follow the de Vaucouleurs $r^{1/4}$ law well. The best fit parameters of the de Vaucoulerurs $r^{1/4}$ are $\mu_e = 21.61$ mag and $r_e = 8.49$ kpc. The surface brightness of the object corresponds to the faintest host galaxy of the QSO sample.

The color-color diagrams of the object are shown in Figure 8.7 (filled square). The $V-R$ and $R-I$ colors of the host galaxy are consistent with those of 10 Gyr elliptical model within uncertainties. On the contrary, the $B-V$ color is 0.4 mag bluer than the 10 Gyr elliptical model. The absolute magnitudes of the object is estimated to be $M_R = -22.33$ mag and $M_V = -21.68$ mag, based on the R band magnitude and k-correction and $V-R$ color of the 10 Gyr elliptical galaxy model.

There is a galaxy with a similar size near the host galaxy. The colors of the galaxy are consistent with the 10 Gyr elliptical model at a redshift of 0.1888. The galaxy may be interacting with the AX J131201+3048(072).

AX J131758+3257(195): $z = 0.2138$, $\log L_{2-10\mathrm{keV}}(\mathrm{erg\ s^{-1}}) = 43.7$

The optical spectrum of AX J131758+3257(195) is a narrow-line Seyfert. However, it's X-ray spectrum is not so hard (apparent photon index of 1.64 ± 0.15) and the best fit absorption column density ($0.045^{+0.192}_{-0.045} \times 10^{22}$ cm^{-2}) is well below the critical column density which divides narrow-line and broad-line AGN (10^{22} cm^{-2}, Section 4.2).

The morphology of the object in R band is a normal elliptical galaxy. The R band profile of the object is shown in Figure 8.8. It is well fitted with de Vaucouleurs $r^{1/4}$ law with $\mu_e = 21.90$ mag and $r_e = 7.60$ kpc. The surface brightness is consistent with that of the host galaxies of the QSOs.

The optical color-color diagrams of the object are shown in Figure 8.10.

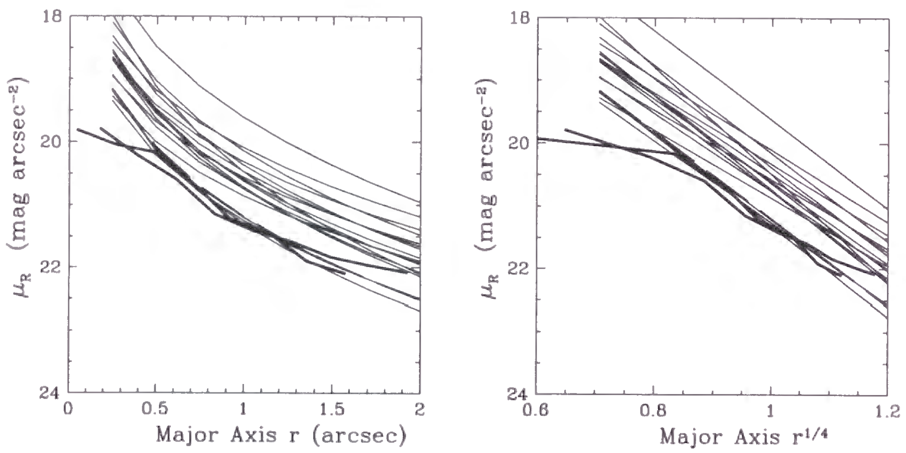

Figure 8.6: Observed R band profiles of AX J131201+3048(072). Left and right panels show the profiles as a function of r and $r^{1/4}$, respectively. Thick solid lines are the profiles of AX J131201+3048(072) along major axis (position angles of 135° and 315°). Thick dashed lines are the best fit de Vaucouleurs $r^{1/4}$ law of these profiles. The fitting was done in the range from 0.″52 to 1.″75. Thin solid lines indicate the best fit model profiles of the QSO host galaxies in McLure et al. (1999). We did not shifted the model profiles, the QSO sample have similar redshift as AX J131201+3048(072).

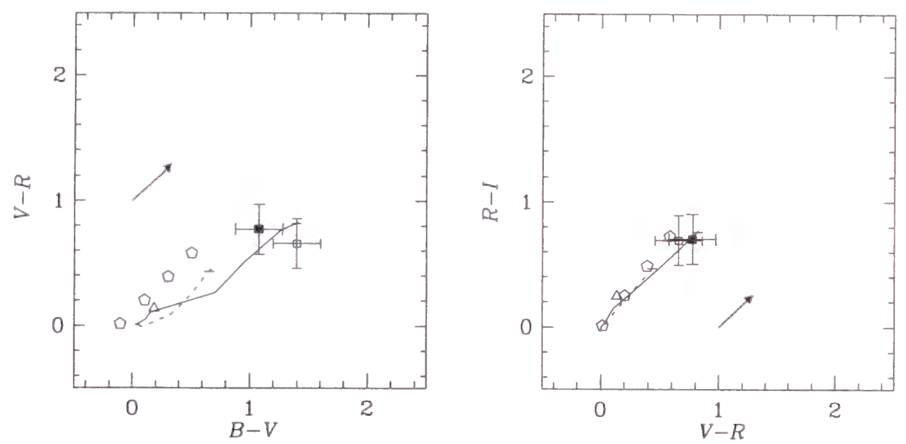

Figure 8.7: Left and right panels are $B-V$ vs. $V-R$ colors and $V-R$ vs. $R-I$ colors diagrams of AX J131201+3048(072) (filled square), respectively. Open rectangle indicate colors of the companion galaxy. The tracks of the elliptical and the disk models with ages from 0.01 Gyr to 12 Gyr are indicated with thick solid and dotted lines, respectively. The position with the model at an age of 10 Gyr are indicated with a tick mark on the each track. Open triangle represents colors of an average QSO SED (Francis et al. 1991). Pentagons show colors of power-law model with index ($f_\nu = \nu^\alpha$) of −2.0, −1.0, 0.0, and 1.0 from top to bottom. The arrow represents the effect of reddening with A_V of 1 mag.

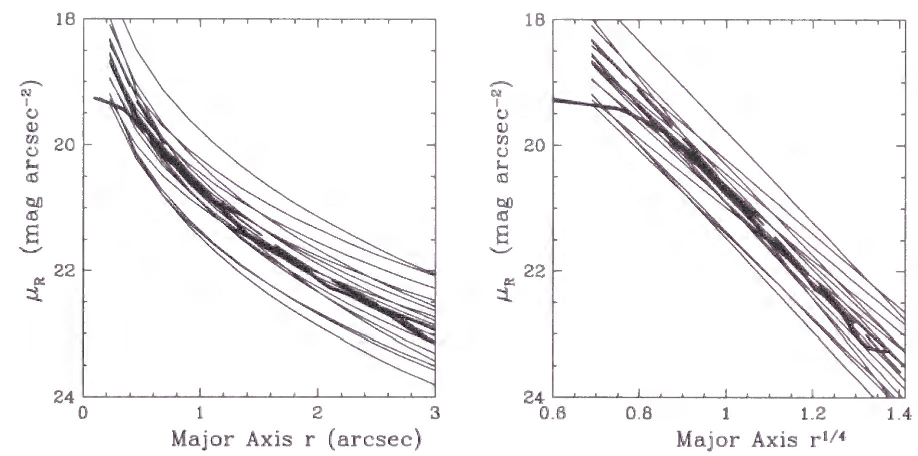

Figure 8.8: Observed R band profiles of AX J131758+3257(195). Left and right panels show the profiles as a function of r and $r^{1/4}$, respectively. Thick solid lines are the observed profiles of AX J131758+3257(195) along major axis (position angles of 100° and 280°). Thick dashed lines are the best fit de Vaucouleurs $r^{1/4}$ law of these profiles. The fitting was done in the range from 0.″66 to 2.″86. Thin solid lines indicate the best fit model profiles of host galaxies of QSOs in McLure et al. (1999). We did not shifted the profiles, because the QSO sample has the similar redshift as AX J131758+3257(195).

Name	B (mag)	V (mag)	R (mag)	I (mag)
a	22.53	20.58	20.21	19.38
b	20.94	19.93	19.23	18.44
c	21.82	20.08	19.46	18.67
d	21.74	20.41	19.76	18.85
e	22.90	21.45	20.30	19.47

Figure 8.9: Optical magnitudes of objects around AX J131758+3257(195)

$V-R$ and $R-I$ colors are consistent with that of 10 Gyr elliptical galaxy model. $B-V$ color is slightly bluer than the model. The absolute magnitude of the object is estimated to be $M_R = -22.94$ mag and $M_V = -22.29$ mag, based on the R band magnitude, k-correction and $V-R$ color of the old elliptical model.

There are several objects distribute around the AGN (see Figure 8.11). These objects may be members of a group of galaxies around AX J131758+3257(195). X-ray emission from hot gas of the group of galaxy may contribute the X-ray flux of AX J131758+3257(195) and make the X-ray spectrum softer than absorbed hard X-ray spectra of narrow-line AGNs at low-redshifts. We measured the optical magnitudes and colors of the candidates of companions. The results are summarized in Table 8.9 and plotted in Figure 8.10. Object

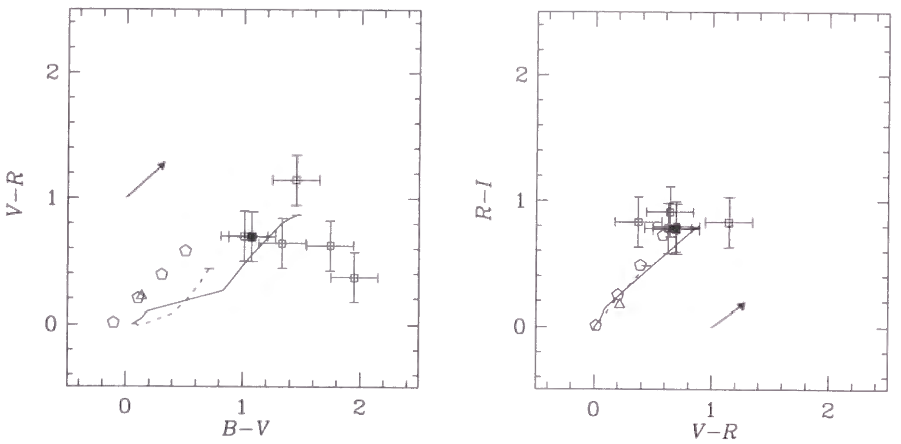

Figure 8.10: Left and right panels are $B-V$ vs. $V-R$ colors and $V-R$ vs. $R-I$ colors diagrams of AX J131758+3257(195) (solid square), respectively. The open squares indicate the colors of objects a∼e around AX J131758+3257(195). The tracks of the elliptical and disk models with ages from 0.01 Gyr to 12 Gyr are indicated with thick solid and dotted lines, respectively. The positions with the models at an age of 10 Gyr are marked with a tick mark on each track. Open triangle represents colors of an average QSO SED (Francis et al. 1991). Pentagons show colors of power-law model with index ($f_\nu = \nu^\alpha$) of −1.0, 0.0, and 1.0 from top to bottom. The arrow represents the effect of reddening with A_V of 1 mag.

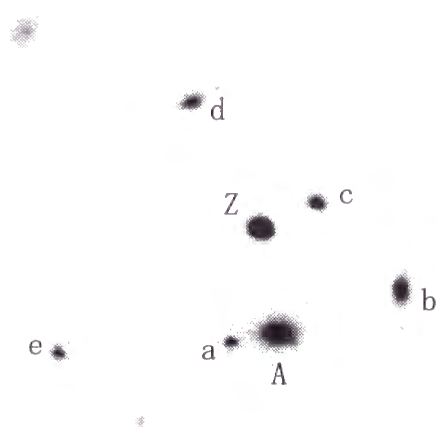

Figure 8.11: R band image of AX J131758+3257(195). Object A represents AX J131758+3257(195). Candidates of companion galaxies are marked with a∼e. The object marked with Z is a galactic late-type star.

b has the same colors with AX J131758+3257(195) within photometric uncertainties. Object **d** is consistent with the color of 10 Gyr elliptical galaxy model at redshift 0.214. They may be companion galaxies of AX J131758 +3257(195).

AX J130926+2952(016): $z = 0.3751$, $\log L_{2-10\mathrm{keV}}(\mathrm{erg\ s^{-1}}) = 43.9$

AX J130926+2952(016) is a weak-broad line AGN. The X-ray luminosity corresponds to QSOs in the hard X-ray band. The X-ray spectrum is consistent with an absorbed AGN.

The host galaxy of the object is a small elliptical galaxy. The R band profiles of the galaxy are shown in Figure 8.12. It is well described by de Vaucouleurs $r^{1/4}$ law with $\mu_e = 20.10$ mag and $r_e = 2.14$ kpc. The surface brightness is consistent with those of the host galaxies of the $z \sim 0.2$ QSOs. But, the profiles of AX J130926+2952(016) are steeper than the host galaxies of QSOs at $z \sim 0.2$.

Color-color diagrams of the object are shown in Figure 8.13. All of the $B-V$, $V-R$, and $R-I$ colors are bluer than the 8 Gyr old elliptical model at that redshift. The $V-R$ and $R-I$ colors are consistent with that of 1 Gyr elliptical model at that redshift, though the $B-V$ color is bluer than the model. The absolute magnitudes of the object are estimated to be $M_R = -22.11$ mag and $M_V = -21.70$ mag, based on the R band magnitude, k-correction and $V-R$ color of the 1 Gyr elliptical model. If we use the 8 Gyr elliptical model, the absolute magnitudes are $M_R = -22.61$ mag and $M_V = -21.96$ mag. There is no obvious companion galaxy near the object.

AX J131831+3341(228): $z = 0.653$, $\log L_{2-10\mathrm{keV}}(\mathrm{erg\ s^{-1}}) = 45.0$

AX J131831+3341(228) shows strong emission lines, such as, broad MgII 2800Å, narrow [OIII] 5007Å, and narrow [OII] 3727Å emission lines, but no broad H_β emission line. The X-ray spectrum of the object in the 0.7–10 keV band is described by an intrinsic absorption with a hydrogen column density of $N_\mathrm{H} = 6.0^{+4.4}_{-4.2} \times 10^{21}$ cm^{-2} (the object is not included in "absorbed" AGN in Chapter 6). The X-ray-to-optical flux ratio of the object, $\log f_X/f_V = 1.3$, is larger than that of the other AGNs detected in the *ASCA* LSS. The large flux ratio can be caused by absorption of optical light from the nucleus (see Section 3.3.2). These optical and X-ray characteristics suggest that the nucleus is absorbed like type 1.8∼1.9 Seyfert. Considering the hard X-ray luminosity, the object is absorbed QSO at intermediate redshift.

The deep R band image of the object shows a point-like nucleus and a peculiar extended component. The derived surface brightness profiles in

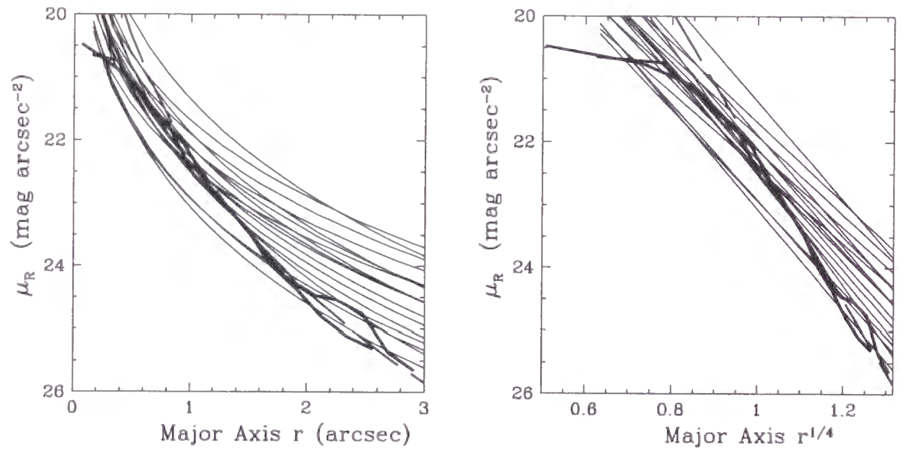

Figure 8.12: Observed R band profiles of AX J130926+2952(016). Left and right panels show the profiles as a function of r and $r^{1/4}$, respectively. Thick solid lines are the observed profiles of AX J130926+2952(016) along major axis (position angles of 65° and 245°). Thick dashed lines are the best fit de Vaucouleurs $r^{1/4}$ law of these profiles. The fitting was done in the range from 0."8 to 2."1. Thin solid lines indicate the best fit model profiles of host galaxies of QSOs in McLure et al. (1999). We shifted the model profiles 0.935 mag for corrections of the $(1+z)^{-4}$ surface brightness dimming and the band shift effect derived from 12 Gyr elliptical model which represents their $R-K$ colors (McLure et al. 1999).

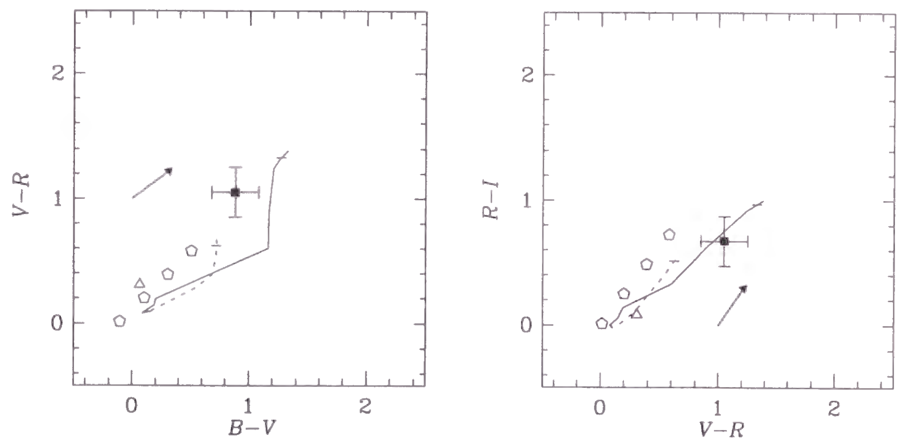

Figure 8.13: Left and right panels are $B-V$ vs. $V-R$ colors and $V-R$ vs. $R-I$ colors diagrams of AX J130926+2952(016) (filled square), respectively. The tracks of the elliptical and disk models with ages from 0.01 Gyr to 12 Gyr are indicated with thick solid and dotted lines, respectively. The positions with the models at an age of 8 Gyr are marked with a tick mark on each track. Open triangles represent colors of an average QSO SED (Francis et al. 1991). Pentagons show colors of power-law model with index ($f_\nu = \nu^\alpha$) of −2.0, −1.0, 0.0, and 1.0 from top to bottom. The arrow represents the effect of reddening with A_V of 1 mag.

Name	B (mag)	V (mag)	R (mag)	I (mag)	$B-V$ (mag)	$V-R$ (mag)	$R-I$ (mag)
Nucleus	···	22.61	22.26	21.77	···	0.35	0.49
Total-Nucleus	···	21.36	20.19	19.04	···	1.17	1.10
Within 1."88	22.25	21.74	21.06	19.98	0.51	0.68	1.08
At 2"	···	···	···	···	···	1.10	1.11

Table 8.3: Summary of Photometry of AX J131831+3341(228)

R band are shown in Figure 8.14. The extended component follows the exponential profile from 1."5 to 4". The extended component is thought to be the host galaxy of the QSO. The peculiar structure extends $\sim$ 8" away from the nuclear component (8" corresponds to 62 kpc at z=0.653). The asymmetric and extended structure of the component suggests a galaxy interaction or merging in the host galaxy.

To deconvolve the nuclear and the extended components, we fit the exponential profiles to the extended components from 1."5 to 4". By subtracting the best-fit exponential profile, magnitudes of the nuclear components are calculated to be 22.61, 22.26, and 21.77 mag in V, R, and I band, respectively. Subtractions of the magnitudes of the nuclear component from the total magnitudes give the magnitudes of the extended components; 21.36, 20.19, and 19.04 mag in V, R, and I band, respectively. To derive the $B-V$ color of the nuclear component, we measured the color within 1."88 aperture, where the optical light is dominated by nuclear component in B and V bands. Based on the differences of surface brightness of the best fit exponential law in V, R, and I bands, $V-R$ and $R-I$ colors of the extended component at 2" from the nucleus are calculated to be $V-R=1.10$ mag and $R-I=1.11$ mag, respectively. We refer the colors as those of the extended component. Derived magnitudes and colors are summarized in Table 8.3.

Color-color diagrams of the total, the nuclear, and the extended components are shown in Figure 8.15. The total colors are bluer than those of the 6 Gyr elliptical model. We discuss the origins of the extended and nuclear components separately.

The colors of the extended component fall on the track of elliptical model with an age of 1 Gyr, and the host galaxy is significantly bluer than the 6 Gyr elliptical galaxy model in the $R-I$ color. The red $V-R$ and blue $R-I$ colors of the object may reflect large Balmer decrement and small 4000Å break of the host galaxy, respectively. The 1 Gyr elliptical model spectrum corresponds to post-starburst galaxies, thus AX J131831+3341 may have a post-starburst galaxy as the host like "post-starburst quasar", UN J1025−0040

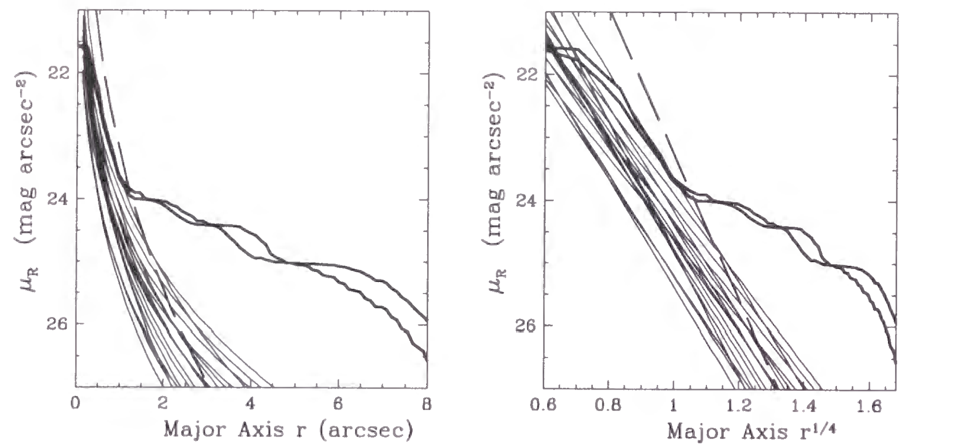

Figure 8.14: Observed R band profiles of AX J131831+3341(228). Left and right panels show the profiles as a function of r and $r^{1/4}$, respectively. Thick solid lines are the observed profiles of AX J131831+3341(228) along major axis (position angles of 114° and 294°). Thin solid lines indicate the best fit model profiles of host galaxies of QSOs in McLure et al. (1999). We shifted the model profiles 2.777 mag for corrections of the $(1+z)^{-4}$ surface brightness dimming and the band shift effect derived from 12 Gyr elliptical model which represents their $R-K$ colors (McLure et al. 1999).

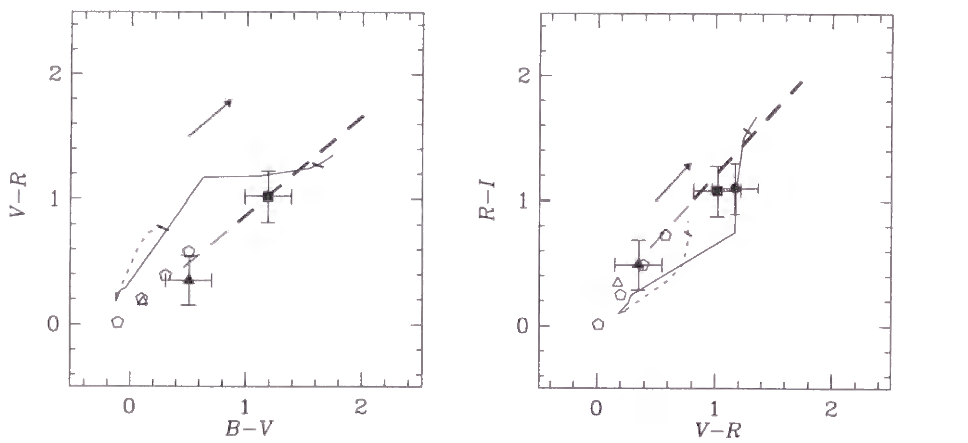

Figure 8.15: Left and right panels are $B-V$ vs. $V-R$ color and $V-R$ vs. $R-I$ color diagram of the total (filled square), the extended (filled circle: only in the right panel), and the nuclear (filled triangle) of AX J131831+3341(228). The tracks of the elliptical and constant star formation models with ages from 0.01 Gyr to 12 Gyr are indicated with solid and dotted lines in the right panel, respectively. The positions with the models at an age of 6 Gyr are marked with tick marks on each track. Open triangle represents a color of an average QSO SED (Francis et al. 1991). Hexagons show colors of power-law model with index ($f_\nu = \nu^\alpha$) of −1.0, 0.0, and 1.0 from top to bottom. The dashed line indicates the expected range of colors of the average QSO SED with the absorption derived from X-ray spectrum ($A_V = 3.35^{+2.47}_{-2.32}$ mag). The absorption ($A_V > 2.4$ mag) estimated from the optical to X-ray flux ratio of the nuclear component only permits the thick region of the line. The arrow represents the effect of reddening with A_V of 1 mag.

(Brotherton et al. 1999), which is found at redshift of 0.6344. From the R band magnitude the absolute magnitude of the extended component is estimated to be $M_B = -22.82$ mag, $M_V = -24.11$ mag, and $M_R = -23.70$ mag with the k-correction of 0.127 mag in R band, $B-R$ color of 0.88 mag, and $V-R$ color of 0.41 mag in the object rest frame, based on the 1 Gyr elliptical model.

The nuclear component should be related to the AGN. Because in the optical spectrum, strong broad Mg II 2800 Å emission line is detected and the equivalent width of the broad line (99 Å) is slightly larger than those of normal QSOs (50±29 Å ; Francis et al. 1991), implying that the nuclear component is dominated by AGN light at least in B band. Possible explanations are that we see an absorbed AGN directly or that we see a scattered AGN light. For the first case, a lower-limit to the optical extinction to the AGN derived from the optical to X-ray flux ratio ($A_V > 2.4$ mag) conflicts with the blue colors of the nuclear component (see Figure 8.15).

In narrow-line AGNs, some fraction of the nuclear light is scattered into our line of sight by dusts or electrons. In narrow-line radio galaxies, the fraction is estimated to be a few percent by spectropolarimetric observations (Alighieri, Cimatti, & Fosbury 1994). For AX J131831+3341, assuming that the nucleus has the same intrinsic optical to X-ray flux ratio of non-absorbed AGNs in the *ASCA* LSS sample (i.e., 15.0 ∼ 18.8 mag in R band) and a few percent of the nuclear light is scattered into our line of sight, the scattered component should appear with 19.2 ∼ 23.0 mag in R band. The observed R band magnitude of the nuclear component falls in the magnitude range. The $B-V$, $V-R$, and $R-I$ colors are consistent with $f_\nu \sim \nu^{-1.0}$ or $f_\nu \sim$ constant model with a A_V smaller than 1 mag (Figure 8.15). Such SED is similar to those of scattered light component in 3C radio galaxies (Alighieri et al. 1994). Also, the broad MgII 2800Å line can originate from the scattered light, like narrow-line radio galaxies (Alighieri et al. 1994; Barcons et al. 1998) and narrow-line ultra-luminous infrared galaxies (Hines & Wills 1993; Hines et al. 1995). Non-detection of broad Hβ line can be explained with a dilution by the host galaxy component in a red wavelength range. Therefore, the scattered AGN light is the most plausible origin of the nuclear component.

AX J08494+4454: $z = 0.8858$, $\log L_{2-10\mathrm{keV}}(\mathrm{erg\ s^{-1}}) = 44.0$

AX J08494+4454 is a narrow-line type 2 QSO found in the optical identification of the *ASCA* Lynx Deep Survey (Ohta et al. 1996). The optical and near-infrared spectra show only narrow emission lines, such as, Hα, [OIII] 5007Å, Hβ, [NeIII] 3967Å and 3869Å, [NeV] 3426Å, and [OII] 3727Å

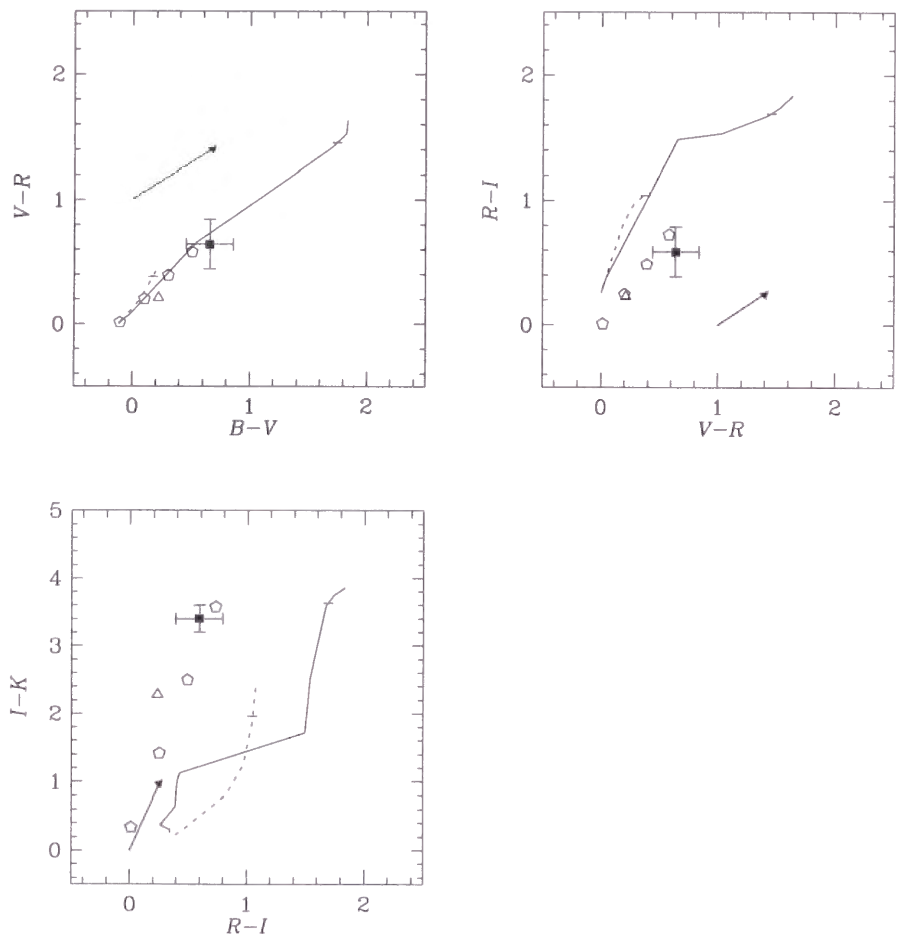

Figure 8.16: Upper left, upper right, and lower left panels are $B-V$ vs. $V-R$ colors, $V-R$ vs. $R-I$ colors, and $R-I$ vs. $I-K$ colors diagrams of AX J08484+4454. The tracks of the elliptical and disk models with ages from 0.01 Gyr to 12 Gyr are indicated with thick solid and dotted lines, respectively. The positions with the models at an age of 5 Gyr are marked with a tick mark on each track. Open triangles represent colors of an average QSO SED (Francis et al. 1991). Pentagons show colors of power-law model with index ($f_\nu = \nu^\alpha$) of −1.0, 0.0, and 1.0 from top to bottom. The arrow represents the effect of reddening with A_V of 1 mag.

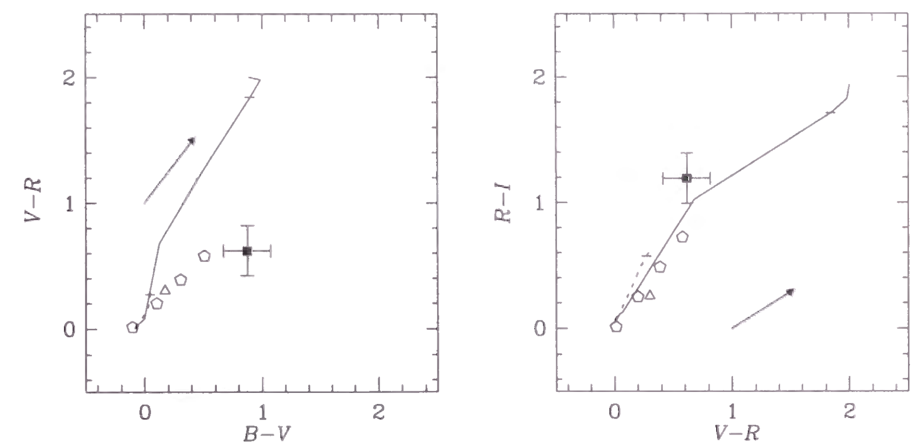

Figure 8.17: Left and right panels are $B-V$ vs. $V-R$ colors and $V-R$ vs. $R-I$ colors diagrams of RX J1011.2+5545. The tracks of the elliptical and constant star formation models with ages from 0.01 Gyr to 12 Gyr are indicated with thick solid and dotted lines, respectively. The positions with the models at an age of 4 Gyr are marked with a tick mark on each track. Open triangles represent colors of an average QSO SED (Francis et al. 1991). Pentagons show colors of power-law model with index ($f_\nu = \nu^\alpha$) of −1.0, 0.0, and 1.0 from top to bottom. The arrow represents the effect of reddening with A_V of 1 mag.

(Ohta et al. 1996, Nakanishi et al. 2000). The X-ray spectrum of the object is consistent with an absorbed AGN. The morphology of AX J08494+4454 in R band is almost stellar. I band image of the object is slightly extended in comparison with the point spread function in the image (Nakanishi et al. 2000).

We plot color-color diagrams of the object in Figure 8.16, adding the K band magnitude from Nakanishi et al. (2000). All colors are much bluer than those of 5 Gyr elliptical model at the object's redshift, except for the $I-K$ color. The colors are consistent with a power-law with index of ~ -2 ($f_\nu \propto \nu^\alpha$) or an absorbed AGN with $A_V \sim 1$ mag. The origin(s) of the optical light is not clear yet. One possible origin is a scattered nuclear light. Based on the hard X-ray flux of the object, the R band magnitude of the nucleus without absorption is expected to be $16.5 \sim 21.5$ mag, assuming the object intrinsically has the same X-ray to optical flux ratio as the LSS AGNs (see Section 3.3.2). If a few percent of the nuclear light is scattered into our line of sight, it will appear $20.5 \sim 25.5$ mag in R band. The R band magnitude of the object (20.8) falls in the range, thus, the nuclear component could be scattered light from the AGN.

RX J1011.2+5545: $z = 1.246$, $\log L_{2-10\mathrm{keV}}(\mathrm{erg\ s^{-1}}) = 45.3$

RX J1011.2+5545 is a radio-loud absorbed narrow-line QSO found in the optical identification of the *ROSAT* Medium Sensitivity Survey (Barcons et al. 1998). Its optical spectrum shows strong narrow emission lines such as CIII] 1909Å, [NeIV] 2424Å, [NeV] 3346Å and 3426Å, and [OII] 3727Å. Broad MgII 2800Å is also detected. The origin of the broad emission line is thought to be the scattered nuclear light (Barcons et al. 1998). It's X-ray spectrum is consistent with an absorbed AGN (Barcons et al. 1998).

The morphology of the object in R band is point-like. The color-color diagrams of the object is shown in Figure 8.17. All of the $B-V$, $V-R$, and $R-I$ colors are bluer than those of the 4 Gyr elliptical model. The $B-V$ and $V-R$ colors are consistent with a spectrum of a QSO with an absorption with $A_V \sim 1$ mag, but the $R-I$ color is redder than that. The scattered nuclear light is the most plausible origin of the optical light, because the broad MgII 2800Å emission line is detected. Based on the hard X-ray flux of the object, the R band magnitude of the nucleus is expected to be $15.7 \sim 20.7$ mag, assuming the object intrinsically has the same X-ray to optical flux ratio as the LSS AGNs (see Section 3.3.2). If a few percent of the nuclear light is scattered into our line of sight, it will appear $19.7 \sim 24.7$ mag in R band. The R band magnitude (21.11 mag) of the object fall in the range, thus, the nuclear component could be scattered light from the AGN.

8.3 Discussions

8.3.1 Morphologies of the Host Galaxies

In the absorbed AGN sample, 5 objects show a host galaxy component which follows the de Vaucouleurs $r^{1/4}$ law, 1 object shows a peculiar extended component, and 2 highest redshift objects only show an almost point-like component. For the 5 objects, we plotted their best-fit effective radius vs. central surface brightness in Figure 8.18. The 5 objects follow the Kormendy relation determined by nearby normal E and S0 galaxies (Hamabe & Kormendy 1987) and host galaxies of $z \sim 0.2$ QSOs (McLure et al. 1999). Considering most of bulges of spiral galaxies (small dots in Figure 8.18) distribute below the Kormendy relation, in the diagram (Capaccioli, Caon, & D'Onofrio 1992), the 5 objects reside not in bulges of spiral galaxies but in normal E and S0 galaxies. The range of the distribution ($\log r_e(\mathrm{kpc}) = 0 \sim 2$) is similar to that of normal and bright E and S0 galaxies ($\log r_e(\mathrm{kpc}) = 0 \sim 2$) but slightly wider than that of host galaxies of $z \sim 0.2$ QSOs ($\log r_e(\mathrm{kpc}) = 0.5 \sim 1.5$). Luminosities of the 5 objects distribute from $1/2\ L^*$ to $3L^*$ and peak at $2L^*$, if we adopt the absolute magnitude of the knee of the galaxy luminosity function as $M_R = -22.2$ mag in the nearby universe.

Three objects (AX J131551+3237(171), AX J131210+3048(072), and AX J131758+3357(195)) show the presence of a close companion(s), AX J 1315013141(119) has a pair galaxy, and AX J131831+3341(228) shows the peculiar morphology which suggests merging or interaction in the host galaxy. These results suggest a connection between AGN activities and galaxy interactions, but quantitative and statistical studies are required to establish the connection.

8.3.2 Colors of the Host Galaxies

For the 5 low-redshift absorbed AGNs, on the contrary to the morphology, the colors of the objects are not fully consistent with those of old elliptical galaxies. Some objects show bluer colors, especially in blue band, than old elliptical model: the $B-R$ color of AX J131551+3237(171) is 0.4 mag bluer, the $B-V$ color of AX J131210+3048(072) is 0.4 mag bluer, the $B-V$ color of AX J131758+3257(195) is 0.4 mag bluer, and the $B-V$, $V-R$, and $R-I$ colors of AX J130926+2952(016) are 0.4 mag bluer than those of elliptical models at the objects' redshift. The blue colors of these objects could originate from star formation activity in the host galaxies of these objects. The highest redshift absorbed AGN in the LSS sample (AX J131831 +3341(228)) shows two components: point-like nucleus which is thought to originate from scattered nuclear light and extended component whose colors suggest post-starburst nature of the host galaxy.

For the 2 high redshift objects (AX J08494+4454 and RX J1011.2+5545), the origin of the point like image is not clear. Considering the existence of broad MgII 2800Å emission line in RX J1011.2+5545 and optical magnitude, the scattered nuclear light is suggested to be the origin of the component.

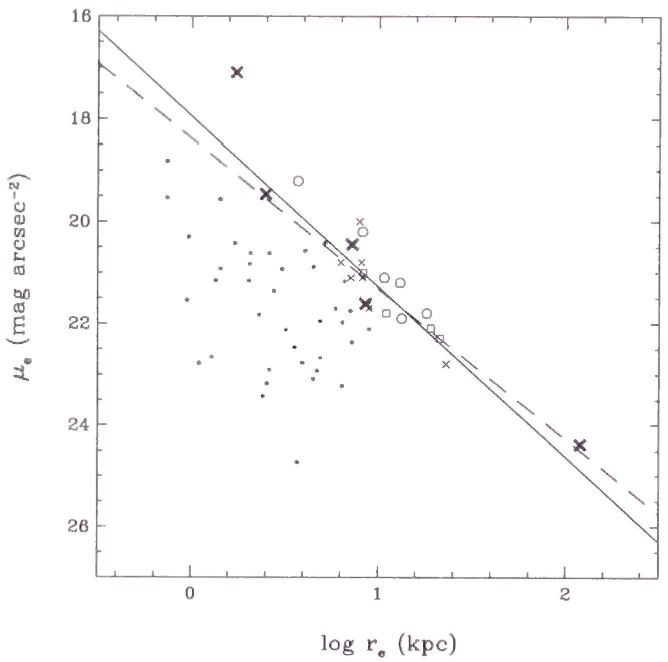

Figure 8.18: The effective radius and surface brightness relation of the 5 absorbed AGNs in the LSS sample. The surface brightness is at the effective radius in R band. We also plotted QSO host galaxies observed with *HST* from McLure et al. (1999) with small marks. Crosses, open circles, and open squares represent radio-quiet QSOs, radio-loud QSOs, and radio galaxies, respectively. We shifted ~ -1 mag for correction of $(1+z)^{-4}$ dimming and band shift effect derived from an elliptical galaxy, using a redshift of each object. Solid line represents the Kormendy relation derived from the QSO host galaxies ($\mu_{eR} = 3.34 \log r_e + 17.95$: McLure et al. 1999). Dashed line indicates the Kormendy relation determined from nearby 89 elliptical galaxies ($\mu_{eV} = 2.94 \log r_e + 19.48$: Hamabe & Kormendy 1987). We shifted the relation -0.65 mag, based on the $V-R$ color of a elliptical galaxy. Correction for Hubble constant is also applied ($\Delta \log r_e = 0.15$). Small dots indicate surface brightnesses and effective radii of bulges of spiral (Sa$\sim$Sc) galaxies in the nearby universe from Kent (1985). The r band surface brightnesses are corrected using the relation $R - r = 0.49$ for elliptical galaxies. Correction for Hubble constant is also applied.

Chapter 9

Conclusion

This chapter summarizes the results in viewpoints of the fraction of absorbed AGNs and the host galaxies of AGNs. Final section mentions prospects of hard X-ray surveys in the near future. The connection between the two questions on the fraction of absorbed AGNs and the host galaxies of AGNs will be tackled by these surveys.

9.1 What Fraction of AGNs are Absorbed ?

Based on the sample of the hard X-ray selected AGNs of the *ASCA* LSS, the dependency of the fraction of narrow-line AGNs on intrinsic luminosities and/or redshifts is detected. The X-ray sources with a hard X-ray spectrum are identified with narrow-line or weak-broad-line AGNs with hydrogen column densities of $\log N_{\rm H}({\rm cm}^{-2}) = 22 \sim 23$. The upper limit of the hydrogen column density distribution is consistent with the detection limit. Their redshift distribution is limited below redshift of 0.5 (Figure 7.1). All 11 identified AGNs at redshifts above 0.75 show strong broad MgII 2800Å and/or CIII] 1909Å emission lines. This dependency of the fraction of narrow line AGNs on the redshift also appears in redshift dependence of the strength of broad Hβ emission line. The fraction of AGNs with strong broad Hβ emission line in $0.3 < z < 0.75$ is larger than in $z < 0.3$ (Figure 4.1). It should be noted that the redshifts of AGNs in the LSS sample correlate with their X-ray luminosities, because of the selection limitation (Figure 7.1). Therefore, we could not distinguish the effect of redshift and luminosity. However, considering the luminosity - redshift distribution of absorbed and less-absorbed AGNs of the *HEAO1* A2 sample (Figure 7.1), the dependence on the luminosity is suggested.

To quantitatively examine the fraction of absorbed AGNs, we divide the LSS sample of AGNs into two groups: less-absorbed AGNs which show X-ray column density less than $\log N_{\rm H}({\rm cm}^{-2}) = 22$ and absorbed AGNs which show X-ray column density of $\log N_{\rm H}({\rm cm}^{-2}) = 22 \sim 23$. The redshift distributions of the two groups are significantly different (Figure 7.2).

In a redshift below 0.5, AGNs with the hard X-ray luminosity smaller than 10^{44} erg s^{-1} are detected in the LSS sample and there exist roughly equal number of less-absorbed and absorbed AGNs. The equal number of less-absorbed and absorbed AGNs is broadly consistent with the CXB model and the Seyfert galaxy column density distribution below $\log N_{\rm H}({\rm cm}^{-2}) = 23$ (Figure 1.2). Therefore, our results support the suggestion that narrow-line AGN is $3 \sim 4$ times more numerous than broad-line AGN in the hard X-ray luminosity below 10^{44} erg s^{-1}.

On the contrary, in the redshift range between 0.5 and 2, or in the X-ray luminosity range larger than 10^{44} erg s^{-1}, the deficiency of narrow-line absorbed AGNs is suggested. There is no absorbed AGN in the redshift and luminosity range, while 10 absorbed AGNs are expected in the LSS sample, if there are luminous absorbed AGNs as numerous as less-luminous absorbed AGNs. The deficiency suggests that the covering factor of the absorbing matter or the opening angle of the dusty torus is getting larger in the luminous AGNs.

In the LSS AGN sample, four high-redshift luminous broad-line AGNs show a hard X-ray spectrum with an apparent photon index of 1.3 ± 0.3. The hardness may be explained by the reflection component of a type 1 Seyfert. The existence of such reflection component is not established in AGNs with $10^{44 \sim 45}$ erg s^{-1} (e.g. Nandra et al. 1997).

The hard X-ray spectra may also be explained by absorption with $\log N_{\rm H}$ (cm^{-2}) $= 22 \sim 23$ at the object's redshift, if we assume an intrinsic photon index of 1.7. If the large column densities of the four hard broad-line AGNs are real, they could complement the deficiency of X-ray absorbed luminous high-redshift AGNs. However, the large column density conflicts with the presence of the strong optical broad-emission lines. (For low and intermediate redshift X-ray selected AGNs, the strength of the broad Hβ emission line correlates with the X-ray column density (Figure 4.5 and 4.6).) The four high redshift hard QSOs in the LSS sample have similar optical-to-X-ray flux ratio as other QSOs in our sample (Figure 5.2) and do not show extinction in the optical wavelength. If the large X-ray column density is real, one possible explanation is that dust in the X-ray absorbing matter is sublimated in high luminous QSOs. In that case, there can be broad-line QSOs with a large X-ray column density (Figure 9.1). Such an large X-ray column density in the luminous radio-loud broad-line QSOs is also found (Cappi et al. 1997, Reeves et al. 1997), while radio-quiet luminous QSOs do not show such a large column density (Vignali et al. 1999). To distinguish the effect of a real X-ray absorption and the intrinsically hard spectrum, such as reflection component, X-ray spectroscopic observations below 0.7 keV in the observed frame are critical.

9.2 In What Kind of Galaxy AGNs Reside ?

Optical imaging observations for 6 absorbed and/or narrow-line AGNs in the LSS sample and absorbed narrow-line QSOs found in the other surveys were done. 5 observed AGNs in the low and intermediate redshift universe reside in E or S0 galaxies. Their radial surface brightnesses are well described by de Vaucouleurs $r^{1/4}$ law, and their surface brightnesses and the effective radii follow the Kormendy relation of the E and S0 galaxies in the nearby universe (Figure 8.18). Luminosities of the galaxies distribute from 1/2 L^* to 3 L^* and peak at 2 L^*. These characteristics are consistent with host galaxies of QSOs at $z \sim 0.2$ observed by *HST* (e.g. McLure et al. 1999). However, the colors of the host galaxies in our sample are not fully consistent with that of old elliptical galaxies at that redshift. They show bluer colors than the old elliptical galaxy model (e.g. Figure 8.13). The blue colors could be originated from young (~ 1 Gyr) stellar population. To determine the origin of the blue colors and the age of the host galaxies, we require higher SN spectra, especially around 4000Å, in objects' rest frame.

The highest redshift luminous absorbed QSO in the LSS sample (AX J 131831+3341(228)) shows two components, point-like nucleus which is thought to originate from scattered nuclear light and extended component whose colors suggest post-starburst nature of the host galaxy.

Additional two high redshift absorbed AGNs show a point-like component. The possible origin of the point-like component is scattered nuclear light as well as in AX J131831+3341(228). To establish the origin of the point-like component, we need spectro-polarimetric observations of the component.

9.3 Connection between the Two Questions

Unfortunately, the size and depth of the LSS sample of AGNs are too small and shallow to quantitatively explore the column density distribution of AGNs/QSOs as a function of luminosity and redshift independently. In the near future, the situation will be changed by X-ray surveys with next

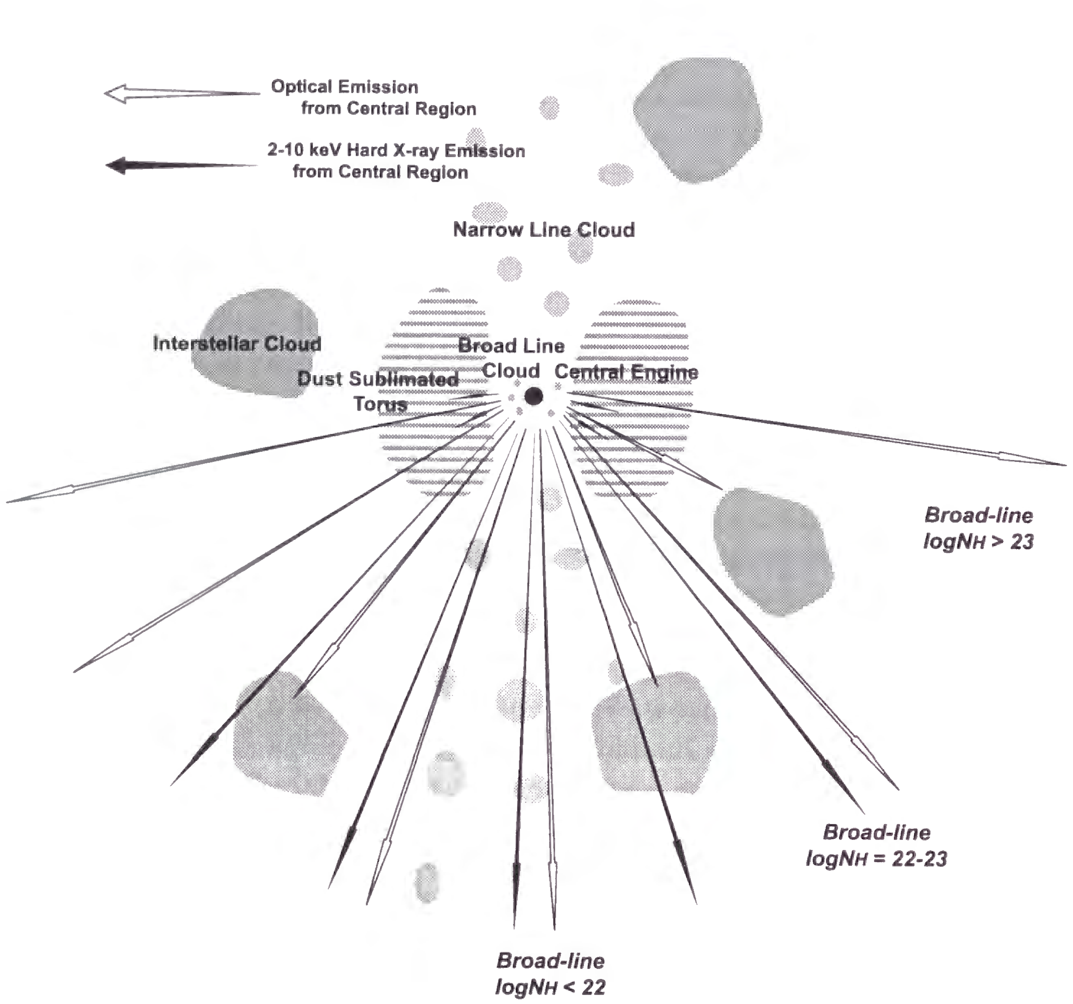

Figure 9.1: Proposed schematic view of the central region of a luminous AGN. White and black arrows represent optical and 2–10 keV hard X-ray emission from central regions.

z	$\log L_{2-10\mathrm{keV}}(\mathrm{erg\ s^{-1}}) >$			
	$\log N_{\mathrm{H}}(\mathrm{cm^{-2}}) =$			
	21.0	23.0	24.0	25.0
0.01	38.6	38.9	39.7	44.2
0.1	40.6	40.8	41.6	45.3
0.5	42.1	42.2	42.7	44.6
1.0	42.7	42.7	43.1	44.2
2.0	43.3	43.3	43.5	44.1
3.0	43.7	43.7	43.8	44.2
5.0	44.1	44.1	44.2	44.4

Table 9.1: The survey limits to the 2–10 keV intrinsic logarithmic luminosity of AGNs with various hydrogen column densities. Only an effect of photoelectric absorption is considered. The flux limit of 1×10^{-15} erg s^{-1} cm^{-2}, which roughly corresponds to that of the deep surveys with *XMM* and *Chandra*, is assumed.

generation X-ray satellites, *XMM* and *Chandra* in combination with optical (or near-infrared) identifications with a 8∼10 m class telescope. Huge and deep sample of hard X-ray selected AGNs from these surveys enables us to explore not only evolution of the X-ray luminosity function of AGNs but also evolution of the column density distribution of AGNs (Table 9.1 shows expected survey limits) up to very high redshift universe. Additionally, deep spectrophotometric observations and high-resolution near-infrared imaging observations with adaptive optics reveal the evolution of spectrophotometric and morphological properties of stellar populations in host galaxies of AGNs.

The two questions on the fraction of absorbed AGNs and the host galaxies of AGNs are discussed independently, so far. However, in viewpoint of evolution of host galaxies, they can be closely connected each other: there are much more absorbed AGNs in the high redshift universe where the host galaxies are young.

Some recent results suggest that luminous AGNs at high redshift tend to reside in a young galaxy which still has a large amount of gas: huge amounts ($10^{11} M_\odot$) of molecular gas around the AGNs are detected in submillimeter continuum and CO emission lines observations on high redshift ($z = 4 \sim 5$) QSOs and radio-galaxies (e.g. Ohta et al. 1996, Omont et al. 1996). On the contrary, submillimeter surveys for high-redshift dust- and gas- rich galaxies with SCUBA at JCMT found a 850 μm submillimeter source (SMM J02399-0136) which is identified with an optical object with strong high-ionization narrow-emission lines, such as NV 1240Å and CIV 1549Å, in the rest frame UV spectrum (Ivison et al. 1998) at a redshift of 2.8. Large infrared luminosity and the high-ionization emission lines suggest existence of luminous obscured AGN in the gas rich (molecular gas of $10^{11} M_{\odot}$ is detected, Frayer et al. (1998)) object.

In such gas-rich host galaxies, not only the fueling to the central massive black hole but also the covering factor of the central region can be much larger than AGNs in the nearby universe. In other words, the fraction of absorbed AGNs can change with the consumption of gas in host galaxies during formation and evolution of the galaxies. The problem whether there are many absorbed AGNs in young galaxies or not will be tackled by the *XMM* and *Chandra* surveys in combination with follow-up observations, such as deep submillimeter observations.

Acknowledgement

I would like to express my special thanks to Prof. Kouji Ohta. He is a supervisor indispensable for my research. I received many invaluable advises and comments from him.

I greatly thank the core members of the *ASCA* Large Sky Survey projects. Dr. Tsuru Takeshi and Dr. Toru Yamada started the project with Porf. Kouji Ohta. The X-ray data of the survey were reduced by Dr. Yoshihiro Ueda, Prof. Tadayuki Takahashi, and Dr. Masaaki Sakano. The optical identification greatly advanced with *ROSAT* and Calar Alto observations which were done in collaboration with Dr. Ingo Lehmann, Prof. Günther Hasinger, and Prof. Wolfgang Voges. The research would not be finished without any member's effort and encouragement. I am also greatly indebted to members of mosaic CCD camera and Suprime-Cam teams. Parts of the dissertation are based on the observations with these instruments. I also thank the collaborators of the optical identification of the hardest X-ray source, Dr. Michael Eracleous and Prof. Jules P. Halpern.

I appreciate hospitality of members of Department of Astronomy, Kyoto University. Especially, I would like to thank Ms. Eiko Takahashi for managing complicated paper works originated from my complicated position and Ms. Natsuko Ikemura for keeping the library very efficient. I also greatly thank hospitality of members of Subaru Telescope, National Astronomical Observatory of Japan. Particularly, I would like to thank my supervisors in the observatory, Prof. Kazuhiro Sekiguchi and Dr. Jun'ichi Noumaru.

I also thank staff members of the University of Hawaii observatory, Kitt Peak National Observatory, and Calar Alto Observatory for their hospitality during the imaging and spectroscopic observations.

I acknowledges support from a Research Fellowships of the Japan Society for the Promotion of Science for Young Scientists.

Finally, I thank my family for supporting and encouraging my research life.

Reference

Abell, G.O., Corwin, H.G., & Olowin, R.P. 1989, ApJS, 70, 1

Akiyama, M., et al. 1998a, ApJ, 500, 173

Akiyama, M., et al. 1998b, AN, 319, 63

Alighieri, S.S., Cimatti, A., & Fosbury, R.A.E. 1994, ApJ, 431, 123

Almaini, O., Boyle, B.J., Griffiths, R.E., Shanks, T., Stewart, G.C., Georgantopoulos, I. 1995, MNRAS, 277, L31

Antonucci, R. 1993, ARA&A, 31, 473

Bade, N., et al. 1998, A&AS, 127, 145

Bahcall, J.N., Kirhakos, S., Saxe, D.H., & Schneider, D.P. 1997, ApJ, 479, 642

Barcons, X., Franceschini, A., De Zotti, G., Danese, L., & Miyaji, T. 1995, ApJ, 455, 480

Barcons, X., Carballo, R., Ceballos, M.T., Warwick, R.S., & Gonzalez-Serrano, J.I. 1998, MNRAS, 301, L25

Becker, R. H., White, R. L., & Helfand, D. J. 1995, ApJ, 450, 559

Boyce, P.J., Disney, M.J., Blades, J.C., Boksenberg, A., Crane, P., Deharveng, J.M., Macchetto, F.D, Mackay, C.D., & Sparks, W.B. 1998, MNRAS, 298, 121

Boyce, P.J., Disney, M.J., & Bleaken, D.G. 1999, MNRAS, 302, L39

Boyle, B.J., Staveley-smith, L., Stewart, G.C., Georgantopoulos, I., Shanks, T., & Griffiths, R.E. 1993, MNRAS, 265, 501

Boyle, B.J., Georgantopoulos, I., Blair, A.J., Stewart, G.C., Griffiths, R.E., Shanks, T., Gunn, K.F., & Almaini, O. 1998a, MNRAS, 296, 1

Boyle, B.J., Georgantopoulos, I., Blair, A.J., Stewart, G.C., Griffiths, R.E., Shanks, T., Gunn, K.G., & Almaini, O. 1998b, MNRAS, 297, 53

Brandt, W.N., Fabian, A.C., Takahashi, K., Fujimoto, R., Yamashita, A., Inoue, H., & Ogasaka, Y. 1997, MNRAS, 290, 617

Brotherton M.S., Breugel, W.V., Stanford, S.A., Smith, R.J., Boyle, B.J., Miller, L., Shanks, T., Croom, S.M., & Filippenko, A.V. 1999, ApJ, 520, L87

Capaccioli, M., Caon, N., & D'Onofrio, M. 1992, MNRAS, 259, 323

Cappi, M., Matsuoka, M., Comastri, A., Brinkmann, W., Elvis, M., Palumbo, G.G.C., & Vignali, C. 1997, ApJ, 478, 492

Comastri, A., Setti, G., Zamorani, G., & Hasinger, G. 1995, A&A, 296, 1

Cowie, L.L., Songaila, A., Hu, E.M., Egami, E., Huang, J.S., Pickles, A.J., & Weymann, R.J. 1994, ApJ, 432, L83

de Grijp, M.H.K., Keel, W.C, Miley, G.K., Goudfrooij, P., & Lub, J. 1992, A&AS, 96, 389

De Ruiter H.R., Zamorani G., Parma P., Hasinger G., Hartner G., Trümper J., Burg R., Giacconi R., & Schmidt M., 1997, A&A, 319, 7

Egami, E., Iwamuro, F., Maihara, T., Oya, S., & Cowie, L.L. 1996, AJ, 112, 73

Elvis, M., et al. 1994, ApJS, 95, 1

Evans, D.W. 1989, A&AS, 78, 249

Falco, E.E., Kochanek, C.S., & Munoz, J.A., 1998, ApJ, 494, 47

Fiore, F., et al. 1999, MNRAS, 306, L55

Frogel, J.A., Gillett, F.C., Terndrup, D.M., & Vader, J.P. 1989, ApJ, 343, 672

Franceschini, A., Bassani, L., Cappi, M., Granato, G.L., Malaguti, G., Palazzi, E., & Persic, M. 1999, A&A, inpress, astro-ph/9912127

Francis, P.J., Hewett, P.C., Foltz, C.B., Chaffee, F.H., Weymann, R.J., & Morris, S.L. 1991, ApJ, 373, 465

Francis, P.J., Whiting, M.T., & Webster, R.L. 1999, PASA in press, astro-ph/9911195

Frayer, D.T., Ivison, R.J., Scoville, N.Z., Yun, M., Evans, A.S., Smail, I., Blain, A.W., & Kneib, J.P. 1998, ApJ, 506, L7

Gendreau, K. C., et al. 1995, PASJ, 47, L5

Georgantopoulos, I., Stewart, G.C., Blair, A.J., Shanks, T., Griffiths, R.E., Boyle, B.J., Almaini, O., & Roche, N. 1997, MNRAS, 291, 203

Georgantopoulos, I., Almaini, O., Shanks, T., Stewart, G.C., Griffiths, R.E., Boyle, B.J., & Gunn, K.F. 1999, MNRAS, 305, 125

Giacconi, R., Gursky, H., Paolini, F.R., & Rossi, B.B. 1962, Physical Review Letters, 9, 439

Gondek, D., Zdziarski, A.A., Johnson, W.N., George, I.M., McNaron-Brown, K., Magdziarz, P., Smith, D., & Gruber, D.E. 1996, MNRAS, 282, 646

Halpern, J.P., Eracleous, M., & Forster, K. 1998, ApJ, 501, 103

Halpern, J.P., Turner, T.J., & George, I.M. 1999, MNRAS, 307, L47

Hamabe, M. & Kormendy, J. 1987, In: *Structure and Dynamics of Elliptical Galaxies, IAU Symp. No.127*, p.379, ed. de Zeeuw, T., Reidel, Dordrecht.

Hasinger, G., Burg, R., Giacconi, R., Schmidt, M., Trümper, J., & Zamorani, G. 1998, A&A, 329, 482

Hasinger, G., Lehmann, I., Giacconi, R., Schmidt, M., Trümper, J., & Zamorani, G. 1999, In: *Highlights in X-ray Astronomy*, astro-ph/9901103

Hartwick, F.D.A., & Schade, D. 1990, ARA&A, 28, 437

Hill, G.J., Wynn-Williams, C.G., & Becklin, E.E. 1987 ApJ, 316, L11

Hines, D.C, & Wills, B.J. 1993, RMxAA, 27, 149

Hines D.C., Schmidt G.D., Smith, P.S., Cutri, R.M., & Low, F.J. 1995, ApJ, L1

Hooper, E.J., Impey, C.D., & Foltz C.B. 1997, ApJ, 480, L95

Huchra, J., & Burg, R. 1992, ApJ, 393, 90

Hutchings, J.B., Holtzman, J., Sparks, W.B., Morris, S.C., Hanisch, R.J., & Mo, J. 1994, ApJ, 429, L1

Hutchings, J.B., & Morris, S.C. 1995, AJ, 109, 1541

Inoue, H., Kii, T., Ogasaka, Y., Takahashi, T., Ueda, Y. 1996, In: *Rötgenstrahlung from the Universe* eds. Zimmermann, H.U., Trümper, J., and Yorke, H. MPE Report 263, 323

Ishisaki, Y., Makishima, K., Takahashi, T., Ueda, Y., Ogasaka, Y., & Inoue, H. 1999, ApJ, submitted

Iwasawa, K. 1999, MNRAS, 302, 96

Ivison, R.J., Smail, I., Le Borgne, J.F, Blain, A.W, Kneib, J.P., Bezecourt, J., Kerr, T.H., Davis, J.K. 1998, MNRAS, 298, 583

Kent, S.M. 1985, ApJS, 241, 493

Kim, D., & Elvis, M. 1999, ApJ, 516, 9

Kodama, T., & Arimoto, N. 1997, A&A, 320, 41

Kotilainen, J.K., Ward, M.J., Boisson, C., et al. 1992, MNRAS, 256, 125

Landolt, A.U. 1992, AJ, 104, 340

Lawrence, A. 1991, MNRAS, 252, 586

Madau, P., Ghisellini, G., & Fabian, A.C. 1994, MNRAS, 270, L17

Maiolino, R., & Rieke, G.H. 1995, ApJ, 454, 95

McLure, R.J., Dunlop, J.S., Kukula, M.J., Baum, S.A., O'Dea, C.P., & Hughes, D.H. 1999, MNRAS, 308, 377

McMahon, R.G., Irwin, M.J., & Hazard, C. 1992, Gemini Issue, 36, 1

McQuade, K., Calzetti, D., & Kinney, A.L. 1995, ApJS, 97, 331

Miyaji, T., Hasinter, G., & Schmidt, M. 2000, A&A, 353, 25

Moshir, M., et al. 1992, Explanatory Supplement to the IRAS Faint Source Survey, Version 2, JPL D-10015 8/92 (Pasadena: JPL)

Moreau, O., & Reboul, H. 1995, A&AS, 111, 169

Nakanishi, K., Akiyama, M., Ohta, K., & Yamada, T. 2000, ApJ, in press

Nandra, K., George, I.M., Mushotzky, R.F., Turner, T.J., & Yaqoob, T. 1997, ApJ, 488, L91

Ogasaka, Y., Inoue, H., Brandt, W.N., Fabian, A.C., Kii, T., Nakagawa, T., Fujimoto, R., & Otani, C. 1997, PASJ, 49, 179

Ohta, K., Yamada, T., Nakanishi, K., Ogasaka, Y., Kii, T., & Hayashida, K. 1996, ApJL, 458, L57

Ohta, K., Yamada, T., Nakanishi, K., Kohno, K., Akiyama, M., & Kawabe, R. 1996, Nature, 382, 426

Omont, A., Petitjean, P., Guilloteau, S., McMahon, R.G., Solomon, P.M., Pecontal, E. 1996, Nature, 382, 428

Osterbrock, D.E. 1977, ApJ, 215, 733

Osterbrock, D. E. 1989, Astrophysics of Gaseous Nebulae and Active Galactic Nuclei, University Science Books

Osterbrock, D.E, & Martel, A. 1993, ApJ, 414, 552

Phillips, M.M., Feldman, F.R, Marshall, F.E, & Wamsteker, W. 1979, A&A, 76, L14

Piccinotti, G., Mushotzky, R. F., Boldt, E. A., Holt, S. S., Marshall, F. E., Serlemitsos, P. J., & Shafer, R.A. 1982, ApJ, 253, 485

Predehl, P., & Schmitt, J.H.M.M. 1995, A&A, 293, 889

Puchnarewicz, E.M., & Mason, K.O. 1998, MNRAS, 293, 243

Reeves, J.N., Turner, M.J.L., Ohashi, T., & Kii, T. 1997, MNRAS, 292, 468

Richstone, D.O., & Schmidt, M. 1980, ApJ, 235, 361

Risaliti, G., Maiolino, R., & Salvati, M. 1999, ApJ, 522, 157

Sakano, M., et al. 1998, ApJ, 505, 129

Sakano, M., et al. 1999, Advances in Space Research, in press

Schartel, N., Schmidt, M., Fink, H.H., Hasinger, G., & Trümper, J. 1997, A&A, 320, 696

Schmidt, M., et al. 1998, A&A, 329, 495

Sekiguchi, M., Iwashita, H., Doi, M., Kashikawa, N., & Okamura, S. 1992, PASP, 104, 744

Schade, D. 1991, AJ, 102, 869

Stocke, J.T., Liebert, J., Maccacaro, T., Griffiths, R.E., & Steiner, J.E. 1982, ApJ, 252, 69

Stocke, J.T., Morris, S.L., Gioia, I.M., Maccacaro, T., Schild, R., Wolter, A., Fleming, T.A., & Henry, J.P. 1991, ApJS, 76, 813

Tadhunter, C.N., Morganti, R., di Serego-Alighieri, S., Fosbury, R.A.E, & Danziger, I.J. 1993, MNRAS, 263, 999

Takase, B., & Miyauchi-Isobe, N. 1986, Annals of the Tokyo Ast. Obs., 21, 181

Turner, T. J., & Pounds, K. A. 1989, MNRAS, 240, 833

Ueda, Y. 1996, PhD. thesis, University of Tokyo

Ueda, Y., et al. 1998, Nature, 391, 866

Ueda, Y., et al. 1999a, ApJ, 518, 656

Ueda, Y., et al. 1999b, Advances in Space Research, in press

Ueda, Y., Takahashi, T., Ishisaki, Y., Ohashi, T., & Makishima, K. 1999c, ApJ, 524, L11

Usher, P.D. 1981, ApJS, 46, 117

Vaceli, M.S., Viegas, S.M., Gruenwald, R. & de Souza, R.E. 1997, AJ, 114, 1345

Veilleux, S., Kim, D.C., & Sanders, D.B. 1999, ApJ, 522, 113

Vikhlinin, A., Mcnamara, B.R., Forman, W., Jones, C., Quintana, H., & Hornstrup, A. 1998, ApJ, 502, 558

Vignali, C., Comastri, A., Cappi, M., Palumbo, G.G.C, Matsuoka, M., & Kubo, H. 1999, ApJ, 516, 582

Vignati, P., et al. 1999, A&A, 349, L57

Visnovsky, K.L., Impey, C.D., Foltz, C.B., Hewett, P.C., Weymann, R.J., & Morris, S.L. 1992, ApJ, 391, 560

Voges, W., et al. 1999, A&A, 349, 389

Webster, R., et al. 1995, Nature, 375, 469

Whittle, M. 1992, ApJS, 79, 49

Wills, D., & Wills, B.J. 1976, ApJS, 31, 143

Winkler, H. 1992, MNRAS, 257, 677

Zimmermann, H.U., Becker, W., Belloni, T., et al. 1994, MPEreport, 257

Zwicky, F., Herzog, E., & Wild, P. 1961, Catalogue of Galaxies and of Clusters of Galaxies, (Carnegie Institution of Washington)